MINERALOGY AND CHEMISTRY OF ALTERATION

STYLES AT THE AFTON Cu-Au(-Pd) DEPOSIT,

KAMLOOPS, BRITISH COLUMBIA: CONSTRAINTS ON

FLUID TEMPERATURE, COMPOSITION, AND ORIGIN

D. Morgan Quinn © 2009

**Submitted in Partial Fulfillment of the Requirements
for the Degree of Bachelor of Sciences, Honours
Department of Earth Sciences
Dalhousie University, Halifax, Nova Scotia
April 2009**

DATE: 23/04/09

AUTHOR: Donald Morgan Quinn

TITLE: Mineralogy and Chemistry of Alteration Styles at the Afton Cu-Au(-Pd) Deposit, Kamloops, British Columbia: Constraints on Fluid Temperature, Composition, and Origin.

Degree: B. Sc   Convocation: May 21   Year: 2009

Permission is herewith granted to Dalhousie University to circulate and to have copied for non-commercial purposes, at its discretion, the above title upon the request of individuals or institutions.

_____
Signature of Author

Abstract

The Afton Cu-Au porphyry deposit near Kamloops, B.C. contains high concentrations of platinum-group elements (PGE). PGE mineralization occurs in an unusual alteration zone that developed where a high-Mg basalt subvolcanic intrusion is in contact with a syenite-monzodiorite stock. The samples examined in this study are from the hypogene zone of the Cherry Creek unit, the latest intrusive phase of the Iron Mask Batholith. They were obtained as part of DRC Resources Corporations deep drilling program that is exploring the economic potential for underground mining beyond the pit. The goal of this study is to provide a first and detailed characterization of the alteration mineralogy of the Afton deposit with a particular focus on the effects of the alkali basalt dykes on the alteration styles, and the P-T-X characteristics of the different alteration styles in the deposit in the context of Cu, Au, and PGE deposition. Petrographic characterization of vein crosscut relationships in the samples determined the timing of different alteration stages. Temperatures for the formation of chlorite and biotite were calculated based on the Al content of the tetrahedral site of chlorite and the exchange of F between biotite and apatite. Four sets of veins observed in the samples define four stages of alteration. In order of formation, from earliest to youngest, they are early carbonate, chlorite brecciation, quartz stockworks, and late carbonate. New gold geologists determined that the quartz stockworks are the most significant host to sulphide and PGE minerals. Chlorite veins are the most abundant and are associated with the formation of ore-minerals. Chlorite formed from 497-735°C ± 20°C. After the chlorite had partially crystallized, biotite precipitated out of the SiO_2–rich fluids from 723-1271°C ± 41°C. The high temperatures determined from the biotite composition suggest that the fluid was derived from the basalt intrusion. Therefore, fluid released from the late basalt intrusions would be hot enough to dissolve any minerals hosting copper, gold, and PGE and provide a mechanism to reprecipitate these elements close to the basalt and explain the presence of PGE in the quartz stockwork.

TABLE OF CONTENTS

TABLE OF TABLES

TABLE OF FIGURES

TABLE OF ABBREVIATIONS

Minerals

Ab – Albite

Ank – Ankerite

Ap – Apatite

Au – Gold

Bn – Bornite

Bt – Biotite

Cc – Chalcocite

Chl – Chlorite

Cpy – Chalcopyrite

Cb – Carbonate

Cy – Clay group minerals

Ep – Epidote

Grt – Garnet

Hem- Hematite

Ksp – Potassium Feldspar (K-feldspar)

Mg – Magnetite

Nph – Nepheline

Psmph – Pseudomorph

Py – Pyrite

Qtz – Quartz

Rb – Riebeckite

Rt - Rutile

Ser - Sericite

Spec – Specularite

Wo - Wollastonite

Rocks

Ar – Argillic alteration

Bx - Breccia

Di – Diorite

ACKNOWLEDGEMENTS

CHAPTER 1 – INTRODUCTION

The Afton ore body is a large copper-gold-palladium (Cu-Au) porphyry deposit situated within the southern Canadian Cordillera of British Columbia, near the city of Kamloops (Fig. 1.1). The host intrusion is a multistage alkalic felsic igneous body, known as the Iron Mask Batholith (IMB) (Fig. 1.2). It intruded the related Nicola Volcanic Group during the Upper Triassic period. A series of high Mg-alkali basalt intrusions cut the IMB. They are thought to be unrelated genetically to the IMB, but may have played an important role in the concentration/redistribution of some ore metals. Recent exploration beyond the pit mine has discovered highly anomalous concentrations of platinum group elements (PGE), notably palladium (Pd) mainly at the contact zone between the felsic rocks of the IMB and the mafic basalt dykes. Little is known about the alteration styles and mode of deposition of the PGE relative to Cu and Au. This report is intended to provide a first and detailed characterization of the alteration mineralogy of the Afton deposit with a particular focus on the effects of the alkali basalt dykes on the alteration styles, and the P-T-X characteristics of the different alteration styles in the deposit in the context of Cu, Au and PGE deposition.

1.1 Mining history and grade

The Afton mine was operated from 1977 to 1987 by Teck Cominco Inc. It produced 22.1 million tonnes of ore grading 0.91% copper and 0.69 g/T gold. In 1999 DRC Resources Corporation (DRC) acquired the Afton mine claims after Teck Cominco Inc. let the claims lapse. Between 2000-2003, DRC drilled 90 holes (42,450 meters) to determine the potential for underground bulk mining of high-grade Cu-Au mineralization (Behre Dolbear & Company Ltd., 2004). New Gold Corporation (New Gold) is the current owner and operator of the Afton Project claims. The latest assessment (measured and indicated) showed 65.7 million tonnes of resource grading 1.02% copper and 0.77 g/t gold (New Gold Corp., 2006).
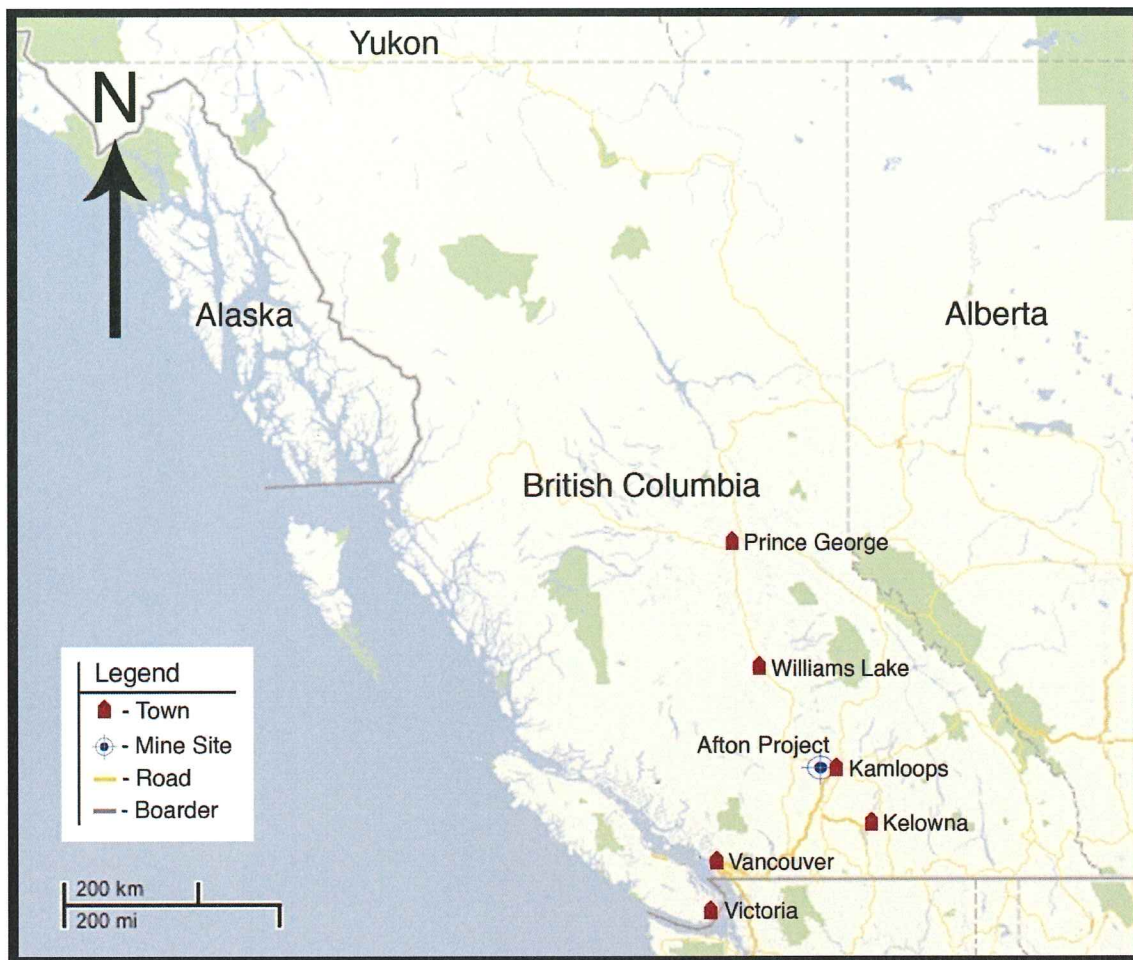
Modified from Google Maps (maps.google.ca)

Figure 1.1 Location of the Afton Deposit in British Columbia, Canada.
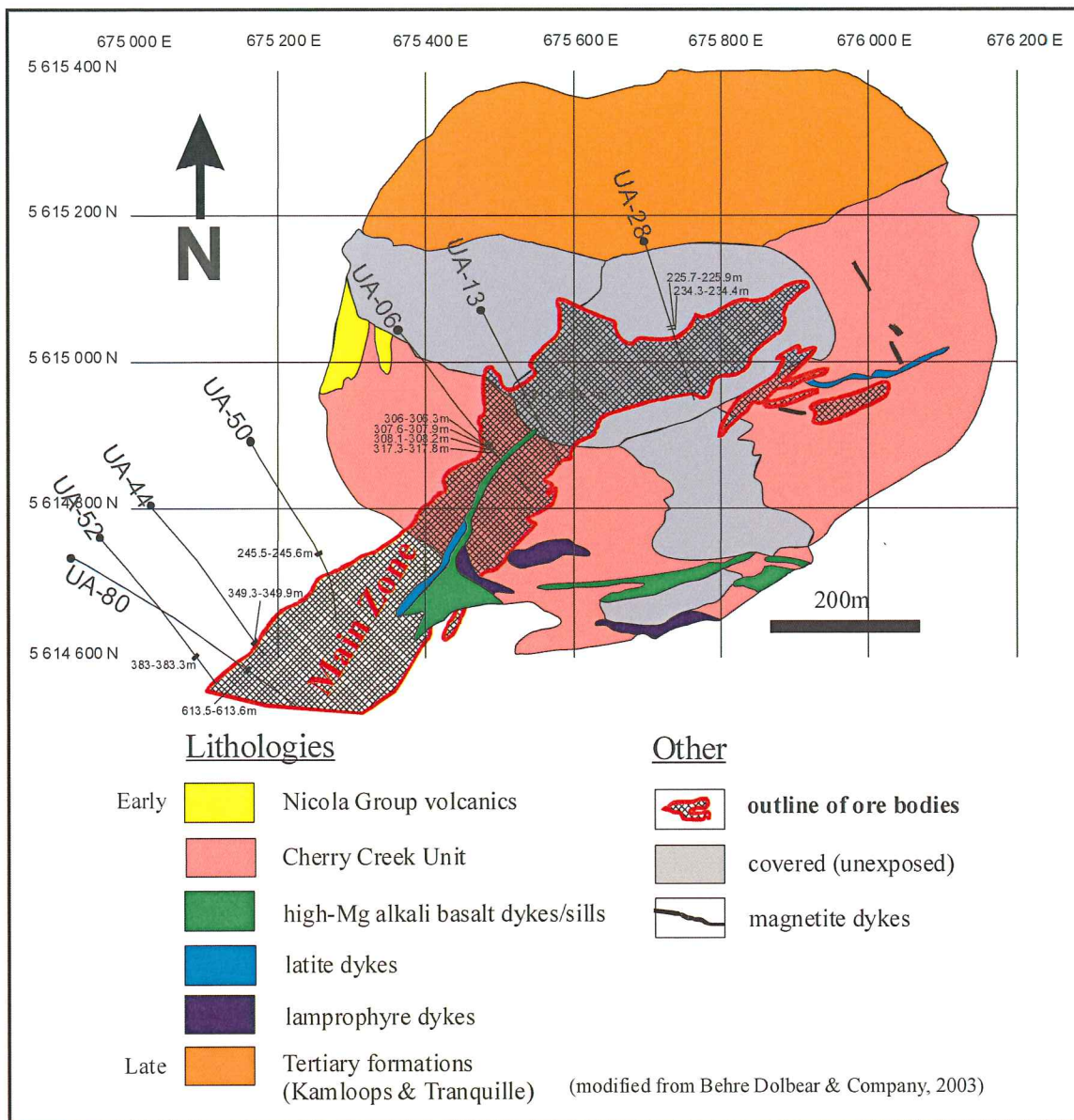
Figure 1.2 Geological Map of the Afton open pit mine showing lithologies and location of mineralized/altered samples from 7 drill holes intersecting the main mineralized zone.

1.2 Geological setting

1.2.1 Previous work

A list of research works that describe the Iron Mask Batholith and regional geology was compiled by Nixon, (2003): Cockfield (1948), Carr (1956), Carr and Reed (1976), Preto (1967, 1972), Northcote (1974, 1976, 1977), Hoiles (1978), Kwong (1982, 1987), Kwong *et al.* (1982), Snyder (1994), Lang and Stanley (1995), Ross *et. al.* (1995) and Snyder and Russell (1993, 1995). More recent summaries can be found in Nixon (2003), Owsiacki (2003), and Robinson (2007).

1.2.2 Deposit location

The Afton mine is located near Kamloops, B.C., approximately 13 km to the east of the town (Fig. 1.1; 5615087N, 675628E [NAD 83, Zone 10]). It is a part of the Quesnel Terrane within the Intermontane tectonic belt of the North American Cordillera mountain range (Fig. 1.3).

1.2.3 Geological setting and the age of the deposit

The Afton deposit is an alkalic Cu-Au porphyry that is hosted by a sub-unit of the Iron Mask Batholith (IMB) (Ross, 1993). Its formation is related to subduction magmatism in an island arc setting (Preto, 1977). The intrusion is situated within the upper Triassic Nicola volcanic rocks that came from the same magma source as the IMB (Ross, 1993; Robinson, 2007). Unconformable Tertiary volcanic and sedimentary rocks of the Kamloops Group lay horizontal on top of the Nicola Group (Nixon, 2003). Magnesium rich, alkali basalt subvolcanic intrusions cut the IMB (Robinson, 2007). These are not considered to be part of the batholith, based on the presence of this unit at distance from the IMB (Robinson, 2007) but they may be coeval with the IMB. A study by Kwong (1987) constrained the age of all units in the IMB and the basalt intrusion to between 204–194 Ma (Robinson, 2007). Recent studies agree that the basalt is the latest unit of the igneous system (Nixon, 2003; Behre Dolbear & Company, 2003). A geological map of the open pit mine can be found in Figure 1.2.

Cordilleran Terranes

mixed, TU (Taku)

ACCRETED TERRANES

Arc Terranes

inner

ST (Stikinia)

QN (Quesnellia)

intermediate position

WM (Windy-McKinley)

HA (Harrison)

CD (Cadwallader)

CK (Chilliwack)

MT (Methow)

outer

AX (Alexander)

WR (Wrangellia)

Accreted Complex Terranes

chert-rich

BR (Bridge River)

CC (Cache Creek)

SM (Slide Mountain)

clastic-rich

CG (Chugach)

PR (Pacific Rim)

YA (Yukatat)

mixed (OZ, OC, HO)

undivided metamorphic and plutonic rocks

North American craton

North American margin (ancestral North America)

MO (Monashee; craton fragment)

PERICRATONIC TERRANES

proximal

AA (Arctic Alaska)

PC (Porcupine)

CA (Cassiar)

DY (Dorsey)

distal

NS (Nisling)

YT (Yukon-Tanana)

KO (Kootenay)

metamorphic

PG (Pelly Gneiss)

500 km

Afton Project

(from Seigel, C., 2005)

Figure 1.3 Location of terrains in the Cordillera (After the Geological Survey of Canada). The Quesnel Terrane (QN) is displayed in grey.

1.2.4 Tectonic setting and similar deposits

The Canadian Cordillera is the largest mountain range of Western Canada. It formed as part of the larger American Cordillera which extends from Alaska to Chile. The main mountain building period was between 185 and 50 Ma (Geologic Survey of Canada, 2007). It is composed of a mélange of rocks from a variety of geologic settings including continental margins, volcanic arcs and deep ocean basins that were accreted onto the margin of the North American Plate as the Pacific Plate subducted beneath it. The portion of the Cordillera located in Canada is divided into five tectonic belts composed of unique rocks formed in different tectonic environments. From east to west the belts are Foreland, Omineca, Intermontane, Coast, and Insular belts (Fig. 1.3; Geologic Survey of Canada, 2007). Earthquakes, recent volcanic activity, and regional uplift over the last 10 million years in Western Canada indicate that the mountain building process is still active (Geologic Survey of Canada, 2007).

The Afton property occurs in the Quesnel Terrane which is situated in the Intermontane belt (Fig. 1.3). The Intermontane belt is a region of high plateaus, rolling uplands, and deep valley cuts. It is characterized by sedimentary and volcanic with Devonian (370 Ma) to recent ages and granitic intrusions with Early Mesozoic to Early Tertiary in age (210-50 Ma) (Melville, 1992). The geochemistry of the Intermontane rocks and the belts to the west show that their formation is unrelated to the ancient North American Plate (Survey of Canada, 2007). The Quesnel Terrane is composed of sub-aqueous and sub-aerial sedimentary and volcanic rocks that were formed in a volcanic arc setting during the Late Cretaceous to Lower Jurassic (310-180 Ma; Melville, 1992).

Several alkaline to calc-alkaline Cu-Au-Pd±Pt porphyry-related intrusions similar to the Afton deposit occur within the Quesnel Terrane and the neighboring Stikinia Terrane (Copper Mountain, Ajax/Afton, Mount Polley, Galore Creek, Cat Mountain and Kemess intrusions) (Economou-Eliopoulos, 2005). Studies focused on xenoliths, geological, mineralogical, geochemical, and isotopic data provides evidence that these intrusions were derived from an enriched mantle source region and that they were emplaced during collisional events. U-Pb dating shows that these intrusions all have an age of 210-200 Ma.

1.2.5 Nicola Group

The Nicola Group is a suite of volcanic, volcaniclastic, and sedimentary rocks that hosts the Iron Mask Batholith (Robinson, 2007). A study by Carr and Reid (1976) interpreted the Nicola Group as an "ocean fissure" volcano that developed into an island, which was then able to collect sediments along its shores (Behre Dolbear, 2004). Later stage magmatism resulted in the IMB, which came from the same magma, intruding into the core of the island (Behre Dolbear, 2004). The latest subvolcanic high-Mg, alkali basaltic intrusives (not Nicola Group; see below) have textures of proper peperites, that is, fragmentation caused by injection of high temperature magma into hydrous, partially consolidated sediments (Hanley, pers. communication). The rocks apart of the Nicola Group have undergone variable amounts of alteration.

1.2.6 Iron Mask Batholith

The Iron Mask Batholith (IMB) (Fig 1.2) is a multiple stage intrusion with a sub-alkaline to alkaline bulk composition (Nixon, 2003). It was emplaced on the southwest side of a northwest trending fault system within the upper Triassic Nicola group (Robinson, 2007). The Nicola group consists of older volcanic rocks that came from the same source as the IMB, and the fault system is thought to have controlled the shape of the intrusion, a steeply dipping, NW striking sub-planar body (Robinson, 2003; Behre Dolbear, 2004). Uranium-lead (U-Pb) zircon dating by Mortensen *et al.* (1995) determined that the batholith crystallized at 204.5 ± 3 Ma (Nixon, 2003 and references therein).

Two plutons comprise the IMB: the larger Iron Mask pluton (IM) at the south end and the smaller Cherry Creek pluton 6 kilometers NW of the Iron Mask pluton (Robinson, 2007). The IM hosts all four of the consecutive and relevant geological units represented by the IMB. Chronologically, these are identified by increasing age as the Cherry Creek, Sugarloaf, Pothook, and Iron Mask Hybrid units (Nixon, 2003). The Cherry Creek pluton is composed entirely of the Cherry Creek unit, the unit which hosts the mineralization (Robinson, 2007).

1.2.7 Cherry Creek Unit

The Cherry Creek Unit (CCU) is the latest and most widely distributed unit of the IMB (Robinson, 2007). The contact with its host, the Nicola Group, is steeply dipping to the south. A study currently in progress has determined that the CCU crystallized at a pressure between 5.1-

8.6 kbar based on Al-in-amphibole barometry (Anderson and Smith, 1995; J. Hanley, pers. communication). The CCU contains porphyritic and fine-grained varieties of diorite, monzonite and syenite, with diorite being the most abundant phase (Robinson, 2007). Albitic plagioclase (rather than Na-rich alkali feldspar) is the dominant mineral in the CCU rocks (Robinson, 2007). Microcline is the main species of alkali feldspar (Robinson, 2007). Phenocrysts of alkali feldspar are rare (Robinson, 2007). It is largely limited to the fine-grained groundmass, occurs in patchy distribution that merges into aggregates of epidote or biotite, or develops rims around plagioclase (Robinson, 2007). Late veins also host potassium feldspar, which developed chlorite along the edges (Robinson, 2007). Amphibole, along with its alteration derivatives, is the primary mafic mineral throughout most of the CCU. However, in the eastern area of the Afton pit, clinopyroxene is the dominant mineral forming up to 10 vol% of the CCU (Robinson, 2007). The possible reasons for this are lower crystallization temperatures and increased concentration and/or activity of water in the magma, which are conditions that favor the formation of hornblende.

1.2.8 High-Mg alkali basalt subvolcanic intrusions

A series of high-Mg alkali basalt dykes cut the CCU striking approximately in an E-W direction (Carr and Reid, 1976) (Fig 1.2). In past works, these rocks have been classified as "picrite" due to the high olivine content (J. Hanley, pers. Communication). However, olivine is not as abundant as clinopyroxene (which lends its pistachio green colour to misidentifying it as olivine) and the rocks are leucite-rich, making their primary alkali abundances (K_2O+Na_2O) in excess of 4 wt%. Using the new IUGS classification scheme for high-Mg volcanic rocks, this unit should be classified as high-Mg alkali basalt since picritic rocks are those with alkali abundances of less than 3% (Le Bas, 2000). They may not be genetically related to the IMB, since they outcrop far from the Batholith. On the other hand, they are spatially associated with the regional NW-trending fault system Robinson, 2007) and there is no geochronological evidence to date that precludes the IMB and dykes from having a common (parental) alkalic magma source, despite their different compositions and depths of emplacement. There is a significant interest in the dykes because they are often present within 300 m of the known mineralization in the region (Carr and Reid, 1976). It was suggested by Kwong (1987) that the interaction of CO_2-enriched fluids from the Nicola Group (Sect 1.2.5) with the Mg-rich basalt

would have raised the pH of ore-forming fluids associated with the CCU, which would potentially induce the precipitation of Cu-Fe sulphide minerals and Au (Nixon, 2003).

1.2.9 Alteration and mineralization

Porphyry deposits usually have characteristic alteration zones that can be explain in terms of two categories: hydrothermal alteration, and supergene enrichment. Hydrothermal alteration is the change in the primary mineral assemblages of the intrusions and associated wallrocks due to interaction with hot (and usually acidic) fluids that are usually exsolved during the crystallization of a volatile-saturated porphyry stock. These fluids can be released as a consequence of either primary (decompression) boiling or secondary (crystallization-induced) boiling. Most porphyry deposits develop concentric shells of different alteration styles that emanate from the core in a common pattern. The alteration zones from the core to the periphery of the porphyry system are: 1) potassic alteration, whereby primary feldspar grains are enriched in potassium, usually turning them pink, and biotite or new potassium feldspar is introduced; 2) sericitic (phyllic) alteration, whereby fine-grained inclusions of muscovite develop as it replaces primary feldspar (or secondary potassium feldspar produced by the earlier, higher temperature potassic alteration event); 3) argillic alteration, in which the breakdown of feldspars to minerals of the clay group occurs; and 4) propyllitic alteration, which occurs as the most distal zone from the core, and involves the growth of chlorite, epidote, and actinolite by breaking down Fe-Mg bearing minerals such as pyroxene and biotite, the primary magmatic minerals (Fig 1.4 and Fig 1.5).

Supergene enrichment occurs after the crystallization is complete and must be explained in terms of the overlapping supergene and hypogene zones. The supergene zone generally occurs above the water table where the mineralized porphyry rocks (hypogene) were exposed to oxidizing conditions. Here, meteoric water leaches the sulphur from Fe and Cu-bearing sulphide minerals, releasing sulphate (SO_4) and forming native copper, copper oxide (e.g., cuprite, tenorite) and iron oxyhydroxides (e.g., hematite, limonite, goethite, lepidocrocite) in the rock. These components can either replace the primary minerals in-situ or re-precipitate elsewhere as supergene alteration minerals. The hypogene zone comprises the mineralized porphyry rocks situated in more reducing conditions below the water table. The rock in this zone is unaffected by supergene enrichment and therefore represents rock only affected by hypogene alteration processes. By definition, native copper is not present in the hypogene zone.
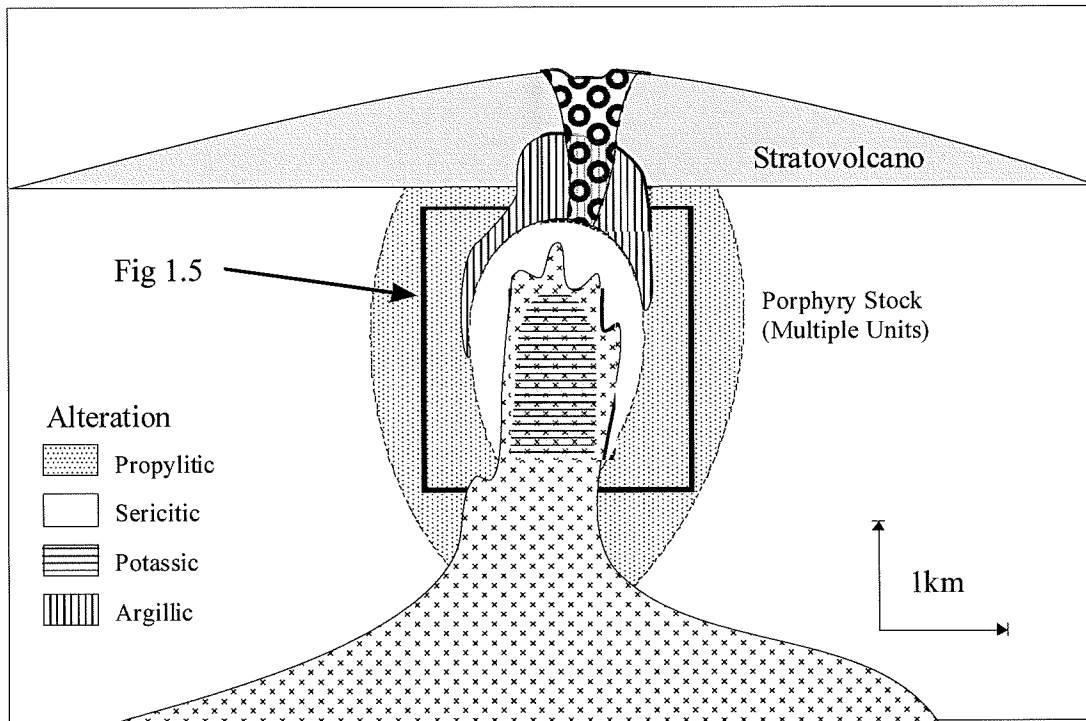
Figure 1.4 Alteration zones of a typical porphyry deposit. (After PacMag Metals Limited, 2009)
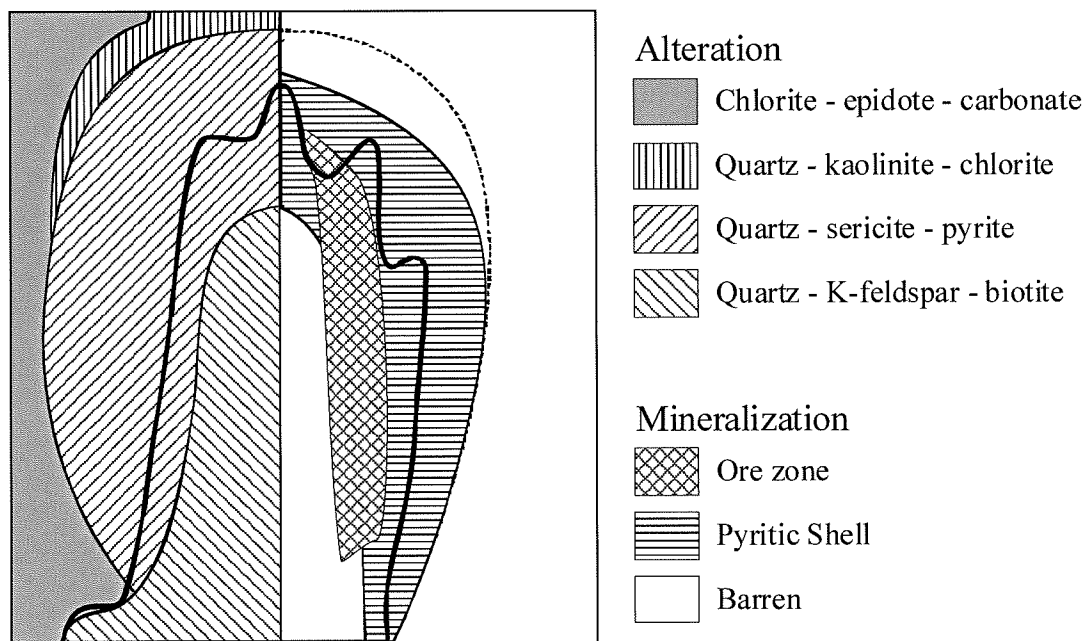
Figure 1.5 Alteration and mineralization of a typical porphyry ore-body. (After PacMag Metals Limited, 2009)

A unique feature of the Afton deposit is the absence of a well-defined (zoned or concentric) hydrothermal alteration pattern that normally accompanies porphyry systems (Robinson, 2007). A zone of abundant hydrothermal magnetite, 300 m wide and extending 800 m SE of Afton, enveloped by a pyritic zone, is the most prominent vestige of intrusion-related alteration (Robinson, 2007). The ore-body is hosted within the magnetite zone, whereas the pyritic zone is barren (Carr and Reid, 1976). This indicates that the ore minerals were deposited during the same stage as the magnetite, which precipitated from the same fluids that formed chlorite. In addition to the previously mentioned zones, poorly developed phyllic and argillic assemblages are present.

The Nicola Group alteration styles include: albitization (plagioclase grains alter to the sodic end-member); saussuritization (calcium-bearing plagioclase alters to an assemblage of zoisite, chlorite, amphibole, and carbonates); and hematitization (the pervasive introduction of hematite) (Robinson, 2007).

The common alteration styles thought to be associated with the cooling of the CCU itself include: albitization (this has occurred in all rock units of the IMB); weak to moderate sericitization of the feldspar grains; the replacement of feldspar by carbonate; and weak argillic alteration (Robinson, 2007). In addition to these common alteration styles, previous studies have noted large volumes of CCU rock that have been altered to ankerite, an iron-magnesium carbonate (Behre Dolbear & Company Ltd., 2004). Although the source of the magnesium is uncertain, a large dyke of high-Mg alkali basalt is the probable source (Behre Dolbear & Company Ltd., 2004). Because alkalic magmas generally contain low amounts of dissolved CO_2, it has been suggested by Kwong (1987) that the CO_2 responsible for the intense ankerite alteration associated with copper and gold mineralization was leached from the Nicola group (Nixon, 2003).

1.2.9.1 Hypogene zone

In the Afton open pit supergene alteration largely overprints hypogene alteration, which represents the primary hydrothermal alteration related to the cooling of the CCU. Therefore, direct observations made regarding this alteration are sparse because of the mineralogical complexity of the overlapping styles. However, work by Preto (1973) indicates that the

hypogene alteration is similar to that seen in other parts of the batholith (Carr and Reid, 1976). The first stage of the hypogene alteration was potassic alteration, marked by the growth of secondary potassium-feldspar and hydrothermal biotite. Next, propyllitic alteration introduced epidote, chlorite, and magnetite with rare occurrences of secondary quartz and calcite (Carr and Reid, 1976). Finally, phyllic alteration occurred (Carr and Reid, 1976). The distribution and intensity of the hypogene alteration effects are poorly understood (Carr and Reid, 1976). With the exception of sample UA13 214, the samples examined in this study are from the hypogene zone.

1.2.9.2 Supergene zone

Due to the highly fractured nature of the rocks at Afton and the associated high precipitation levels of a temperate paleoclimate, the supergene zone extends to abnormal depths (Carr and Reid, 1976). It has also been suggested that localized volcanic activity could have raised the ground water temperature increasing the alteration propensity (Carr and Reid, 1976). In the western end of the deposit, the zone extends much deeper, reaching depths of up to 600m (250 m elevation relative to the sea-level). But in the east, it extends only 80 m (Carr and Reid, 1976). The disintegration of the rock mass, and the pervasive introduction of hematite are the best indications of supergene alteration (Carr and Reid, 1976). What is thought to be primary magnetite is oxidizing to an earthy variety of hematite that is more prevalent in the western end of the deposit (Carr and Reid, 1976).

1.2.9.3 Mineralization

The deposit at Afton is hosted by the CCU, as are most economic prospects within the IMB (Fig. A.1.3; Carr and Reid, 1976). The supergene zone contains native copper, chalcocite, and cuprite, deposited in stockwork veinlets (Robinson, 2007). Native copper, which is characteristic of the zone, is highly depleted in trace elements and therefore is inferred to have developed through supergene alteration (Carr and Reid, 1976). Chalcocite is seen replacing bornite and chalcopyrite in thin-section, and is of the sooty variety typical of the supergene zone (Carr and Reid, 1976). In the hypogene zone, highly chloritized rocks host equal abundances of bornite and chalcopyrite in carbonate-free veins (Robinson, 2007). Where they occur together, chalcopyrite will tend to occur in the middle with bornite at the edges of the vein (Robinson, 2007). Bornite and chalcocite are also disseminated in feldspar-rich rocks of monzonitic

composition (Robinson, 2007). Within the porphyry stock, bornite and chalcopyrite mineralization is largely hosted within fractures and "crackle" breccia zones that are often highly chloritized, as disseminations, blebs, or massively. These sulphide minerals are also seen as blebs within mafic minerals replaced by chlorite (Robinson, 2007). Unlike most porphyry systems, sulphides are finely disseminated throughout the altered microdiorite (Behre Dolbear & Company, 2004) rather than occurring in discrete mineralized (porphyry-stage) veins. Minor ore styles, including a high grade, magnetite-rich carbonate ore are locally distributed around areas of intense, fracture-controlled carbonate alteration. PGE enrichments may occur in both the non-carbonate and carbonate ore styles (J. Hanley, pers. communication).

CHAPTER 2 – METHODS

2.1 Transmitted/reflected light microscopy

Polished thin sections from representative samples from 12 diamond drill hole intervals in the Afton deep drilling core library were prepared at Vancouver Petrographics, Ltd., Langley, B.C. The sections were ground to a thickness of 30 μm and polished. This allowed the samples to be viewed in transmitted light and reflected light simultaneously, so that the gangue mineralogy could be related paragenetically to the ore mineralogy without changing samples.

Petrographic analysis was conducted at Dalhousie University using a Nikon Eclipse LV 100 binocular petrographic microscope with objective lens of 2x, 10x, 20x, and 50x magnification power. This allowed accurate observations to be made on mineral grains as small as 2μm. The model of microscope used had both reflected and transmitted light capabilities. A Nikon DS-Fi1 digital camera was fitted to the microscope in order to capture plane-polarized and cross-polarized (reflected and transmitted) images of the samples as viewed through the oculars.

The identification of mineral phases was done using mainly the determinative optical properties for each mineral. In cases where a phase was unidentifiable, SEM-EDS data (an EDS spectrum) was acquired and the mineral identity confirmed from X-ray peak positions and intensities (Sect. 2.2). Grain size measurements were taken using a graticule scale that is etched into one of the oculars. Mineral abundances were obtained by a visual estimate and are semi-quantitative. They were estimated using a comparison chart for visual modal percentage estimation (Tarduno *et al.*, 2009, and references therein).

2.2 SEM-BSE/EDS/EDX analysis

To assist in identification of problematic mineral phases (i.e, those that were fine-grained, showed complex intergrowths or ambiguous optical properties), semiquantitative compositional data was acquired by scanning electron microscopy (SEM). Due to the highly altered nature of the samples, distinguishing domains of closely (compositionally) related phases (e.g. feldspars) by optical petrography proved to be very difficult. Two different SEM-EDS instruments were used throughout the study, the first at Saint Mary's University (SMU) and second at Dalhousie

University (DAL). The instrument at SMU is a LEO 1450 VP SEM equipped with backscattered electron (BSE), energy dispersive spectrometer (EDS) and energy-dispersive x-ray (EDX) capabilities. The operating conditions used for analysis of silicate minerals were 20 kV, 40-60 mA, and a working distance of ~19mm. At DAL, analysis was performed using a Hitachi S-4700 SEM with EDS capabilities. The operating conditions applied for this instrument were 10 kV, 15 mA, and a working distance of ~12mm.

2.3 Electron microprobe analysis

For the purposes of making estimates of the crystallization temperature of selected alteration minerals, quantitative analyses of chlorite and biotite-apatite pairs were obtained at Dalhousie University using a fully-automated JEOL 8200 Superprobe, five-spectrometer electron microprobe.

A standard grain of potassium kaersutite was used as a control to monitor analytical accuracy and instrument drift. Single EMP analyses of 30 grains of chlorite were performed. Two grains were rejected from the final data set because they were iron carbonate. The analytical conditions used for chlorite analysis were a 15 kV accelerating voltage and a 2 nA beam current. A summary of the recalculated chlorite analyses can be found in Table C.4

A total of 120 analyses from biotite and apatite in textural equilibrium (i.e. grains in contact with no visible reaction textures) were taken, including 12 control analyses. The analyses were done on 27 apatite biotite pairs from 5 different samples. Only one sample (UA44 349–06 B) was rejected based on unreasonably low or irregular temperature results indicating disequilibrium. Where several analyses were obtained (for the purposes of thermometric calculations; see below) for these minerals, grains were analyzed as close as possible to grain margins. For the apatite grains, a fluorapatite standard was analysed once every 10 apatite analyses as a control. Two standards, potassium kaersutite and fluorapatite, were used as controls for the biotite grains. The fluorapatite was analysed once every 10 biotite analyses and potassium kaersutite was analysed once every 20 analysis. For every grain, 2 points were selected for analyses. Therefore, for every apatite-biotite pair, 4 microprobe analyses were obtained, allowing 2 independent temperatures to be calculated for each pair. A summary of the recalculated biotite and apatite analyses can be found in Tables C.2 and C.3

2.4 Mineral chemistry and minimum crystallization temperature calculations

2.4.1 Biotite apatite halogen exchange thermometry

Constraints on the minimum temperature of at least one stage of alteration mineral crystallization (equilibration) can be calculated based on the exchange of fluorine between apatite and biotite grains that are in contact and equilibrium with one another. The method, which was developed by Zhu and Sverjensky (1992), involves the calculation of a partition coefficient, K_D, for fluorine distribution between coexisting biotite and apatite (See Appendix C.1 for sample temperature calculations). The F exchange between biotite and apatite is shown in the following reaction (Zhu and Sverjensky, 1992):

$$\tfrac{1}{2}KMg_3AlSi_3O_{10}(F)_2 + Ca_5(PO_4)_3(OH) = \tfrac{1}{2} KMg_3AlSi_3O_{10}(OH)_2 + Ca_5(PO_4)_3(F) \qquad (A)$$

fluorbiotite   hydroxyapatite   hydroxybiotite   fluorapatite
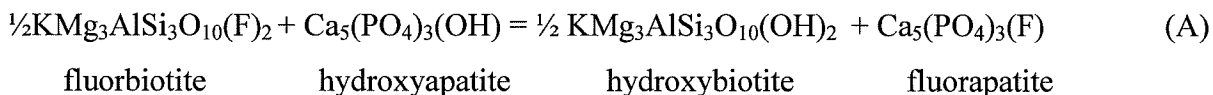
The partition coefficient (K_D) for the above reaction is defined by (Zhu and Sverjensky, 1992; Boudreau et al., 1995):

$$lnK_D = ln \frac{\left(\frac{X_F}{X_{OH}}\right) Apatite}{\left(\frac{X_F}{X_{OH}}\right) Biotite} \qquad (2.1)$$

The recalculation of oxides into cations per formula unit was performed using *MinPet*, a petrography software that was developed by MinPet Geological Software, Ltd. (Québec, Québec). The fluorine-rich nature of the apatite and biotite (Table C.2 and C.3) in this study meant the typical assumption (for structural formula recalculation purposes) that F+Cl+OH = 1 or 2 per formula unit (for apatite and biotite, respectively) was probably invalid. Instead, the number of hydroxyl groups (and corresponding F) was calculated based on 14 cations per formula unit for biotite and 10 cations per formula unit for apatite. The mole fraction of flourine (X_F) and hydroxyl (X_{OH}) were determined and used in equation 2.1 to determine K_D. To calculate minimum crystallization temperature, the following equation (Zhu and Sverjensky, 1992) was used where P represents pressure (in bars) and X_{Fe} is equal to the mole fraction of iron:

$$T = \frac{[(8852-(0.024*P)+(5000*X_{Fe})]}{[(1.987*ln\,K_D)+3.3666]} - 273.1 \qquad (2.2)$$

A P of 8.6 Kbars was used, as this is the maximum crystallization depth determined in a current study (J. Hanley, pers. communication). However, pressure has very little effect since the calculated temperature changes with respect to pressure at a rate of only 3°C/kbar.

The error margin was worked out using equation 2.4 where σ represents one standard deviation for F and Cl mole fractions or $\ln K_D$ (Zhu and Sverjensky, 1992).

$$\sigma^2_{\ln K_D} = \left(\frac{\sigma^{Bt}_{X_F}(1-X_{Cl})}{X_F(1-X_F-X_{Cl})}\right)^2_{Bt} + \left(\frac{\sigma^{Bt}_{X_{Cl}}}{X_F(1-X_F-X_{Cl})}\right)^2_{Bt}$$

$$+ \left(\frac{\sigma^{Ap}_{X_F}(1-X_{Cl})}{X_F(1-X_F-X_{Cl})}\right)^2_{Ap} + \left(\frac{\sigma^{Ap}_{X_{Cl}}}{X_F(1-X_F-X_{Cl})}\right)^2_{Ap} \qquad (2.3)$$

2.4.2 Chlorite thermometry

Calculation of the minimum crystallization temperatures using the composition of chlorite employed a modified version of the Cathelineau and Nieva (1985) temperature determination equation revised by Jowett (1991) (De Caritat *et al.* 1993, and references therein) (See Appendix C.1 for sample temperature calculations).

Because silicon and aluminum share the same crystallographic occupancy, the proportion of these elements varies in different samples. The following chemical formula is the general structural formula for chlorite. (De Caritat *et al.* 1993, and references therein):

$$\left(R^{2+}_u R^{3+}_y \square_z\right)^{VI} (Si_{4-x}Al_x)^{IV} O_{10+w}(OH)_{8-w} \qquad (C)$$
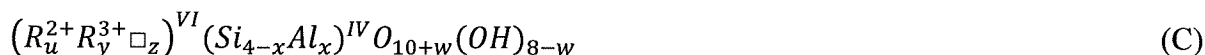
In the above formula $u+y+z=6$, $z=(y-w-x)/2$, w is usually zero or a very small number, R^{2+} usually represents Mg^{2+} or Fe^{2+}, R^{3+} usually represents Al^{3+} or Fe^{3+}, and $\square$ represents structural vacancies (De Caritat *et al.* 1993, and references therein). Cathelineau and Nieva (1985) derived the following equation by analyzing the aluminum content in chlorites with known temperatures of formation (De Caritat *et al.* 1993, and references therein):

$$T = -61.92 + 321.98\, Al^{IV} \qquad (2.4)$$

However, this does not take into account the variation in Fe/(Fe+Mg). Therefore, Jowett (1991) and others made modifications to equation 2.4 based on empirical calculations to account for variable Fe/(Fe+Mg). Using the corrections made by Jowett (1991), the following equations were used to calculate the formation temperature of chlorite in this study (De Caritat *et al*. 1993, and references therein):

$$Al_C^{IV} = Al^{IV} + 0.1(\frac{Fe}{[Fe+Mg]})$$
(2.5)

$$T = 319\, Al_C^{IV} - 69$$
(2.6)

2.5 Trace element analyses of the ores

Bulk rock analyses for selected trace elements were performed at the Ontario Geological Survey Geoscience Laboratories in Sudbury, Ontario. Representative samples of hypogene ore styles from the Afton deposit were pulverized in a chrome steel jaw crusher to a size of 90 mm, and then powdered in an agate mill to a size passing 200 mesh (70 um). The powdered samples were then dissolved by 4-acid digestion in a closed vessel and the resulting solutions analyzed by inductively-coupled plasma mass spectroscopy (ICP-MS). The multi-acid digestion was used to ensure the complete digestion of incompatible element-bearing refractory minerals (e.g., apatite, monazite, oxides).

For the purposes of data interpretation, trace element concentrations were normalized to upper crustal abundances using data for these reservoirs from the Geochemical Earth Reference Model (GERM) (EarthRef.org, 2009). Upper crustal values were used because the bulk composition of the upper crust is assumed to be most similarly felsic as the plutonic rocks at Afton, enabling a sensitive comparison of trace element abundances between rocks of differing alteration intensity and style. The samples were compared to three control samples, representing three distinct rock types of the deposit. The controls samples were fresh hornblende porphyry (112-hbphyrCC), fresh pyroxene porphyry (UA39-pxphyrCC), and high-Mg, alkali basalt (155conpic).

Mineral-melt partition coefficient values for the REE and other trace elements were also obtained from GERM. The values were used in the interpretation of the trace element results where the melt composition involved was trachyandesite, peralkaline trachyte, or low silica

rhyolite rock types since these were the most similar rock types available. This information helped to determine which minerals were most likely to host the specific trace elements of interest, thereby controlling the abundance of those elements in variable altered rock. Even though the partition coefficient obtained from GERM are for mineral-melt equilibrium, they may be used as a proxy for the assimilation of trace elements from a fluid that equilibrates with a mineral.

CHAPTER 3 – RESULTS

3.1 Ore and alteration petrography

Modal abundances are reported in Table 3.1. The samples in this study all have a microporphyritic diorite protolith. After several alteration events, they can be broadly categorized as 1) altered diorite, 2) breccia, 3) intensely seriticized, or 4) supergene rock. The dominant mineral phase of all samples is primary albite which forms most of the ground mass and phenocrysts. Carbonate, chlorite and K-feldspar are also abundant phases. Carbonate occurs in two separate sets of veins as well as semi-pervasively throughout the rock. Chlorite is the principal component in the matrix of brecciated samples. It is also seen in veins and replacing both hydrothermal and primary biotite. The abundance of chlorite, and its significant association to ore–mineralogy is absent from previous studies reviewed earlier in this paper. K-feldspar is most commonly seen next to chlorite veins, but occurs throughout the groundmass and as phenocrysts in some samples. Accessory minerals include apatite, biotite, quartz, wollastonite, epidote, hematite, reibeckite, garnet, and sericite. These are either seen in some but not all samples and are generally minor constituents. The grain size of the groundmass varies from being immeasurable to 50μm. The phenocrysts have a subhedral shape and reach up to 1.5cm but are generally around 0.75mm. Representative images taken through a microscope and with the SEM of all samples can be found in Appendix B.1 and B.2 respectively.

The degree of hydrothermal alteration is moderate to strong throughout the samples. Varying degrees of sericitization alteration are common. Pseudomorphs of aggregated carbonate and chlorite after primary biotite were seen in some samples (Fig. B.1.6 and Fig. B.1.9). Chlorite is also seen replacing hydrothermal biotite. Samples with intense carbonate alteration show albite altering to fine-grained wollastonite with garnet porphyroblasts growing near the veins. Sample UA28 – 234 shows pervasive sericitic alteration and late quartz-carbonate veining (Fig. B.1.7)

Four sets of alteration veins are seen throughout the samples. Their relative age relationships were determined on the basis of crosscutting relationships and the grain boundary relationships of secondary minerals introduced by each event. In order from the earliest to the latest they are: carbonate veins, chlorite breccia pipes, quartz stockworks, and a second set of carbonate veins.

The first set of carbonate veins are filled with massive carbonate. In some cases, the carbonate has been remobilized and precipitated with minerals related to later alteration events. These veins are also seen in the clasts of breccia samples. The next set of veins to form contains abundant chlorite and was formed during the brecciation event (with the breccia matrix containing abundant chlorite). The fluids associated with this event introduced abundant chalcopyrite, found as large blebs in the matrix and also replacing whole clasts, as well as magnetite and specular hematite. Also during this event, apatite was precipitated with specular hematite and feldspar grains of the wall rock underwent potassic alteration. It is possible that specular hematite is a result of supergene effects opposed to developing from the brecciation event. The third set of veins comprises quartz stockworks. Hydrothermal biotite precipitated close to the veins preferentially in contact with apatite or primary igneous biotite (Fig B.1.6, B.1.9, and B.1.10). The crosscutting relationship of the quartz veins and chlorite breccia pipes is not always distinct in the samples (Fig B.1), suggesting that the chlorite had not fully crystallized when the quartz veins began to form. Some of these veins also contain variable amounts of carbonate, chlorite, apatite, bornite, chalcopyrite, and gold. The sulphide minerals seen in these veins may indicate that themetals that were remobilized by the quartz-precipitating fluids and re-precipitated, or that a second minor mineralizing event occurred. The last set of veins to form are filled with crystalline carbonate. No other minerals were introduced during this event. Overall, the chlorite veins are most abundant and are significant because they are host to the majority of ore minerals. However, in the context of PGE the quartz stockworks are more important as they are the main host to precious metals at Afton. A plot illustrating the timing of formation for each mineral observed can be found in Figure 3.1.

3.2 Minimum temperatures of crystallization of alteration minerals

The results of temperature calculations are based on element partitioning between co-existing minerals mentioned in section 2.2. The results give estimates for the minimum (closure) crystallization temperatures of those minerals in a specific sample. When a crystal cools below its closure temperature it can no longer exchange ions with fluids or other grains, therefore the composition is set. The closure temperature can change as the composition of the minerals changes. By measuring the contents of the elements exchanging between two minerals, it is possible to obtain accurate temperatures during their equilibration. This study uses

geothermometers based on the Mg/(Fe+Mg) and tetrahedral Al content of chlorite and the exchange of F between biotite and apatite. It was concluded that hydrothermal fluids deposited all of these minerals; therefore the results are representative of the approximate minimum temperature of the fluid responsible for each event.
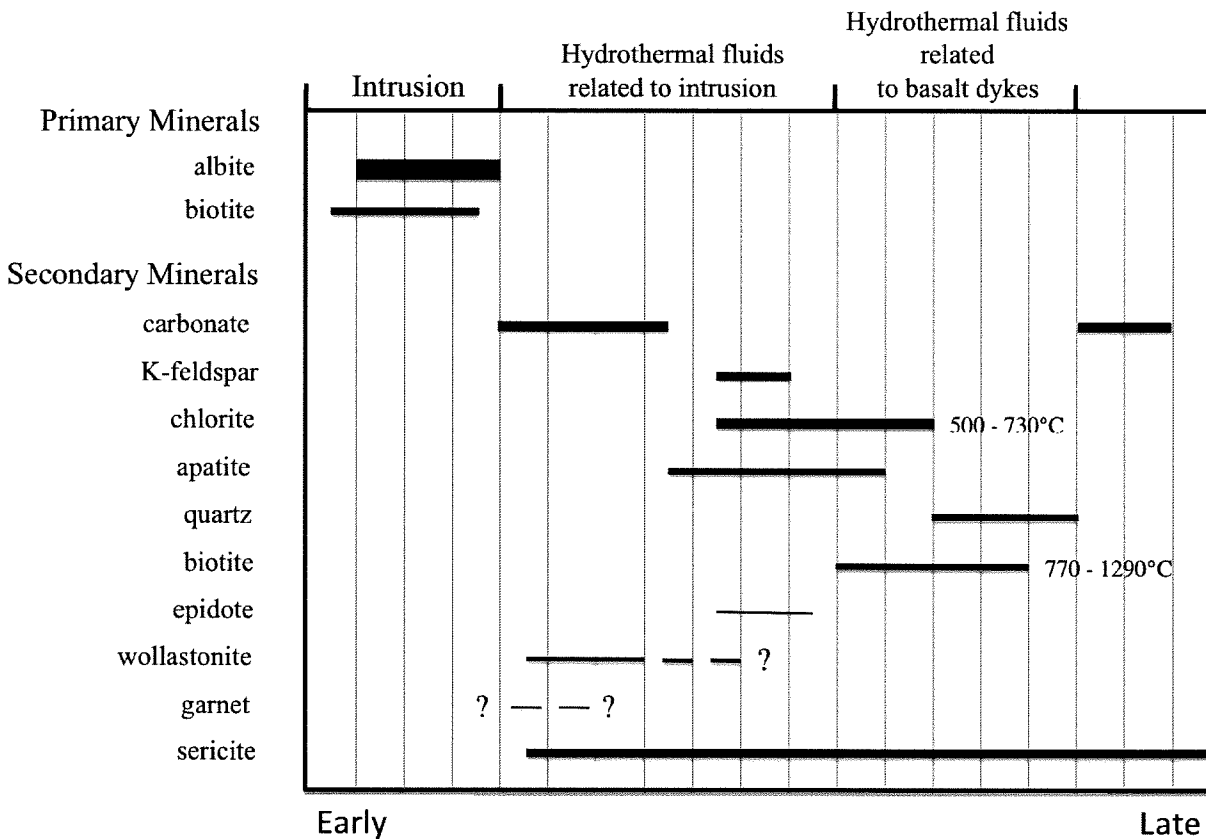
Figure 3.1 Paragentic mineralogical sequence observed in the altered/mineralized samples. Relative abundance is represented by line thickness and relative timing is represented by position and line length.

Table 3.1 Modal abundance

Sample: UA06‑306	%	UA06‑307	%	UA06‑308	%	UA06‑317	%	UA13‑214	%	UA28‑225	%
Phenocrysts		**Phenocrysts**	**35**	**Phenocrysts**	**30**	**Phenocrysts**	**22**	**Phenocrysts**	**40**	**Phenocrysts**	**33**
		Ab	25	Ab	28	Ksp	15	Ab	10	Ab	13
		Ksp	9	Ap	2	Ab	5	Ksp	8	Cb psmph	10
		Rb	1			Bt	1	Ap	8	Bt	7
						Ap	1	Bt	5	Ap	3
								Ser	2		
								Cb	7		
Groundmass	**45**	**Groundmass**	**38**	**Groundmass**	**41**	**Groundmass**	**63**	**Groundmass**	**57**	**Groundmass**	**60**
Chl	20	Ab > Ksp		Ab > Ksp		Ab > Ksp		Ab < Ksp	49	Ab	50
Ab+Ksp	3	Chl						Hem	8	CO_3	10
Qtz	15										
Cb	7										
Veins	**5**	**Veins**	**20**	**Veins**	**24**	**Veins**	**10**	**Veins**	**2**	**Veins**	**4**
Cb	3	Cb	10	Chl	17	Chl	2	Cb	2	Qtz	2
Qtz	2	Chl	7	Cb	3	Cb	8			Cb	2
		Qtz	3	Nph	2						
				Ap	1						
				Qtz	1						
Opaques	**50**	**Opaques**	**7**	**Opaques**	**5**	**Opaques**	**5**	**Opaques**	**1**	**Opaques**	**3**
Mg		Cpy		Cpy		Cpy		Cu		Cpy	
Cpy				Bn		Cc		Spec		Py	
Py						Au		Bn			

Table 3.1 Modal abundance continued

Sample	UA28 - 234	%	UA44 - 349	%	UA50 - 245	%	UA52 - 383	%	UA80 - 613	%	UA100 - 822	%
	Phenocrysts	**25**	**Phenocrysts**	**35**	**Phenocrysts**	**40**	**Phenocrysts**	**40**	**Phenocrysts**	**39**	**Phenocrysts**	**40**
	Cy/Ank/Wo psmph		Ab	13	Ab	15	Ab	33	Ab	20	Ab	38
	Ap	2	Ksp	5	Wo	5	Cb psmph	5	Ap	2	Ap	2
			Cb psmph	5	Ap	5	Ap	2	Chl	3		
			Bt	7	Ksp	1			Grt	1		
			Chl	5	Chl	5			Qtz	3		
					Bt	1			Wo	10		
					Cb psmph	10						
	Groundmass	**60**	**Groundmass**	**56**	**Groundmass**	**55**	**Groundmass**	**47**	**Groundmass**	**55**	**Groundmass**	**38**
	Ab		Ab	41	Ab>Ksp		Ab	25	Ab<CO$_3$		Ab	8
	Ksp		Ksp	15	Ser		Ksp	15	Ser	7	Chl	7
							Qtz	1			Cb	20
							Hem	1			Ser	3
							Chl	5				
	Veins	**10**	**Veins**	**4**	**Veins**	**2**	**Veins**	**10**	**Veins**	**3**	**Veins**	**17**
	Qtz	10	Cb	3	Qtz	2	Cb	4	Cb	1	Ap	<10
			Qtz	1			Chl	3	Chl	0.5	Cb	>10
							Ep	2	Qtz	0.5		
							Qtz	1	Bt	1		
	Opaques	**5**	**Opaques**	**5**	**Opaques**	**3**	**Opaques**	**3**	**Opaques**	**3**	**Opaques**	**5**
	Cpy		Cpy		Cpy		Py		Cpy		Spec	
	Bn		Py		Py		Cpy		Bn		Cpy	
			Bn				Spec		Au		Py	

Biotite and apatite are both fluorine-rich relative to chlorine. The temperatures calculated from the biotite-apatite compositional data range from 723-1271°C ± 41°C (Fig 3.2 and Table C.1.1). The error was calculated using the standard deviation of cation values of the control samples in equation 2.3. If lower values for pressure are used, the temperatures increase, therefore this is a minimum temperature at which biotite crystallized. Biotite grains that formed at higher temperatures are Mg-rich relative to those that formed at lower temperatures. The temperatures calculated based on the chlorite data range from 497-735°C ± 20°C. The error was calculated assuming a maximum of 3% error associated with the electron microprobe as estimated by the intstruments technician (D.J. MacDonald pers. communication) (Fig. 3.3 and Table C.1.3; temperatures are rounded to the nearest degree).

3.3 Trace element distribution in ores

In general the rocks at Afton are depleted in incompatible trace elements, notably the REE, with respect to the upper crust. This could reflect their formation from the melts derived from the depleted mantle source or later leaching out of incompatible elements due to the interaction with the fluids. The rocks have abundant apatite and other minerals that typically concentrate these elements (e.g., garnet, oxides). On the other hand, apatite and other incompatible element-rich minerals in these samples could have behaved as fluid refractory minerals. In other words, these minerals may have crystallized early, becoming enriched in trace elements but the remainder of the bulk rock incompatible elements have since been flushed out due to interaction of those rocks with hot hydrothermal fluids in which apatite and other refractory phases were insoluble. A notable exception to the general depleted nature of the samples (relative to upper crust) is elevated levels of Ni, Co, and less often Cr in most of the samples. These elements are most likely contained within sulphide minerals and magnetite; thus, elevated levels are expected in the Afton rocks since these minerals are abundant. Another exception is a consistent enrichment of V relative to the upper crust. Vanadium prefers to go into magnetite and biotite (J. Hanley, pers. communication), both of which are abundant minerals in the Afton rocks. The samples can be divided into four groups when compared to the three control samples based on which rock type exhibited a similar peak pattern. Group A are those samples that are most similar to the fresh pyroxene porphyritic, group B are also most similar to the fresh pyroxene porphyritic rock, but

are different from group A, group C are most similar to the basalts, and group D are those which do not fit any pattern.
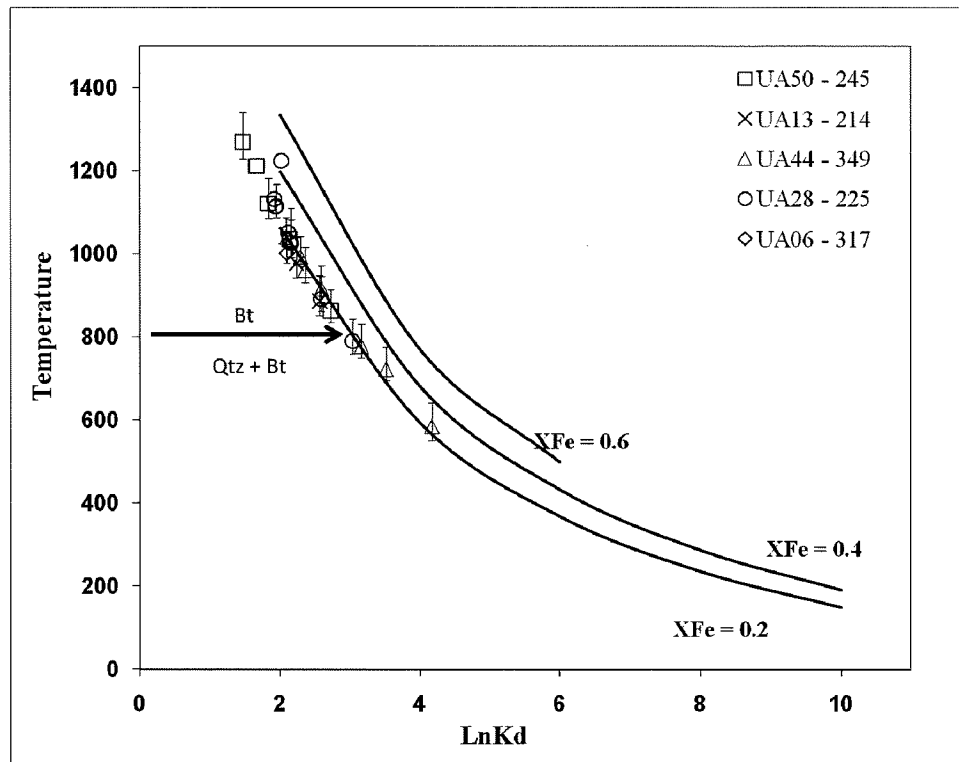
Figure 3.2 Minimum crystallization temperatures of coexisting biotite-apatite pairs. The error a bars were calculated using equation 2.3.

Table 3.2 Minimum crystallization tempertures calculated from biotite apatite compositions

Sample	lnKd	T (°C)	+	-	Avg. T (°C)	Sample	lnKd	T (°C)	+	-	Avg. T (°C)
UA50 245 - 01 A	1.881	1098	61	33		UA44 349 - 04 B	2.336	961	53	28	865
UA50 245 - 01 B	1.787	1143	64	36	1121	UA44 349 - 05 A	2.393	961	54	29	
UA50 245 - 02 A	2.631	883	51	28		UA44 349 - 05 B	2.667	895	53	30	928
UA50 245 - 02 B	2.824	843	51	28	863	UA44 349 - 06 A	2.513	938	54	30	
UA50 245 - 03 A	1.469	1268	71	40		UA44 349 - 06 B	4.166	585	37	19	762
UA50 245 - 03 B	1.479	1271	72	41	1270	UA44 349 - 07 A	3.512	723	54	33	
UA50 245 - 04 A	2.219	1011	62	36		UA44 349 - 07 B	2.102	1002	42	17	862
UA50 245 - 04 B	2.064	1062	61	34	1037	UA44 349 - 08 A	2.588	891	39	17	
UA50 245 - 05 A	1.744	1186	67	38		UA44 349 - 08 B	2.273	983	44	20	937
UA50 245 - 05 B	1.604	1237	68	38	1212	UA06 317 - 01 A	2.041	1068	49	23	
UA13 214 - 03 A	2.306	952	53	28		UA06 317 - 01 B	2.132	1055	51	26	1061
UA13 214 - 03 B	2.160	1005	55	29	978	UA28 225 - 01 A	1.769	1176	55	27	
UA13 214 - 04 A	2.908	791	51	28		UA28 225 - 01 B	3.191	759	38	18	968
UA13 214 - 04 B	2.219	982	54	28	887	UA28 225 - 02 A	2.881	821	38	17	
UA44 349 - 01 A	2.157	1037	74	46		UA28 225 - 02 B	1.818	1172	54	27	997
UA44 349 - 01 B	2.231	990	48	23	1013	UA28 225 - 03 A	2.019	1092	50	24	
UA44 349 - 02 A	1.952	1090	49	23		UA28 225 - 03 B	1.614	1225	55	27	1159
UA44 349 - 02 B	2.168	1030	54	28	1060	UA28 225 - 04 A	2.138	1053	50	25	
UA44 349 - 03 A	2.423	955	55	31		UA28 225 - 04 B	2.100	1051	49	23	1052
UA44 349 - 03 B	3.120	786	56	33	870	UA28 225 - 05 A	1.787	1163	54	26	
UA44 349 - 04 A	3.202	769	57	34		UA28 225 - 05 B	2.081	1063	49	24	1113
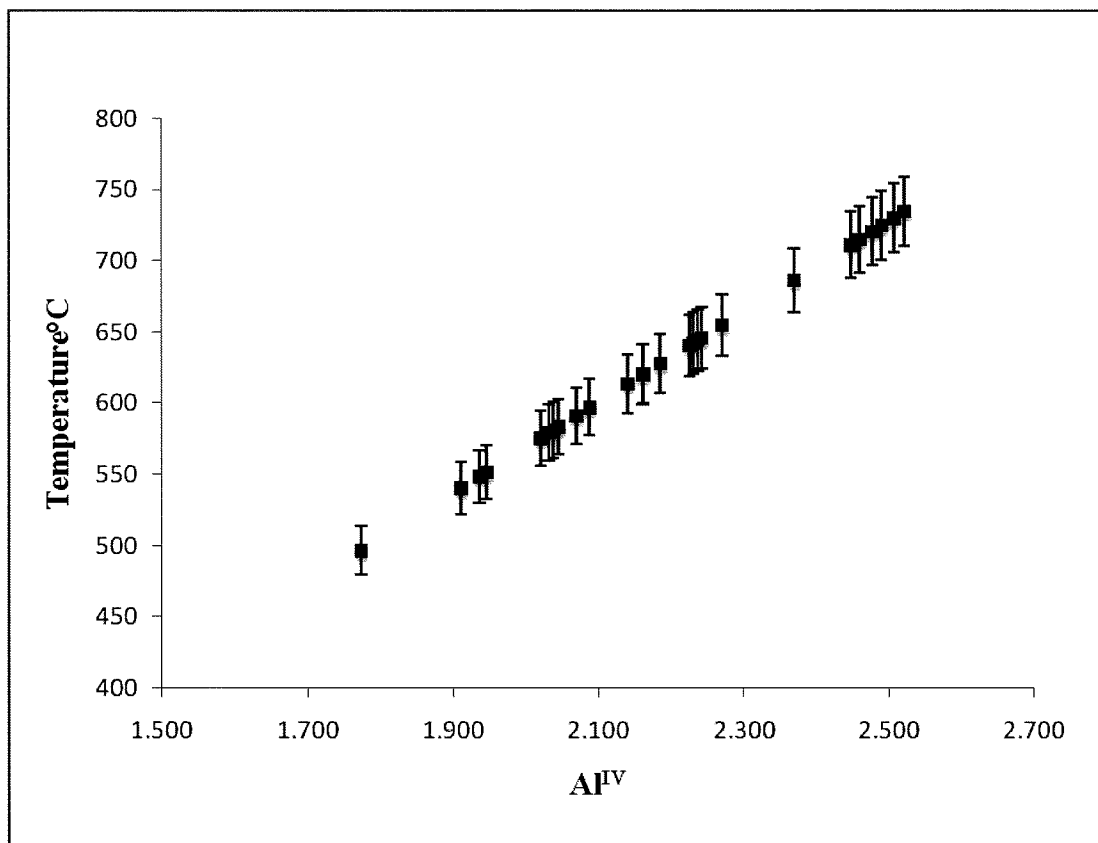
Figure 3.3 Minimum crystallization temperatures of chlorites. The error bars were calculated based on a maximum of 3% error associated with the microprobe (D.J. MacDonald pers. Communication).

Table 3.3 Minimum crystallization temperatures calculated from chlorite compositions

No.	Sample	Fe2	Mg	AlIV	T°C	+/-
2	UA52 - 383	2.986	6.512	2.161	620	21
3	UA52 - 383	2.926	6.749	2.089	597	20
4	UA52 - 383	3.026	6.636	2.033	580	19
5	UA52 - 383	2.793	6.615	1.911	541	18
6	UA52 - 383	2.950	6.440	2.141	614	20
7	UA52 - 383	3.223	6.376	2.242	646	21
8	UA52 - 383	2.866	6.821	2.021	576	19
9	UA52 - 383	3.039	6.391	1.937	549	19
10	UA52 - 383	2.960	6.586	2.185	628	21
11	UA52 - 383	2.846	6.717	2.039	582	20
12	UA80 - 613	3.402	5.796	2.046	584	20
13	UA80 - 613	3.336	6.256	2.230	643	21
14	UA80 - 613	3.670	5.155	1.773	497	17
15	UA80 - 613	3.621	5.376	2.459	715	24
16	UA80 - 613	3.621	5.376	2.459	715	24
17	UA80 - 613	3.576	5.738	2.071	592	20
18	UA80 - 613	2.881	6.871	1.946	552	19
19	UA80 - 613	3.134	6.292	2.162	621	21
20	UA06 - 307	3.996	5.159	2.447	711	23
21	UA06 - 307	3.026	6.142	2.520	735	24
22	UA06 - 307	3.734	5.339	2.476	721	24
23	UA06 - 307	3.829	5.265	2.506	730	24
24	UA06 - 307	3.670	5.379	2.476	721	24
25	UA06 - 307	3.572	5.169	2.489	725	24
26	UA06 - 308	2.890	6.285	2.236	644	21
27	UA06 - 308	2.494	6.650	2.225	641	21
28	UA06 - 308	3.488	5.616	2.368	686	23
31	UA06 - 308	3.242	5.759	2.270	655	22

Group A consists of samples UA06 307 and UA52 383, and are most similar to fresh pyroxene-bearing porphyritic rock from Afton (Fig. 3.4). The samples share peaks in W and Sr levels, and are depleted in Cs relative to other large ion lithophiles (LIL). Relative to the fresh porphyrytic rock the samples are highly enriched in W, slightly more enriched in LIL, and slightly depleted in Sr. Assuming that a fresh pyroxene porphyritic rock was the primary rock, these changes illustrate the effects of hydrothermal alteration with W and the LIL being mobile elements.

Group B consists of samples UA06 308 and UA28 234, which are also most similar to a pyroxene-bearing porphyritic rock but are different from group A (Fig. 3.5). Compared to group A, they have higher W peaks, much lower Sr peaks, and a peak in Pb concentration. The similarity between the pyroxene porphyritic rock and group A is the peak pattern with the exception of Pb. Peak levels are notably different but involve the same trace elements. Relative to the fresh rock pyroxene porphyry, group B samples are depleted in Cs and are slightly depleted in high field strength elements (HFS). Assuming that the samples also began as a fresh pyroxene-bearing porphyritic rock, the differences are evidence that the samples have undergone alteration by similar hydrothermal fluids with W and the LIL being fluid-mobile.

Group C consists of samples UA28 225, UA50 245, and UA80 613 which are most similar to the basalt control sample (Fig. 3.6). However, no samples from this study are from the basalt unit (other than the control sample); therefore, the similarities are strictly due to alteration effects. Unlike the other groups, these samples have a significant peak in Ba levels as well as the common Sr peak, which also links the samples to the fresh pyroxene-bearing porphyritic rock. The LIL elements are also notably enriched compared to other samples and the basalt control sample. These samples probably are pyroxene porphyry and have since been altered by hydrothermal fluids that have introduced trace elements from the basalt intrusion.
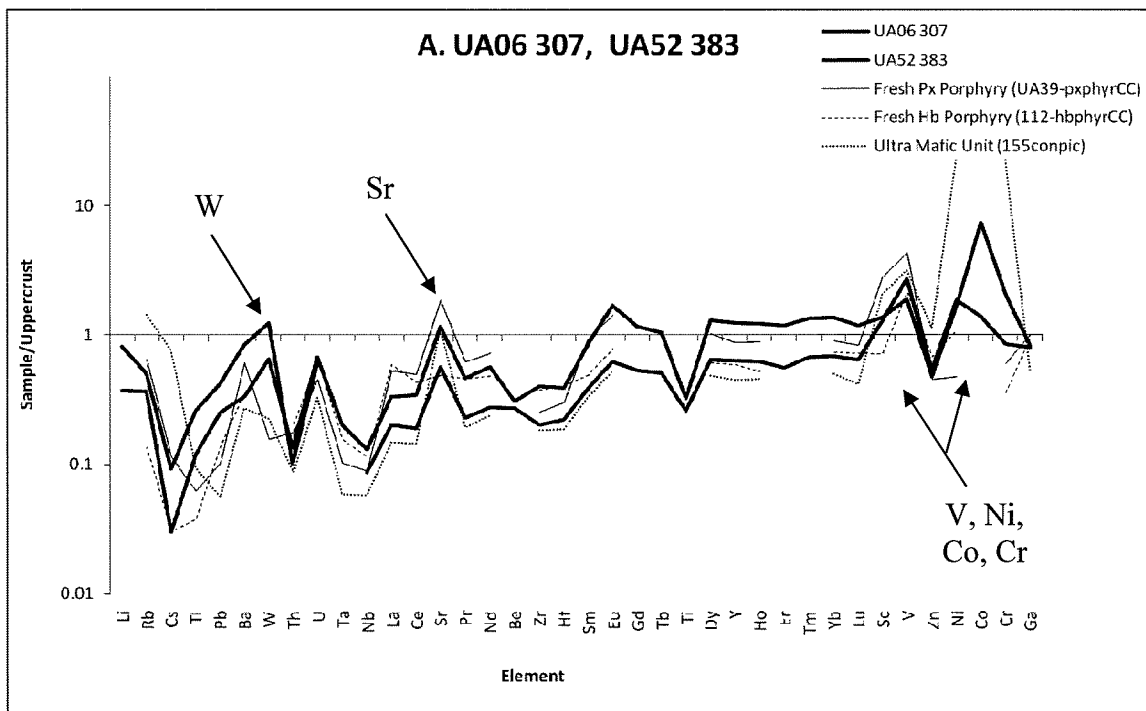
Figure 3.4 Group A. These samples are most similar to the fresh pyroxene porphyry control sample (UA39-pxphyrCC), but are different from group B.
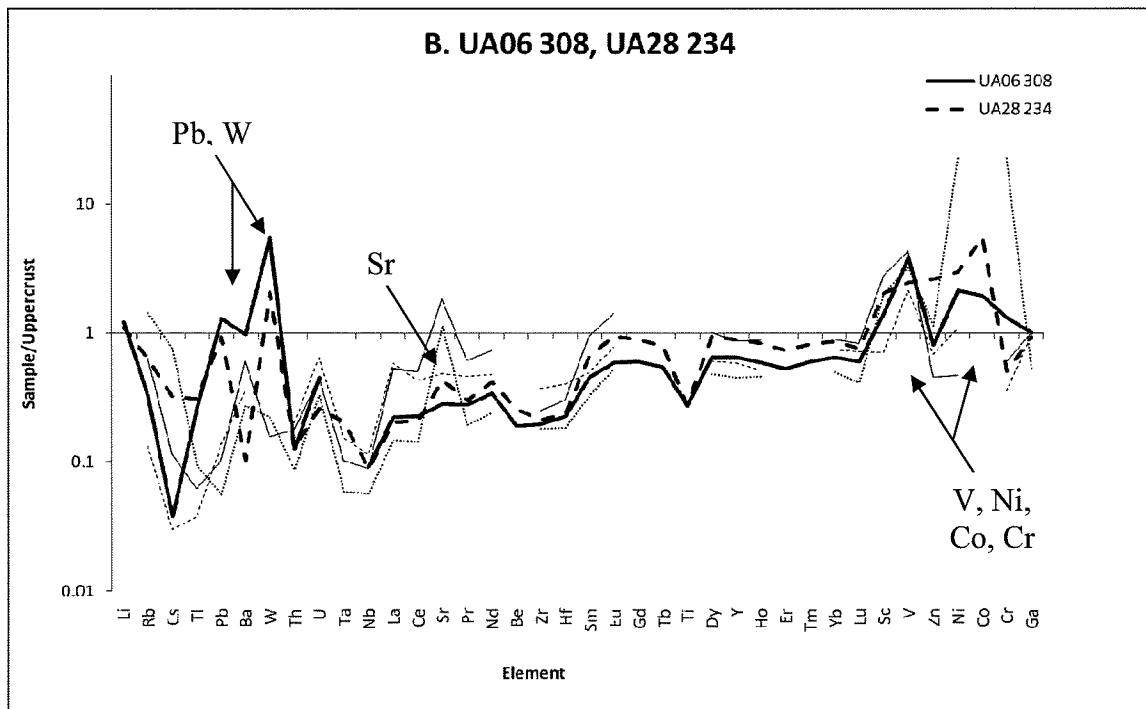
Figure 3.5 Group B. These samples are most similar to the fresh pyroxene porphyry control sample (UA39-pxphyrCC), but are different from group A.
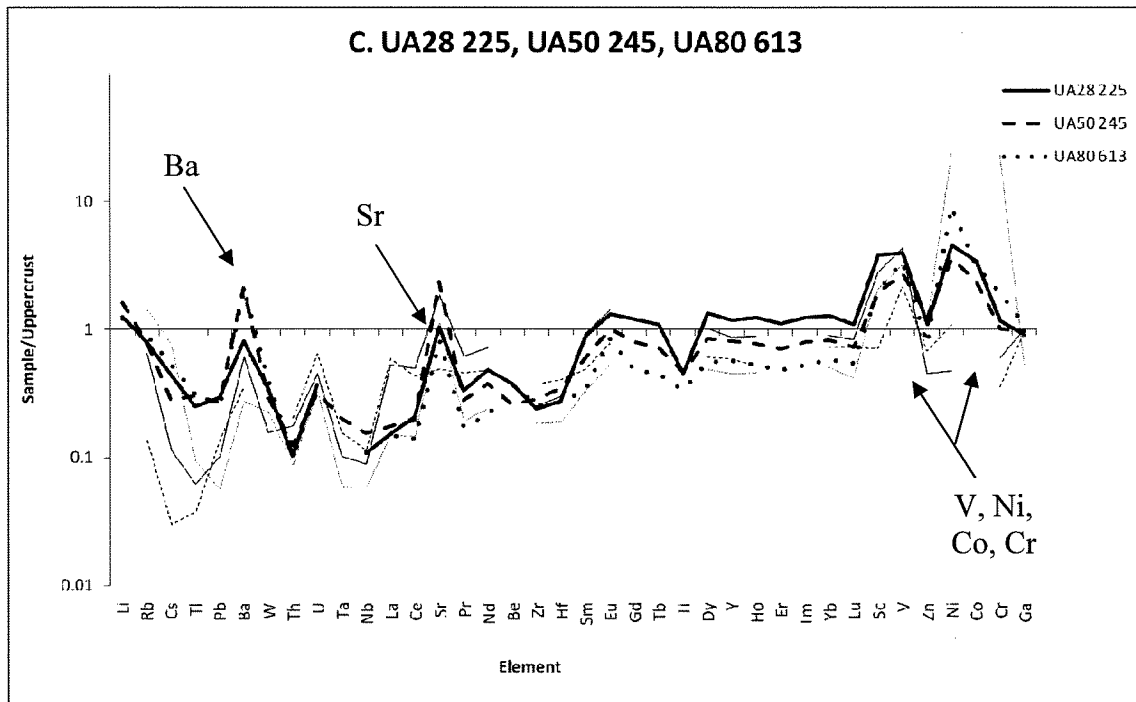
Figure 3.6 Group C. These samples are most similar to the ultramafic unit control sample (i.e. the basalt intrusions).

Group D consists of samples UA06 306 and UA44 349, which could not be grouped with the others (Fig. 3.7 and Fig. 3.8). UA44 349 is most similar to samples from group A in that it shares a similar peak pattern. However, it noticeably depleted in LIL elements, which is reminiscent of group C. Most likely it began as a pyroxene-bearing porphyritic rock. On the other hand, UA06 306 displays a completely different pattern than the other samples. It is significantly more enriched in Pb, W, and most REE. This sample is also contains abundant chalcopyrite and magnetite, both of which can host abundant REE.
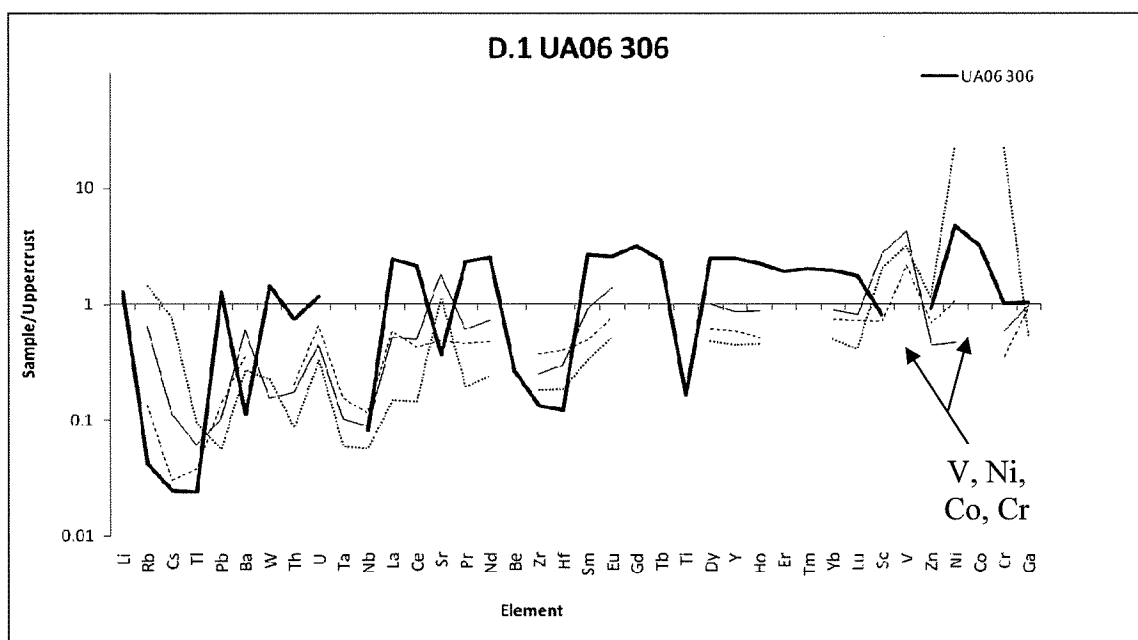
Figure 3.7 Group D.1. This sample is characterized by abundant chalcopyrite and magnetite. It is the only one that exhibits enrichment in most elements relative to the upper crust.
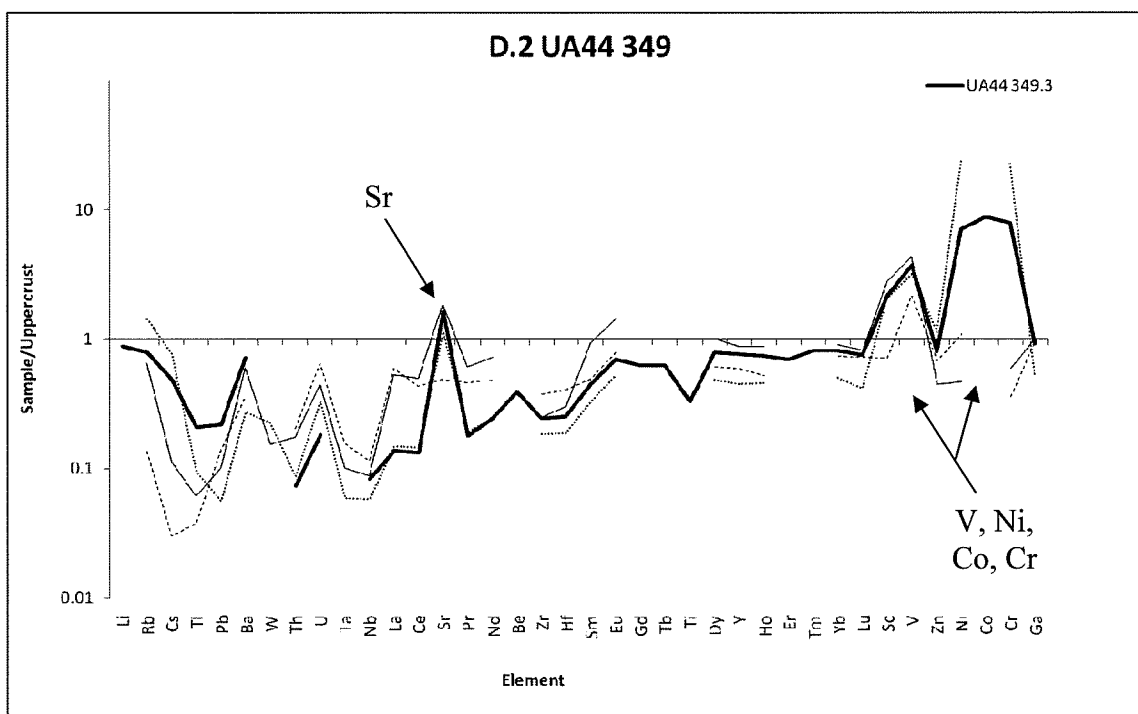
Figure 3.8 Group D.2. This sample does not fit into the other groups. It is most similar to the fresh pyroxene porphyry control sample (UA39-pxphyrCC).

Overall, the REE patterns of most samples are similar to the fresh pyroxene porphyry control sample. The REE content of each sample is controlled by apatite, which is relatively unaltered. Therefore the depleted nature of the bulk REE values show that apatite is a refractory phase, and hydrothermal fluids removed the REE from the system. The samples in group D are all dioritic, but exhibit patterns similar to the high-Mg basalt intrusions in addition to the fresh pyroxene porphyry. Thus, the difference in the REE pattern of group D gives insight into the chemistry and more importantly the alteration effects of the high-Mg basalt intrusions.

CHAPTER 4 – DISCUSSION

It has been proposed that the PGE at Afton came from the high-Mg alkali basalt dyke since the highest grades are found near it. However, the characteristics of typical Cu-Au-Pd±Pt porphyry deposits correlate very well with those of the Afton deposit as outlined in Table 4.1. Therefore, it is very possible that the PGE were derived from the original porphyry melt rather than being introduced from the basalt. Furthermore, the Afton deposit crystallized from a very sodium-rich melt, indicated by the abundant albite. Fluid inclusion studies show that precious metals can be transported as chloride complexes by hot (400-700°C) magmatic-hydrothermal fluids that are hypersaline (up to 70 wt% NaCl equivalent; Economou-Eliopoulos, 2005). The Na^+ needed to albitize the rocks would require an anion to be charge balanced. Cl^- is the most likely anion. This suggestion is reinforced by the chlorine poor nature of the biotite and apatite which indicates a chloride-rich free fluid phase (rather than having chloride dissolved in a melt; Boudreau *et al.*, 1995). Therefore, the fluids present at the early stages of alteration at Afton, during the albitization of plagioclase, would provide a potentially good medium for PGE transport. Because these fluids reacted pervasively through the entire IMB, PGE are probably dispersed throughout the entire deposit at trace levels. On the other hand, the basalt intrusion would have been a potential source for iron and magnesium. These elements, when dissolved in solution, reduce the solubility of Pd and Pt by reducing the activity of free chloride ions thereby promoting the precipitation of these elements (Economou-Eliopoulos, 2005). Therefore, any PGE that were remobilized by hydrothermal fluids may have been preferentially precipitated close to the dyke as the cation complexity of the fluid changed from being Na-bearing to Na-Fe-Mg-bearing (i.e., a salting-out effect; Table 4.1).

4.1 Petrography

New gold geologists determined that the quartz stock works are a significant source of sulphides, gold, and PGE (J. Hanley pers. communication). The petrographic evidence suggests that the sulfides, gold and associated minerals contained within the quartz veins were originally formed during the chlorite breccia event and were then dissolved, transported and re-precipitated

Typical Characteristic of Porphyry Cu-Au-Pd±Pt Deposits	Afton Deposit (This Study)
• Associated with alkaline rocks, in particular alkaline porphyry systems, SiO_2<65 wt.%	√
• Enriched mantle source or contribution by crustal material ($^{87}Sr/^{86}Sr$ and $^{207}Pb/^{204}Pb$)	?
• Parent magma are volatile rich, moderately fractionated, characterized by high halogen (F,Cl), REE and Th Values	√
• Commonly show elevated levels of Cr and Ni	√
• Common alteration minerals: Albitic (Sodic) and Calc-silicate (Actinolite, epidote, diopside, garnet), K-spar, and Biotite	√
• Cu and precious metals are transported as chloride complexes by relatively hot (400-700 degrees) and saline to hypersaline (>70 wt.%) hydrothermal fluids	?
• Predicated during main stage mineralization as an association of bornite, chalcopyrite, pyrite, and magnetite reaching up to 10 Vol.% as veinlets and disseminations, associated with potassic alteration type	X
• Textural relations between Cu-minerals and main Pd-bearing mineral, merenskyite, and Au-Ag tellurites, indicates that precious metals are closely associated with copper vein-type chalcopyrite and bornite	X
• Deposition occurs at earliest stages of alteration and mineralization in central parts of deposits	?
• Hydrothermal breccias are particularly abundant in large alkaline Au-Cu deposits	√

Table 4.1 Typical characteristics of a Cu-Au-Pd±Pt deposit as outlined by (Economou-Eliopoulos, 2005).

by the quartz-precipitating fluids. This indicates the strength of these secondary fluids as a solvent for Cu and Au. Had the PGE been hosted by any mineral associated with the original sulphides, they too may have been remobilized by the quartz-precipitating fluids. Wood (1994, 2002) showed that fluids in equilibrium with pyrite, chlorite, albite, epidote, and calcite would be incapable of transporting significant amounts of PGE as chloride complexes (Economou-Eliopoulos, 2005). Therefore, even though chloride could not have carried metals during the chlorite brecciation/mineralization event, it could have carried the metals with the fluids that

precipitated quartz since these fluids are more than capable of carrying metals as chloride complexes.
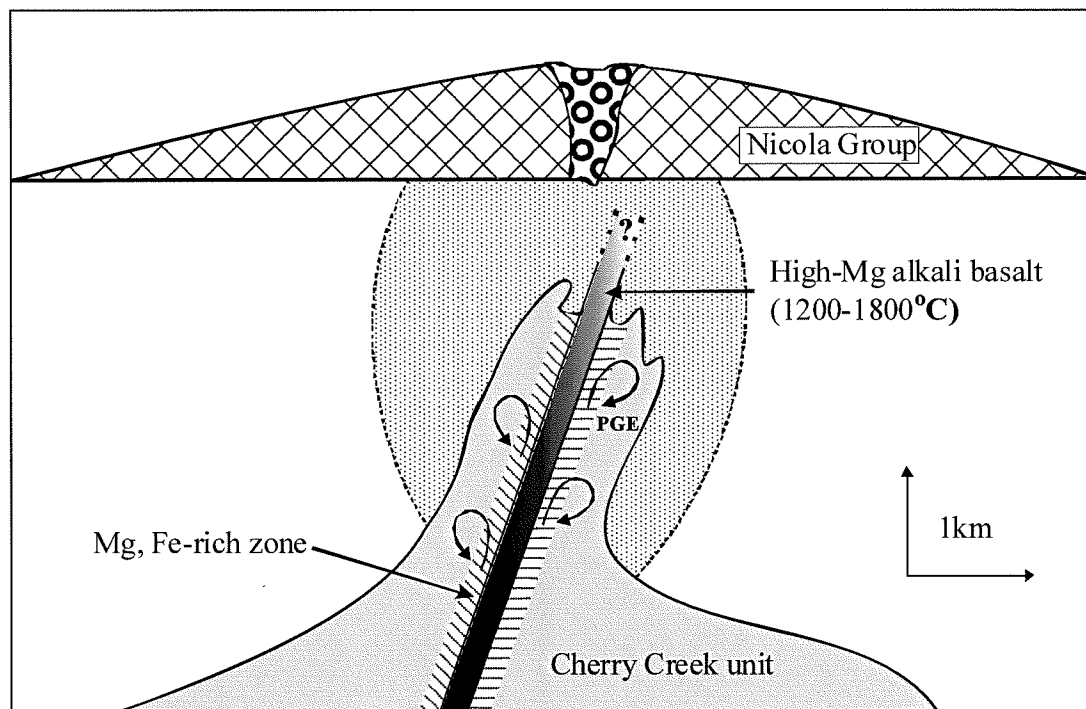
Figure 4.1 A conceptualized model of PGE concentration at Afton. Hot hydrothermal fluids released by the basalt intrusion mobilize PGE and repricipitate in the Mg, Fe-rich zones.

The timing of the formation of the vein styles and the minerals they host provides insight into the history of the deposit. Each set of veins represents a separate hydrothermal event. The first set of veins introduced carbonate. A probable source for the CO_3^{2-} is the Nicola Group (Kwong, 1987). Heated fluids released from the intrusion of the IMB would have dissolved it from the overlying rocks. The second set of veins identified in this study was that containing chlorite associated with the formation of ore-syngenetic breccias. Brecciation is a normal stage in the evolution of porphyry deposits and occurs due to increasing (confined) fluid pressure as the intrusion crystallizes. Eventually the fluid pressure becomes great enough to fracture (brecciate) the rock and the fluids are released. However, a felsic intrusion like the IMB would be incapable of providing the Mg and Fe required to produce abundant chlorite. Therefore, an external source

for the chlorite in the porphyry must exist since the Mg and Fe could not have been derived from the felsic rocks themselves. The basalts could have been the source for thie Mg and Fe. One hypothesis is that Mg/Fe-rich fluids were driven upwards by the intrusion of the basalt using the breccia pipes as conduits. Breccia pipes usually contain abundant ore minerals and are commonly timed with the main stage of mineralization (Sinclair, 2007). The third vein set observed introduced biotite and quartz in addition to dissolving and reprecipitating other phases such as carbonate, chlorite and the ore minerals. These veins have the most significance as they were most likely formed from fluids chemically associated with the basalt intrusions (sect. 4.2). However, quartz cannot be precipitated from fluids in equilibrium with basalt (J. Hanley pers. communication), therefore the basalt probably dissolved the silica from the surrounding rock. The poorly defined contact between chlorite and quartz veins suggests that the intrusion of the basalt immediately followed the brecciation event. It is possible that destabilization of the IMB due to brecciation enabled the intrusion of the basalt. The latest veins to form contain crystalline carbonate and are of little significance in terms of alteration and ore mineral distribution.

4.2 Temperatures

Assay results show that high-grade PGE areas in the Afton deposit are associated with the quartz stockworks (New Gold Corp., 2006). These veins also contain chalcocite, bornite, chalcopyrite, tetrahedrite-tennantite, and are enriched in Hg, As, and Sb (See Table B.2; Mackenzie and Hanley, in prep.; New Gold Corp., 2006). Petrographic results from this study determined that hydrothermal biotite formed from the same event. The minimum crystallization temperatures calculated from biotite-apatite thermometry determined that the biotite grew between 723-1271°C (Fig 3.2 and Table C.1.1). However, the temperatures calculated from the chlorite thermometer are only 497-735 °C. This temperature range coincides to the brecciation (and main mineralization) event. It was also determined that the chlorite formed prior to secondary biotite crystallization. Therefore, the Afton ore-forming system had already cooled below the temperatures calculated for the biotite (and quartz veins containing ore minerals). This shows that an external heat source acted upon the rock of the Afton deposit, which could have dehydrated the country rock to obtain and transport the components needed to grow biotite. A likely source of the heat is the Mg-rich basalt, which can intrude at temperatures up to ~1800 °C (J. Hanley, pers. communication). However, a study by Dachs and Benisek (1995) showed that

the temperature at which biotite will form is greatly reduced in the presence of quartz (Fig. 4.1; Dachs and Benisek, 1995). This is because, at higher temperatures, K (that would otherwise stabilize biotite) combines with SiO_2 to form sanidine. However, in the samples of this study biotite appears to have grown in the wall rock whereas quartz precipitated in the veins. This indicates that the biotite formed earlier when temperatures were higher, and that the quartz precipitated last at cooler temperatures. This provides an explanation for the large range in biotite crystallization temperatures calculated for individual samples using the biotite-apatite geothermometer. The biotite that formed at higher temperatures formed in the absence of quartz. When quartz and biotite began to precipitate together, the data from the biotite-apatite pairs shows that temperatures were considerably lower (Fig 3.2).

4.3 Trace element analysis

The information obtained from the trace element analyses of altered and mineralized samples does not indicate clearly the presence of any dominant mineral controlling element abundance. It is suspected that apatite was the main host to the REE and is now a refractory mineral that was not modified during alteration aside from halogen-hydroxyl exchange with biotite. On the other hand, the sample groupings by trace element pattern do provide a sense of the styles and intensities of alteration. For example, the enrichment of large ion lithophiles (LIL) in altered samples compared to the fresh samples is most likely the result of their interaction with fluids released from the basalt intrusions considering that the basalt control is also enriched relative to the other control samples, and that this basalt was rich in alkalis and LIL. Furthermore, rocks that were once similar to the fresh pyroxene-bearing control now have trace element patterns similar to the basalt intrusion. The consistent enrichment of Ni, Co, and sometimes Cr, controlled by the presence of sulfides and magnetite, provides further evidence that the Afton Deposit is a Cu-Au-Pd±Pt porphyry deposit that was modified chemically by a mafic associate, possibly the basalt.

Alteration Facies	Event	Style	Fracture Filling	Mineralization	Style
Iron Oxide	supergene oxidation	pervasive, ffl, lgb	hematite, limonite, goethite	native copper, cuprite-(specularite, hematite)	ffl, dsm
Silicification (Silica+sericite)	colliform veins	ven; stk	quartz-carbonate-anhydrite-(barite?); colloform banding; vugs; chalcedony	pyrite	
Argillic	white-clay net fracturing	ffl, bxk	quartz-dolomite-calcite-white clay	none, makes friable core	net, ffl
Dolomite + sericite + quartz; (chlorite + calcite destructive)	quartz stockworks associated with steep faults	stk, ven	quartz-dolomite-calcite-clay; banded, jigsaw vein breccias	chalcocite-(bornite, chalcopyrite, pyrite); enrichments in Hg, As, & Sb; tetrahedrite-tennanite	
	specularite veins	ven	quartz-dolomite-calcite-specularite	coarse chalcopyrite, pyrite	dsm
Propylitic; (chlorite + calcite destructive)	epidote overprint on calcareous and magnetite-rich assemblages	halo, ffl, agr	epidote-actinolite-chlorite-calcite-(ankerite)	bornite after chalcopyrite	dsm
Potassic	chalcopyrite crackle breccias	bxk, ffl	biotite-(chlorite after biotite)	chalcopyrite	bxk
Phyllic; (dolomite + sericite + Silica)	pyritic stockwork; (tan to orange halos of Ksp); tourmaline veins;	stk, bxj	pyrite-quartz-carbonate-chlorite-tourmaline	gold; pyrite >> chalcopyrite; some molybdenite	dsm, ffl
Ksp + actinolite + chlorite; (biotite + calcite destructive)	irregular Ksp bands (i.e. orange halos)	ven, bxk	magnetite, specularite-actinolite-chlorite-carbonate-quartz	magnetite, pyrite, chalcopyrite, bornite	ffl
Iron oxide	magnetite stockwork	ven, stk, bxk	magnetite-calcite-biotite magnetite-actinolite-apatite-calcite	chalcopyrite, pyrite	dsm
Early potassic "front"	biotite hornfels; siliceous; white spotted	pervasive			

Table B.3 Afton alteration and mineralization – styles and events (after New Gold Inc., 2006). Abreviations: ffl – fracture filling; ven – vein; stk – stock work; bxk – crackle breccia; bxj – jigsaw breccia; dsm – disseminated; lgb – lazy gang banding.

CHAPTER 5 – CONCLUSIONS

5.1 Conclusions

1. The Afton deposit possesses many of the qualities of a Cu-Au-Pd±Pt deposit. Therefore, it is reasonable to consider that the PGE were deposited during the intrusion of the CCU and have since been reconcentrated by hydrothermal fluids that were derived from the porphyry and driven by the heat radiating from the basalt intrusions. However, key differences between Afton and other alkalic Cu-Au-PGE porphyry deposits is its lack of zoned alteration halo and a significant chlorite-rich brecciation event (Table 4.1, #2)

2. The first alteration event introduced carbonate that formed in veins. Following this, a brecciation event involving intense chlorite alteration introduced the ore minerals. This differs from the conventional alkalic porphyry deposits in which the ore stage coincides commonly with potassic alteration. The third alteration event may have been related to the emplacement of the basalt intrusions. It introduced biotite followed by quartz, and as well, it redistributed sulfides. More importantly, it could have mobilized PGE and reconcentrated them close to the basalt intrusion. The last event formed crystalline carbonate veins. No noticeable pervasive or alteration or reprecipitation of ore minerals was associated with these veins.

3. The chlorite (brecciation stage) crystallized first at 497-730°C. Biotite (with apatite) crystallized second at 723-1268°C. The Mg and Fe needed to grow chlorite may have come from fluids that were driven up preceeding the intrusion of the basaltic dikes and sills. The late addition of heat, which drove the fluids that precipitated biotite, could have radiated from basalt after the emplacement of the dykes and sills. Alteration events were associated with the redistribution of REE and LIL.

4. Cu-sulphides, Au, and PGE associated with quartz veins were mobilized by hydrothermal fluids related to the intrusion of the basalt, and may have been redeposited close to the intrusion. The presence of Mg and Fe, introduced by the basalt intrusions thereby forming a skarn-style zone at the contact with the porphyry, would induce the

precipitation of chloride metal complexes carried by the same fluid that precipitated biotite and quartz.

5.2 Future work

There are many aspects of the Afton deposit that are still poorly understood. Further studies should focus on confirming whether the bulk of the PGE are primary or were introduced by the basalt intrusions. This could be done by comparing the PGE minerals near to and far from (and unaffected by) the basalt intrusions to see if the PGE phases are the same in all areas.

Many aspects of the samples and the deposit in general possess characteristics of skarn alteration/mineralization. These include the development of wollastonite and pervasive carbonate alteration. A future study might investigate the contact zone to determine the extend of skarn formation. In addition, constraining the extent of the mineralized zone influenced by Mg and Fe from the basalt and relating it to PGE grade may clarify the importance of the basalt for PGE enrichment. An approach would be to focus on ankerite alteration and its distribution.

REFERENCES

Adams, D. 2008. Hydrothermal Veins and Alteration [online]. Available from http://www.dmtcalaska.org/course_dev/explogeo/class08/notes08.html. [cited March 1, 2009]

Anderson, J.L. and Smith, D.R. 1995. The effects of temperature and fO_2 on the Al-in-hornblende barometer. American Mineral., **80**: 549-559.

Behre Dolbear & Company Ltd. 2004. Mineral resource estimate for the Afton copper/gold project Kamloops, B.C. Technical Report for DRC Resource Corporation.

Boudreau, A.E., Love, C., and Prendergast, M.D. 1995. Halogen geochemistry of the Great Dyke, Zimbabwe. Contrib Mineral Petrol, **122**: 289-300.

Carr, J.M. and Reed, A J. 1976. Afton: A supergene copper deposit. *In* Porphyry deposits of the Canadian Cordillera. *Edited by* A. Sutherland Brown. Canadian Institute of Mining, Special Vol. 15, pp. 376-387.

Dachs, E. and Benisek, A. 1995. The stability of annite+quartz: reversed experimental data for the reaction 2 annite+3 quartz = 2 sanidine+3 fayalite+ 2 H_2O. Contrib Mineral Petrol, **121**: 380-387.

De Caritat, P., Hutcheon, I., and Walshe, J.L. 1993. Chlorite geothermometry: a review. Clays and Clay Minerals, **41**(2): 219-239.

Deer, W.A., Howie, R.A., and Zussman. 1996. An introduction to rock-forming minerals. Prentice Hall.

EarthRef.org. 2009. Geochemical Earth Reference Model (GERM) [online]. Available from http://earthref.org/GERM/index.html. [cited February 25, 2009].

Economou-Eliopoulos, M. 2005. PGE potential of porphyry deposits. *In* Exploration for deposits of platinum-group elements. Mineralogical Association of Canada Short Course Series, Vol. 35, pp. 203-246.

Geologic Survey of Canada. 2007. Cordilleran Geoscience [online]. Available from http://gsc.nrcan.gc.ca/cordgeo/index_e.php. [cited March 1, 2009].

Le Bas, M.J. 2000. IUGS reclassification of the high-Mg and picritic volcanic rocks. Journal of Petrography, **41**(10): 1467-1470.

Melville, D.M. 1992. Record Summary. B.C. Geologic Survey. MINFILE No. 094D 111 [online]. Available from http://minfile.gov.bc.ca/Summary.aspx?minfilno=094D%20%20111. [cited 1 March 2009].

Mortensen, J. K., Ghosh, D. K. and Ferri, F., 1995. U-Pb geochronology of intrusive rocks associated with copper- gold porphyry deposits in the Canadian Cordillera; *in* Porphyry Deposits of the Northwestern Cordillera of North America, T. G. Schroeter (ed.), Canadian Institute of Mining, Metallurgy and Petroleum. Special Volume 46, p. 142-158.

National Research Council Canada. 2008. Instructions to authors: Canadian Journal of Earth Science [online]. Available from http://pubs.nrc-cnrc.gc.ca/eng/journals/instructions/cjes.html. [cited March 1, 2009].

New Gold Inc. 2006. Table 1. Afton alteration and mineralization. Private company report. 1 p.

Nixon, G. T., 2003. Platinum-group elements in the Afton Cu-Au porphyry deposit, southern British Columbia. *In* Geological Fieldwork 2003. Ministry of Energy and Mines, Victoria, B.C. p. 263-299.

Northcote, K.E. 1977. Geology of the southeast half of Iron Mask Batholith. *In* Geologic Fieldwork 1976 , B.C. Ministry of Energy, Mines and Petroleum Resources. p.41-46.Owsiacki, G. 2003. 092INE [online]. Available from http://www.empr.gov.bc.ca/Mining/Geoscience/MINFILE/ProductsDownloads/PublicationsList/ Pages/092ine.aspx. [cited March 1, 2009].

PacMag Metals Limited. 2009. Frequently Asked Questions [online]. Available from http://pacmag.com.au/faqs.11.html. [cited March 9, 2009]

Preto, V.A. 1977. The Nicola Group: Mesozoic volcanism related to rifting in southern British Columbia. *In* Volcanic Regimes in Canada. W.R.A. Baragar, L.C. Coleman, J.M. Hall (ed.), The Geological Association of Canada, Special Paper No. 16, p. 39.

Robinson, N. 2007. Record Summary. B.C. Geological Survey. MINFILE No. 092INE023. Available from http://minfile.gov.bc.ca/Summary.aspx?minfilno=092INE023 [cited March 1 , 2009].

Ross, K.V. 1993. Geology of the Ajax East and Ajax West, silica-saturated alkalic copper-gold porphyry deposits, Kamloops, south-central British Columbia. M.Sc. thesis, Department of Geological Sciences, The University of British Columbia, Vancouver, B.C. 211 p.

Seigel, C. 2005. Tectonic evolution of northern British Columbia [online]. Avaible from http://www.emporia.edu/earthsci/student/seigel1/Tectonic_Evolution.htm [cited March 10, 2009].

Sinclair, W.D., 2007, Porphyry deposits, *In* Goodfellow, W.D., ed., Mineral Deposits of Canada: A Synthesis of Major Deposit-Types, District Metallogeny, the Evolution of Geological Provinces, and Exploration Methods: Geological Association of Canada, Mineral Deposits Division, Special Publication No. 5, p. 223-243.

Stanley, C.R., Lang, J.R., and Snyder, L.D. 1993. Geology and mineralization in the northern part of the Iron Mask Batholith, Kamloops, British Columbia. *In* Geological Fieldwork 1993. B.C. Geological Survey Paper 1994-1. p. 269-274.

Tarduno, J.A., Duncan, R.A., Scholl, D.W. *et al.* 2009. Explanatory Notes. *In* Proceedings of the Ocean Drilling Program, Initial Reports. Ocean Drilling Program. Texas A&M University, USA. Vol.197, Ch 2, pp. 54.

Winter, J.D. 2001. An Introduction to igneous and metamorphic rocks. Prentice Hall. Toronto.

Zhu, C. and Sverjensky, D.A. 1992. F-Cl-OH partitioning between biotite and apatite. Geochimica et Cosmochimica, **56**: 3435-3467.

APPENDIX A - SAMPLE DESCRIPTIONS

A.1 Hand sample descriptions

A.1.1 UA06 – 306 metres

A.1.1.1 Slab A

This rock is a breccia in which the clasts are completely detached from one another ("matrix-supported") and little movement has resulted in a rock known as a "crackle" breccia. The matrix is very fine-grained black to greenish black due to an abundance of chlorite. The clasts are up to 2 cm in size, angular, and composed of fine-grained potassium feldspar with plagioclase. Chalcopyrite is the main economic mineral in this sample, present at a modal abundance of approximately 1%.

A.1.1.2 Slab B

Slab B of sample UA06 306 is composed largely of the same fine-grained chlorite with carbonate rock seen in the fractures of Slab A. Sulphide mineralization is abundant, around 20% of the entire rock. It is disseminated suggesting that there formation is related to the [chorite + carbonate] event. White carbonate veins with pink impurities cross-cut the rock, including the sulphide minerals.

A.1.2 UA06 – 308 metres

Sample UA06 308 is a sub-matrix supported breccia with sub-angular clasts that grade in size from 2mm to 2.5cm. It has a dark green to black matrix composed of very fine-grained aggregate of chlorite and carbonate. The clasts are grey, brown, or pink to red with white specks. Their texture is fine-grained and micro-porphyritic, with phenocrysts reaching up to 1.5mm in size. The mineralogy is dominated by plagioclase and K-feldspar. Potassic alteration of the wall rock and clasts is intense in some areas, but no pattern is evident. There are carbonate veins are present, but they are not abundant. Chalcopyrite and bornite are the main ore minerals. They occur in micro-fractures and make up about 1% of the sample.

A.1.3 UA06 – 317 metres

Sample UA06 317 is a fine-grained black, grey, grayish salmon rock with minor carbonate veins cutting it. Phenocrysts reach up to 4mm but the average grain size is 1mm. Sulphide mineralization occurs as finely disseminated blebs that are up to 0.5mm. The modal percent of ore minerals in this sample is 0.5%. In addition to the carbonate veins, there is a loose network of microfractures.

A.1.4 UA13 – 214 metres

Sample UA13 214 is a pink rock with green phenocrysts that become larger, up to 3mm, and more abundant near fractures. It is evident that the original rock had a microporphyritic texture, however, most of the original textures were destroyed by intense potassic alteration. Native copper occurs in fractures in association with specular hematite. Because this sample contains native copper, it must be from the supergene zone. The total mineralization was less than 1%. Quartz and carbonate veins are present but they are minor.

A.1.5 UA44 349 metres

Sample UA44 349 is a fine to very fine grained microporphyritic rock. Sections of the sample have undergone intense chlorite alteration turning the rock greenish black. The other areas are greenish grey with pink grains. The pink grains are feldspars that have undergone potassic alteration. There are numerous microfractures that most likely acted as pathways for the alteration fluids. There are a few larger veins that are filled with vuggy quartz. Sulphide minerals, primarily chalcopyrite, form blebs up to 1.5cm. Modal abundance of ore minerals in this sample is 5%.

A.1.6 UA52 383 metres

Slab UA52 383 is a gray, fine grained, slightly porphyritic rock. The average grain size is 0.5mm. Some phenocrysts have grown up to 2mm. Potassic alteration of feldspars is seen throughout the rock, but is more intense within 0.5mm of veins that cut the sample. The veins appear to be from 2 separate events based on weak cross-cut relationships, however they contain similar mineralogy of chlorite, carbonate, quartz, and specular hematite. Sulphides, chiefly chalcopyrite, are dispersed throughout the rock along microfractures. Some blebs contain fine

grained specular hematite enveloping and intergrown with chalcopyrite and commonly pyrite as well. The mineralization mode is around 2%.

A.1.7 UA80 – 613 metres

Sample UA80 613 is a dark greenish gray fine grained rock speckled with white grains. Grains size reaches up to 0.5mm. The dominant mineral is plagioclase. Other minerals present are potassium feldspar, and biotite pseudomorphs that were most likely replaced by a species of carbonate. Patches of pink feldspar, from potassic alteration, form a 1cm zone around veins with sulphide minerals dominated by chalcopyrite. Fracturing is not well developed; which prevented extensive potassic alteration in this sample. Disseminated sulphides make up about 2% of the sample.

A.1.8 UA100 822 metres

Sample UA100 822 is a rock that has undergone intense alteration from fluids that traveled through large fractures. It is dominated by fine grain rock that is green speckled with white grains. Areas of wall rock have experienced heavy potassium alteration turning the rock pink. Two sets of veins cut the rock. One set, that appears associated with the chlorite, contains specular hematite with minor amounts of chalcopyrite. The specular hematite has precipitated preferentially in contact with rock, but is also disseminated throughout the chloritized rock. The second set, which is probably younger (See Fig. ##) contains apatite. Total mineralization in the rock is around 7%.

A.2 Thinsection Description

A.2.1 UA06 – 306 metres

Sample UA06 – 306 is composed of 50% opaque minerals, relict clasts, and a very fine-grain interstitial matrix of chlorite, quartz, and carbonate. The clasts are not very abundant and have been so intensely altered by carbonate that they are consider apart of the ground mass in Table##. The original compositon is assumed to have been diorite, by the presence of indistinguishable feldspar grains, but now they contain less than half of the original mineralogy. A good possibility is that this sample is from the middle of a large breccia pipe where the abundance of matrix is much greater than the clasts and fluids are hottest. The grain size of the

matrix is beyond the measurable limit of a standard light microscope. Larger grains of quartz, up to 0.5mm, as well as carbonate, with grains up to 0.25mm in diameter, have formed throughout the slide. Carbonate has also formed very thin, fine grain rims around the opaque minerals. Two sets of veins cut the rock including the matrix. The earlier set, based on crosscutting relationships, contains solely carbonate. These veins are seen cutting some but not all the carbonatized clasts and where they do cut the edges are crisp suggesting they are were formed at different times. The later and less abundant veins contain only quartz. The opaque minerals consist of approximate equal amounts of magnetite and chalcopyrite with minor amounts of pyrite.

A.2.2 UA06 – 307 metres

Sample UA06 – 307 is part wall rock, and part breccia. The wall rock and clasts have a monzodiorite composition and a microporphyritic texture. The groundmass contains more albite than potassium feldspar, and chlorite that have an average grains size of 20μm. The phenocrysts are dominantly albite, but some of the clasts and areas of wall rock near the contact contain more potassium feldspar. Generally, the phenocrysts are 0.5mm. Trace amounts of Reibecktite, a iron rich metamorphic amphibole, are present. In the wall rock carbonate and quartz have pervasively entered the rock in addition to the veins forming grains up to 0.25mm of quartz and 0.5 of carbonate, although most grains of both are finer. The age relationship between these phases is unclear in this sample. Frequently veins contain quartz and carbonate and the alteration is so pervasive that crosscutting relationships have been obscured. In the clasts, most all veins are filled with Chalcopyrite which is also seen replacing whole areas of the clasts. Between the clasts is a very fine grain mixture of chlorite, carbonate and quartz. Carbonate is also present as grains that range from 0.5mm to 50μm in size, whereas quartz is absent except for at the contact where it has formed a layer. Chalcopyrite is associated with minor chalcocite, pyrrhotite and gold.

A.2.3 UA06 – 308 metres

Sample UA06 – 308 is a breccia that has microporphyritic monzodiorite clasts in a chlorite/carbonate matrix. The clast size spans from 0.25mm to larger than 1.5 cm. Within the clasts the groundmass is composed of more albite than potassium feldspar with an average grain size of 50 μm. The phenocrysts are around 0.5mm up to 1mm in size, have a anhedral to

subhedral shape, and are dominantly albite. Separating the clasts is a matrix composed chiefly of chlorite with minor quantities of carbonate, quartz, apatite, and micro-laths of nepheline. Opaque minerals consist chiefly of chalcopyrite with small amounts of associated chalcocite, pyrite, and gold. These minerals are contained within the matrix as well as in abundant fracturing throughout the clasts. Carbonate and sulphides fill some of the fractures in the clasts. These veins terminate at the edge of a clast. There is some carbonate in the chlorite matrix, but it mostly occurs at the edge of a vein or as small, fine grain aggregates suggesting that the hot chlorite fluids remobilized it. Sericite alteration is weak to moderate in this sample.

A.2.4 UA06 – 317 metres

Sample UA06 – 317 is a microporphyritic diorite. The groundmass is beyond the measurable limit of a standard light microscope. SEM worked revealed that it is composed chiefly of albite, with minor amounts of potassium feldspar. The phenocrysts have an anhedral to subhedral shape and are generally around 0.3 mm in size, with the largest reaching up to 1mm. They are dominantly albite, with some potassium feldspar, clinoziosite, and smaller hydrothermal biotite grains. The biotite preferentially formed adjacent to apatite grains that are near a vein and only occurs in a small area of the slide. A network of fractures contains chlorite, carbonate and the opaque minerals. The carbonate and chlorite have formed separate "strands" with chlorite tending to form at the edges and carbonate in the middle of the vein. Some of the chlorite is stained yellow that maybe due to the inclusion of excess iron. Opaques minerals consist of chalcopyrite, chalcocite, and small amounts of gold. For the most part they are contained in the vein network with carbonate. Apatite contains micro-inclusions of albite. Biotite contains inclusions of ilmentite.

A.2.5 UA13 – 214 metres

Sample UA13 – 214 is a microporphyritic diorite. Most grains have an anhedral shape. In the ground mass the grains are 25μm on average and the phenocrysts are generally 0.5mm, however there are a few larger subhedral porphyroblasts of apatite that have grown up to 1.5mm and potassium feldspar porphryroblasts that reach up to 2.5mm. The mineralogy of the groundmass and phenocrysts contains more potassium feldspar than albite with relatively abundant apatite and biotite. Hematite occurs as earthy aggregates in the groundmass and as

specular hematite that is intergrown with the apatite porphyroblasts. Growing around the apatite what I believe is bournonite. The larger potassium feldspar porphyroblasts contain inclusions of apatite, intergrowths of biotite, and are altering to sericite that is coarser than the micro-inclusions seen throughout the rest of the slide. Biotite occurs as independently as well throughout the slide, but seems concentrated with larger grains in the areas where sericite alteration is more prevalent. Sericite alteration is intense in this sample. Carbonate veins are minor, and carbonate alteration occurs only local to the veins and is also minor. Opaque mineralogy is sparse in this sample. It consists of bournonite grains that have grown on the edge of apatite grains and speculartite that has grown on the cleavage planes of the apatite grains.

A.2.6 UA28 – 225 metres

Sample UA28 – 225 is a diorite with a microporphyritic texture that has been pervasively altered by carbonate fluids. Many of the phenocrysts have been replaced by fine grain carbon. The ones that remain are mostly albite with some apatite. The average grain size of the phenocrysts/pseudomorphs is 0.75mm and the shapes are anhedral to subhedral. The groundmass is dominantly albite, but still contains abundant carbonate. The albite grains are around 5μm and the carbonate is around 25μm. Biotite is present throughout the slide. It is thought to be hydrothermal and related to quartz veins because the grain size and abundance increases near these veins and is associated with apatite. The quartz veins also are host to the sulphide minerals which are dominantly chalcopyrite. Another set of veins contain carbonate, but there is no area of the slide that a clear relative age relationship can be worked out. Sericite alteration is intense in the sample.

A.2.7 UA28 – 234 metres

Sample UA28 – 234 is unlike any of the other samples. The original texture is completely destroyed. The groundmass is a brown very fine aggregate. Pseudomorphs, which are up to 2mm in size, have been completely altered to paler, creamier brown, fine grain aggregates. There is abundant veining with two different types. The earlier ones no longer contain their original minerals; instead they are filled by a fine grain aggregate that is similar in appearance to the pseudomorphs. The later stage veins contain fresh looking quartz and the ore minerals which are

pyrite, chalcopyrite and bournonite. Apatite is unaltered, and is always with a pseudomorph. SEM work revealed that most of the rock has been silicified.

A.2.8 UA44 – 349 metres

Sample UA44 – 349 is a moderately altered microporphyritic diorite. The grains are all anhedral and have an average size of 20μm in the groundmass and 0.75mm as phenocrysts. The mineralogy is dominated by albite, with some phenocrysts of potassium feldspar and relatively abundant hydrothermal biotite. Apatite is also present and is associated with biotite aswell as chlorite which is associated with the quartz/sulphide veins and biotite. Primary biotite pseudomorphous phenocrysts are completely sausseritized and are being overgrown by the hydrothermal biotite. Two veins sets are present in close to equal proportions. The earlier set introduced quartz, ore minerals and biotite. The later set, which cuts sulphides and does not contain biotite are filled with carbonate. Adjacent to some areas of the carbonate veins are albite porphyroblasts that have oriented themselves parallel with the carbonate vein suggesting that the albitization of the rocks coincides with later carbonate veining event (check against other sample that contains same texture). The ore minerals are dominantly chalcopyrite, with less pyrite and minor amounts of gold. Sericite alteration is moderate to strong in this sample.

A.2.9 UA50 – 245 metres

Sample UA50 – 245 is an intensely altered microporphryritic diorite. The groundmass is made of mostly of albite with some potassium feldspar that was determined by SEM. The phenocrysts are dominantly albite that are heavily sercitized. They also exhibit a zoned composition with sericite alteration being much more intense within the core and progressively less intense with each rim. This is a common feature of altered plagioclase that has a core with more a Ca-rich core that more easily alters to sericite. In addition to seritization, some grains have been partly altered to wollastonite. Large psuedomorphs of biotite have been completely sausseritized and are now being overgrown by hydrothermal biotite. Veins are not a prominent feature in this slide, and the ones that are clearly defined are filled with an unidentifiable dark, fine grain aggregate. However, growning around the veins is hydrothermal biotite. In addition, is areas where the vein contact is less defined secondary quartz and opaque minerals have precipitated. The chief ore mineral is chalcopyrite. Sericite alteration is strong in this sample.

A.2.10 UA52 – 383 metres

Sample UA52 – 383 is a microporphyritic monzodiorite. The subhedral phenocrysts reach up to 1.5mm in size and, with a few exceptions, are entirely albite. Groundmass grains have an average size of 50 μm. Albite dominates the groundmass, however SEM analysis showed that the ratio of potassium feldspar:albite is about 1:2 ratio. Minor amounts of quartz, hematite, and chlorite are also present in the groundmass. The sample is moderately fractured containing a network of veins which contain carbonate, specular hematite, chalcopyrite, bornite, epidote, quartz and chlorite. These minerals occur in very different proportions within each vein. To generalize, the veins are dominated by chalcopyrite, carbonate, or chlorite with all other minerals forming minor phases. Carbonate/chlorite psuedomorphs of biotite are present as phenocrysts commonly with bornite and chalcopyrite forming within the core of the grain. Chalcopyrite, bornite, and pyrite also form small blebs, 0.25mm on average, disseminated throughout the sample. Sericite alteration is moderate in this sample.

A.2.11 UA80 – 613 metres

Sample UA80 – 613 is a moderate to highly altered microporphyritic diorite. The groundmass is composed of albite, muscovite, and carbonate that is distributed pervasively throughout the slide. The average grain size of the groundmass is about 0.1mm. The phenocrysts are dominantly albite, some of which have been replaced by an aggregate of fine grained wollastonite. There is also quartz, apatite, and garnet porphyroblasts. In general the phenocrysts are around 0.5mm-1mm in size, except for the garnet porphyroblasts which have grown up to 1.5mm. All phases have an anhedral to subhedral shapes. Only one sample contains remnants garnet. The garnet is being replaced by chlorite, serpentine and carbonate. In addition to the replacement minerals, the garnets contain many inclusions of albite and apatite. Quartz fills out veins that also contain apatite, chlorite and the opaque minerals. Hydrothermal biotite, being replaced by chlorite, occurs close to these veins. Later stage carbonate veins cut the quartz veins showing an age relationship. The opaque mineral are mostly chalcopyrite with some associated bornite and minor amounts of gold. Sericite alteration is strong in this sample.

A.2.12 UA100 – 822 metres

Thin section UA100 – 822 is a microporphyritic diorite with a large vein cutting it. The average grain size of the groundmass is 50 μm. Phenocrysts reach over 1mm in size, but most are about 0.5mm and have a subhedral shape. The dominant mineral is plagioclase composing about 50% of the rock chiefly as phenocrysts. Based on SEM analysis of similar samples it is assumed that the plagioclase is all of the Na-end member variety Albite. The second most dominant phase is carbonate, which has developed pervasively in the groundmass in addition to filling minor vein structures, but only on one side of the apatite vein showing that the apatite vein came first. Along with the carbonate, the groundmass is composed of albite, chlorite and sericite. Pseudomorphs of biotite, also composed of fine grained chlorite, carbonate, and sericite, are present as phenocrysts and in the groundmass. These are considered to be a part of the groundmass in table 3.1. A single large vein, measuring 4.5mm wide contains principally apatite with potassium feldspar that tends to form at the edges and an aggregate of carbonate, chlorite, and serpentine filling in the space. Ore minerals contained within this vein are specular hematite and chalcopyrite. Throughout the rest of the sample chalcopyrite and pyrite form as blebs that are up to 2mm in size and specular hematite always forms with apatite. In one vein, chalcopyrite is associated with quartz. The larger plagioclase phenocrysts tend to be oriented with the long axis parallel to the apatite vein. Sericite alteration is poorly developed in this sample.

APPENDIX B - REPRESENTATIVE IMAGES

B.1 Representative thin section images
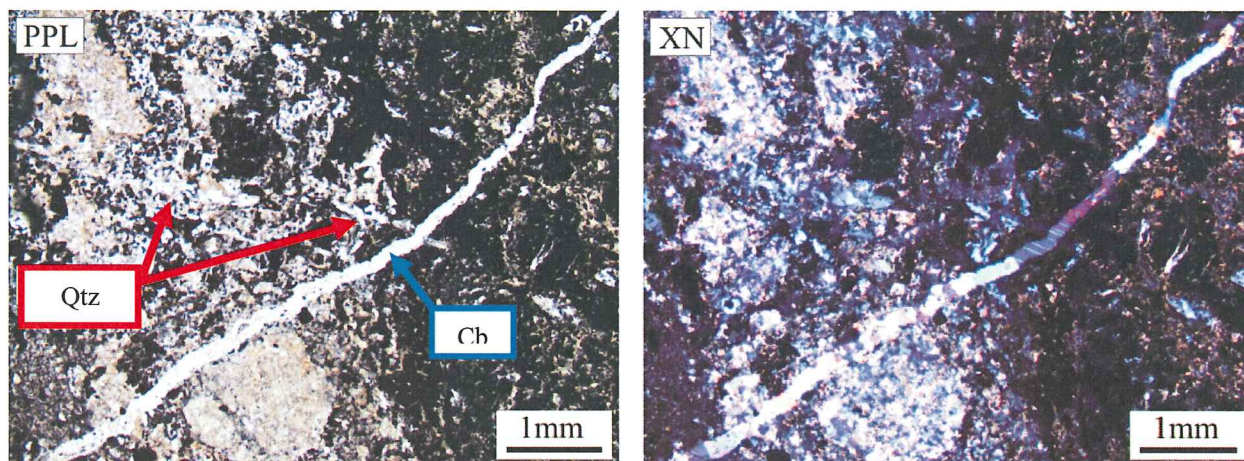
Figure B.1.1 Sample UA06 306. A late carbonate veins cutting a quartz vein and a breccia pipe containing carbonatized diorite clasts in a chlorite+carbonate matrix. The quartz veins also cuts the chlorite breccia, but the relationship is not as distinct.
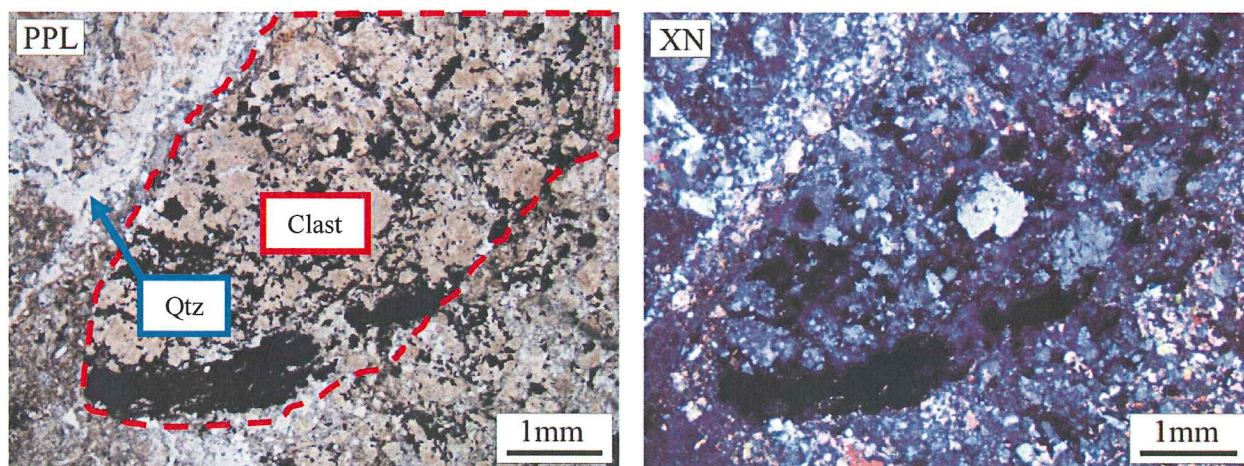
Figure B.1.2 Sample UA06 307. A large diorite clast in a chlorite+carbonate matrix. The lower edge of the clast is replaced by chalcopyrite. At the left of the image is a quartz vein that is redirected by the chlorite matrix.
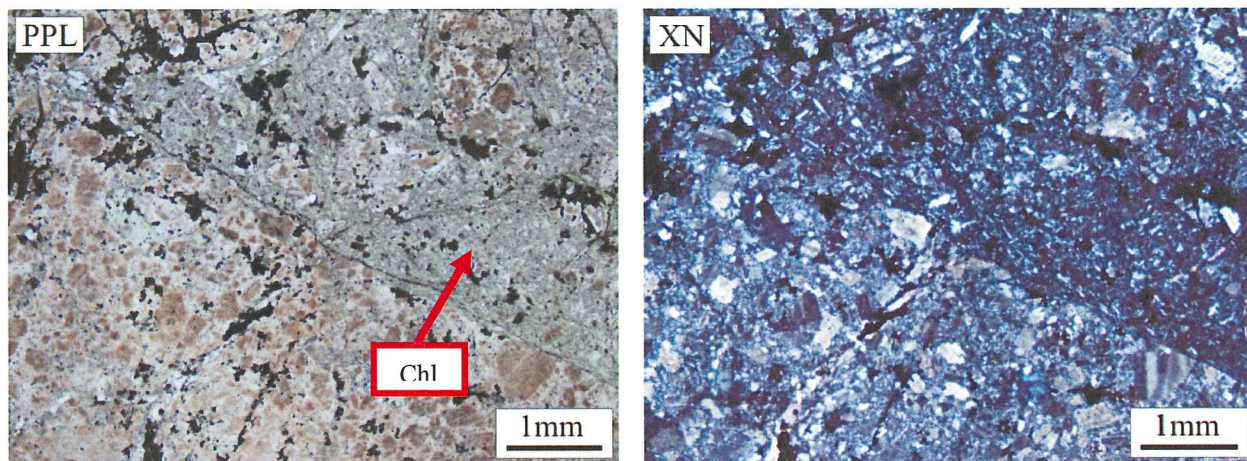
Figure B.1.3 Sample UA06 308. The edge of a breccia pipe containing diorite clasts in a chlorite matrix.
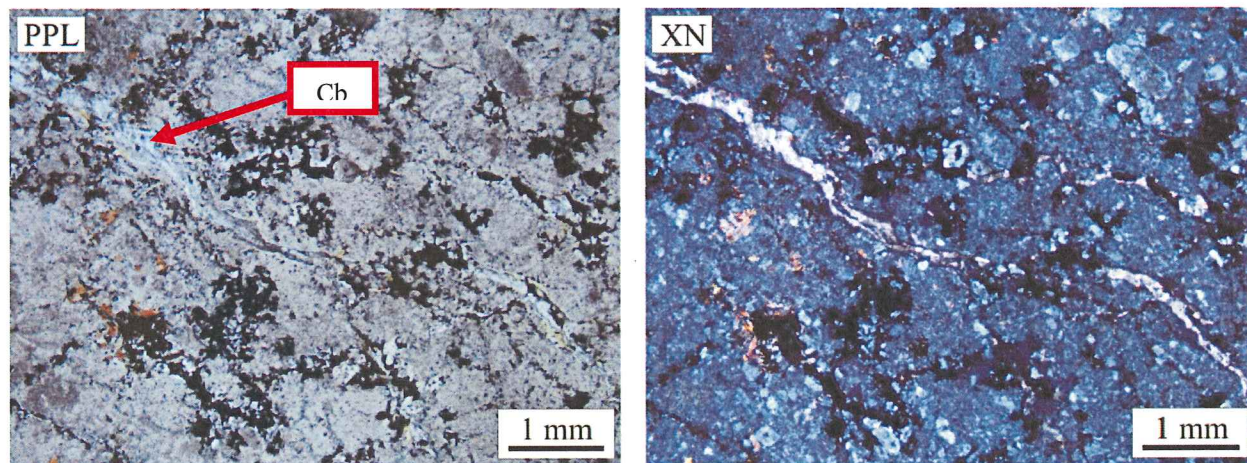
Figure B.1.4 Sample UA06 317. A carbonate veins cutting a diorite with large phenocrysts relative to other samples. Minor hydrothermal biotite is growing in the left side of image.
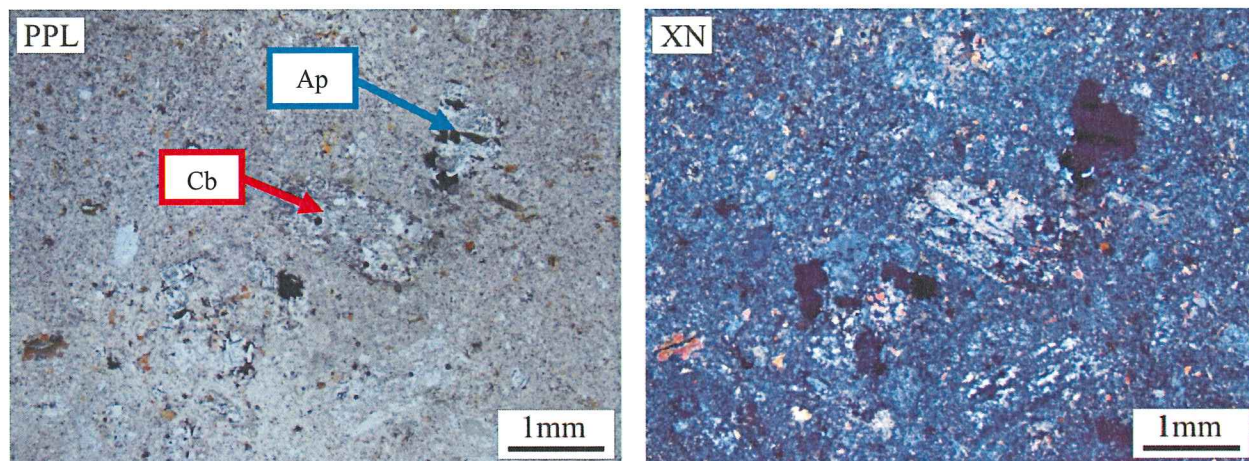
Figure B.1.5 Sample UA13 214. A diorite with a carbonate pseudomorph, a large apatite grain, and minor hydrothermal biotite.
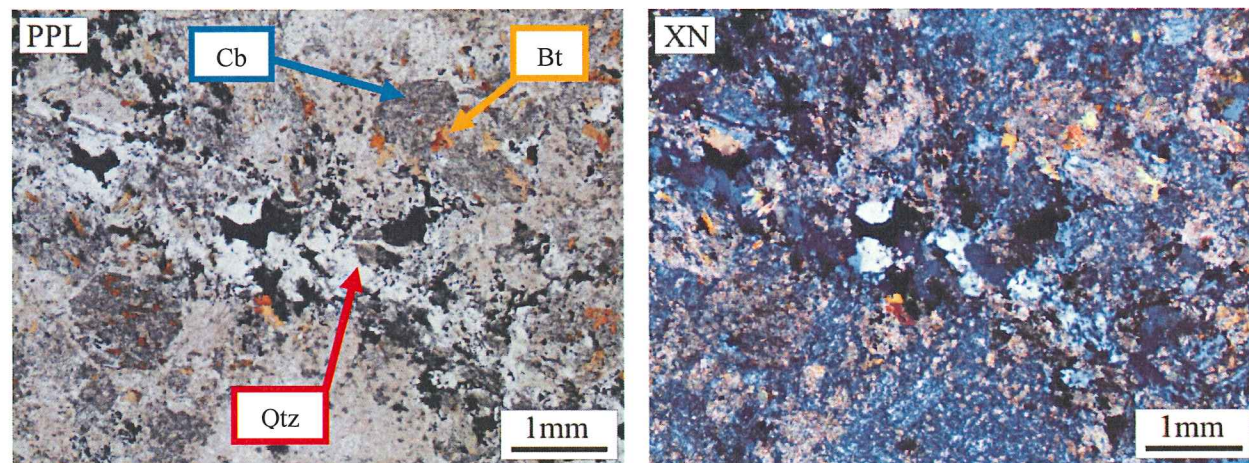
Figure B.1.6 Sample UA28 225. Diorite cut by a quartz vein. Abundant hydrothermal biotite is growing preferentially in contact with carbonate psuedomorphs.
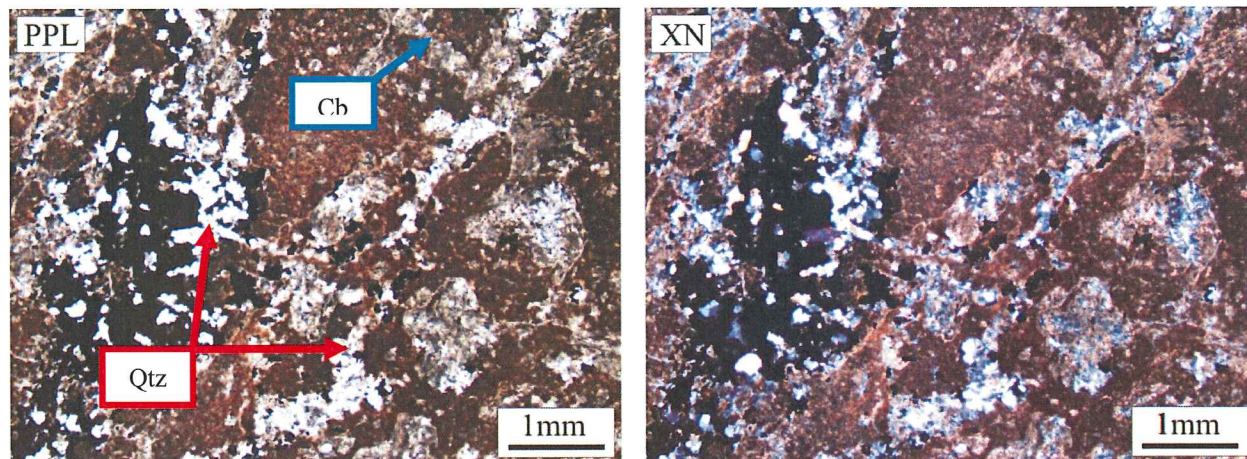
Figure B.1.7 Sample UA28 234. Intensly sericitized diorite cut by quartz veins containing abundant chalcopyrite. Early carbonate veins and carbonate psuedomorphs at right side of image.
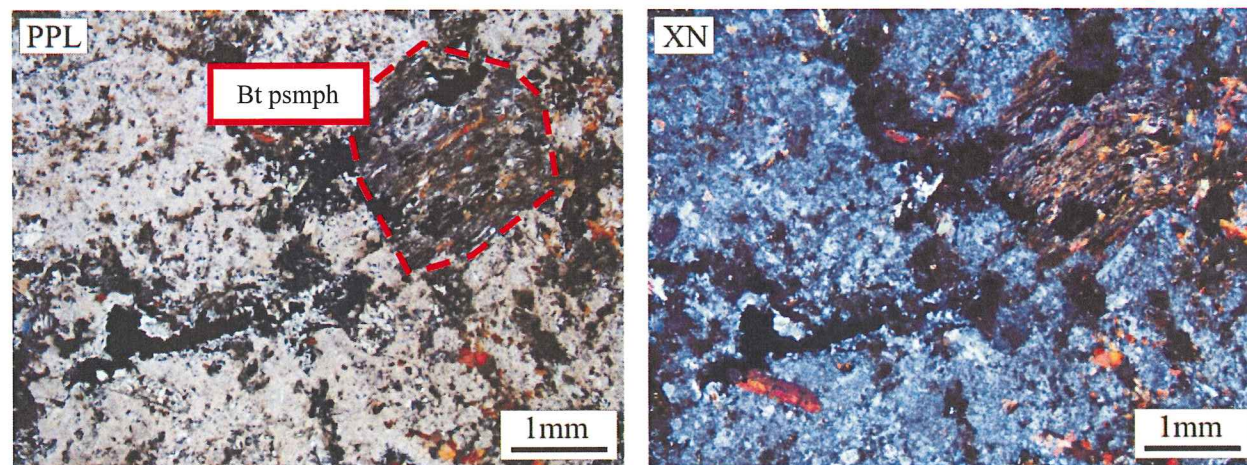
Figure B.1.8 Sample UA44 349. A large primary biotite that is being replaced by hydrothermal biotite in an intensely altered diorite.
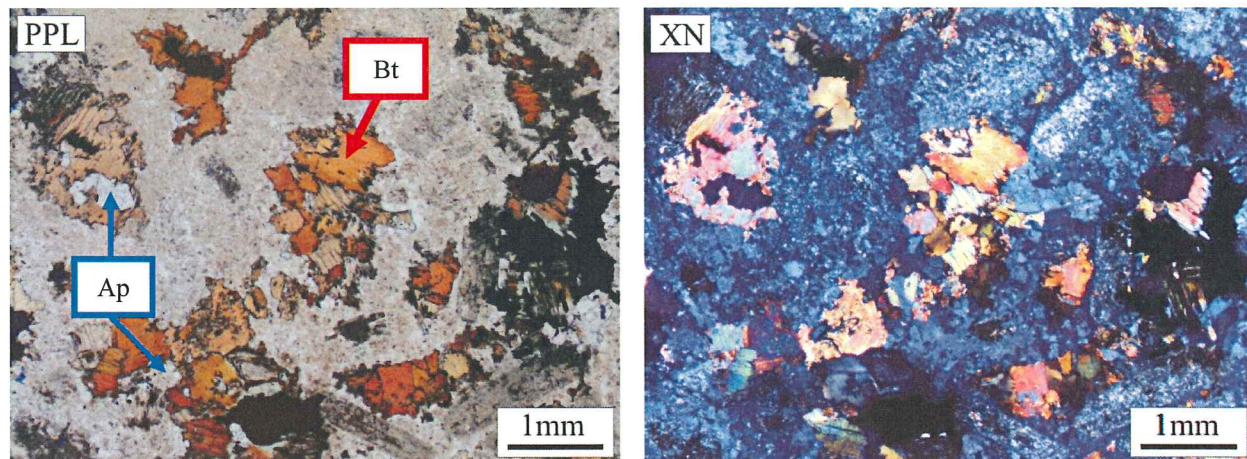
Figure B.1.9 Sample UA50 245. Large hydrothermal biotite that grow preferentially in contact with apatite in an intensely altered diorite.
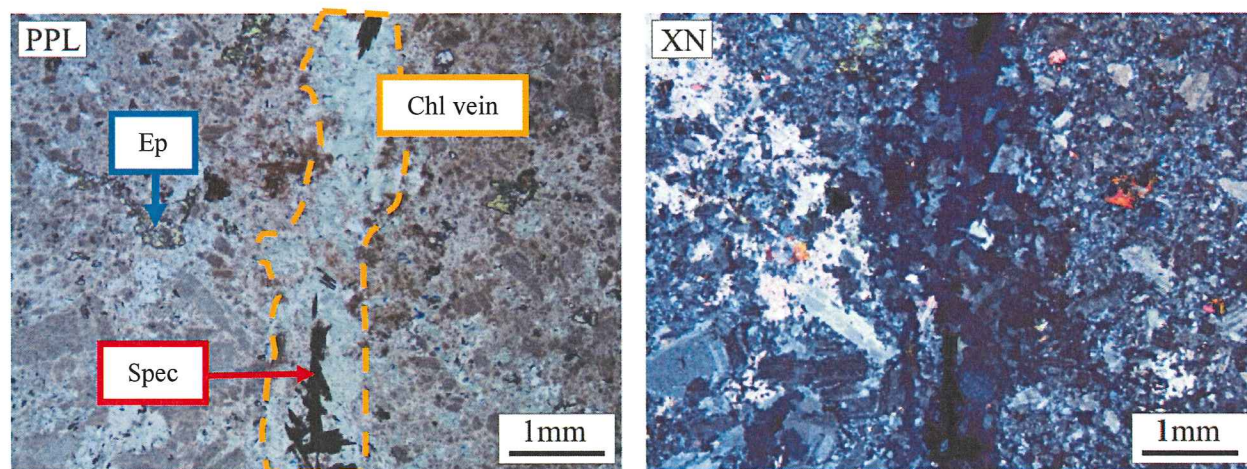
Figure B.1.10 Sample UA52 383. Diorite cut by a chlorite vein containing specularite. Growing in the wall rock, close to the vein, is epidote and to the left of the vein is apatite.
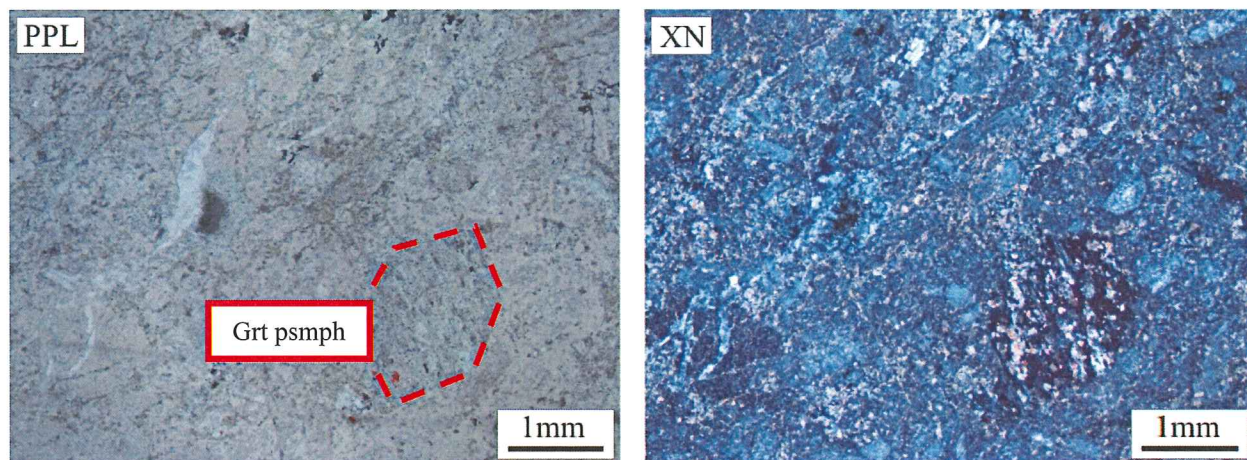
Figure B.1.11 Sample UA80 613. An intensely chloritized and carbonatized diorite. In the bottom right of the image is a chlorite psuedomorph of garnet(?).
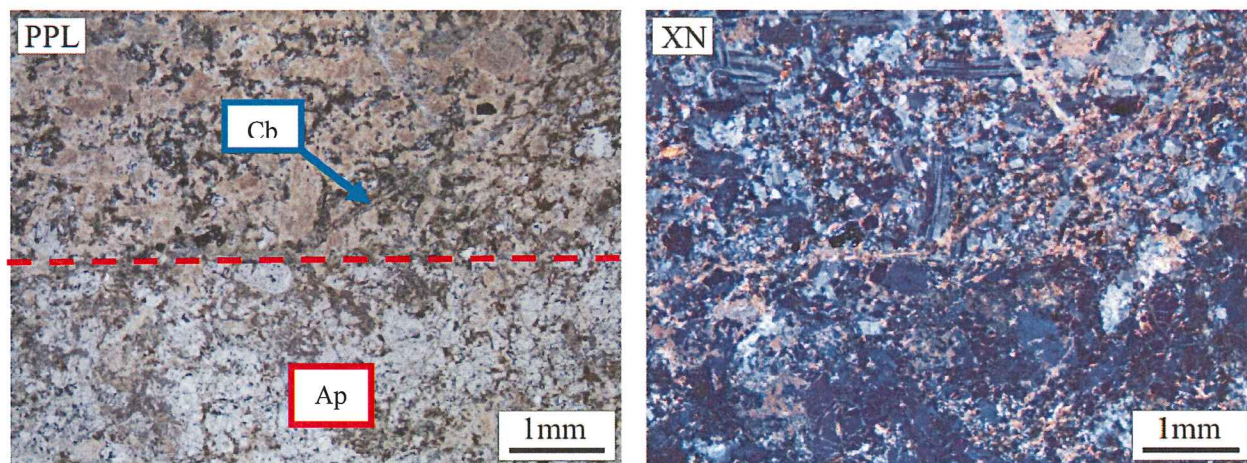
Figure B.1.12 Sample UA100 822. The bottom half of the image is occupied by a vein containing abundant apatite. The top half is wall rock that is cut by carbonate veins that were blocked by the apatite.

B.2 Representative backscatter electron images
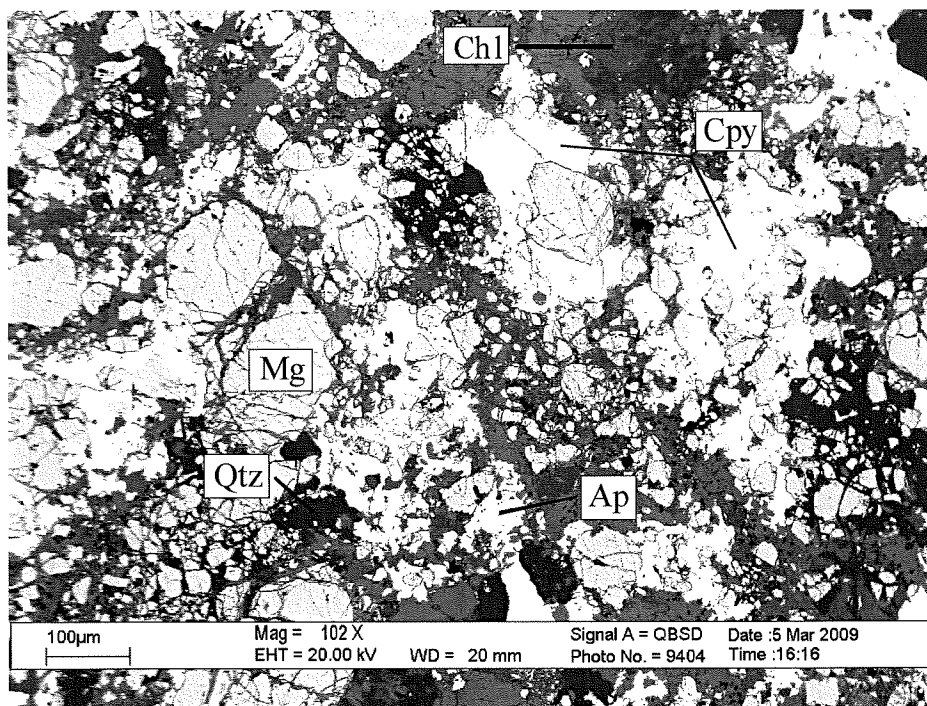
Figure B.2.1 Representative backscatter electron image of sample UA06 306. Abundant chalcopyrite and magnetite in a chlorite+carbonate±quartz matrix.
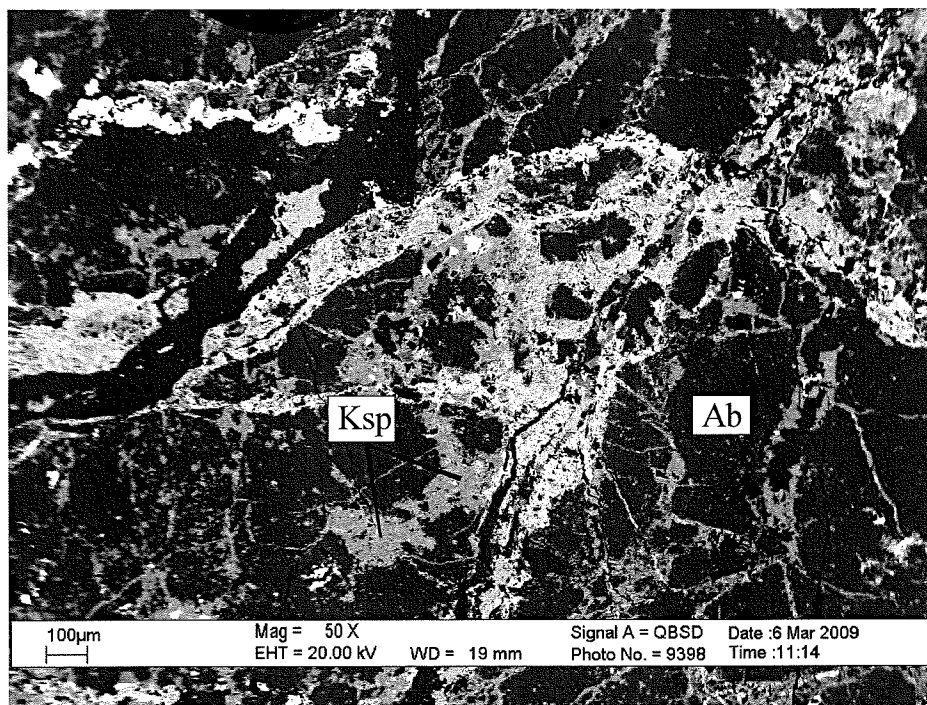
Figure B.2.2 Sample UA06 307. Veins containing K-feldspar, chlorite, and carbonate in an albite groundmass.
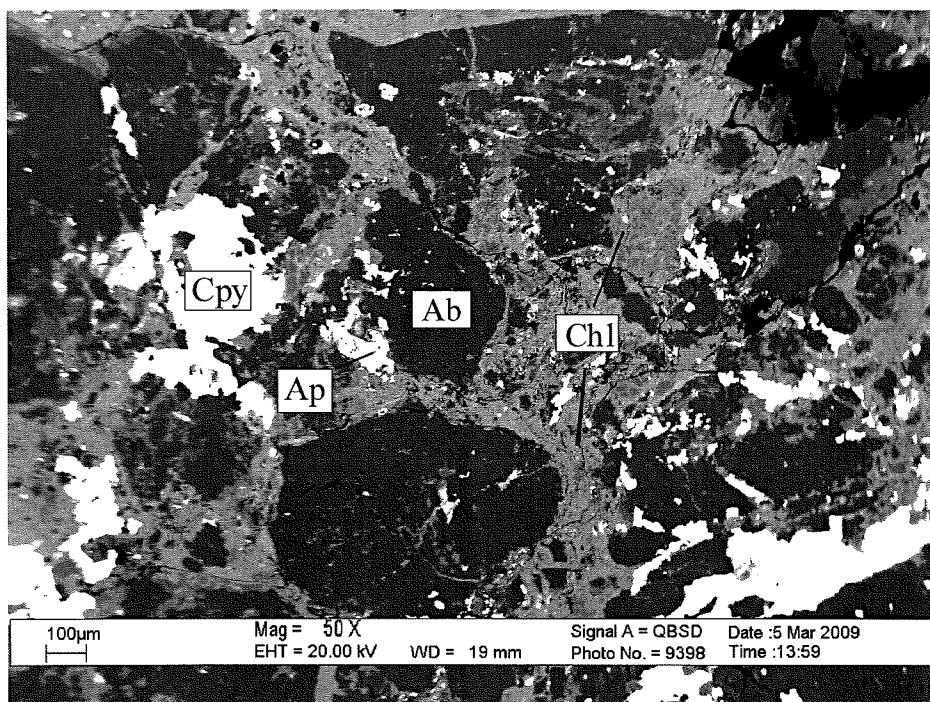
Figure B.2.3 Representative backscatter electron image of sample UA06 308. Albite clasts and chalcopyrite in a chlorite matrix
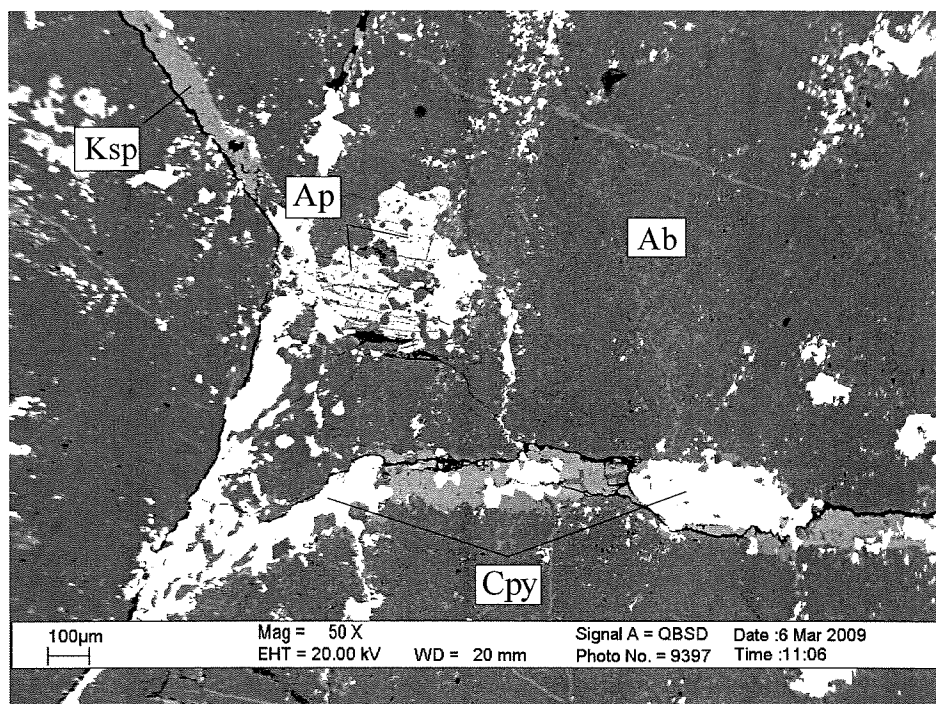
Figure B.2.4 Representative backscatter electron image of sample UA06 317. Hydrothermal apatite growing from K-feldspar veins that contain chalcopyrite. The groundmass consists of albite.
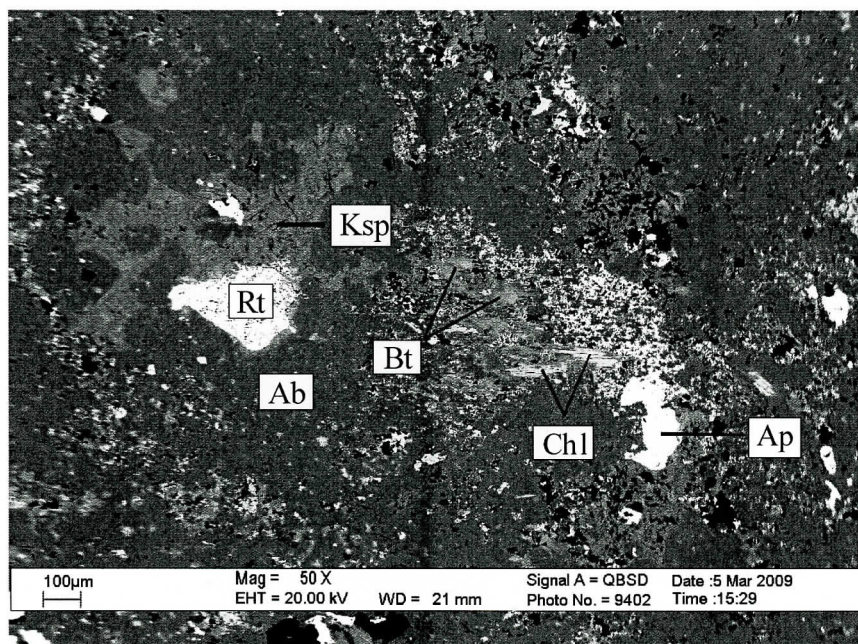
Figure B.2.5 Representative backscatter electron image of sample UA13 214. Mineralogy of the supergene zone. Chlorite is replacing primary biotite that is associated with apatite. Rutile is associated with K-feldspar.
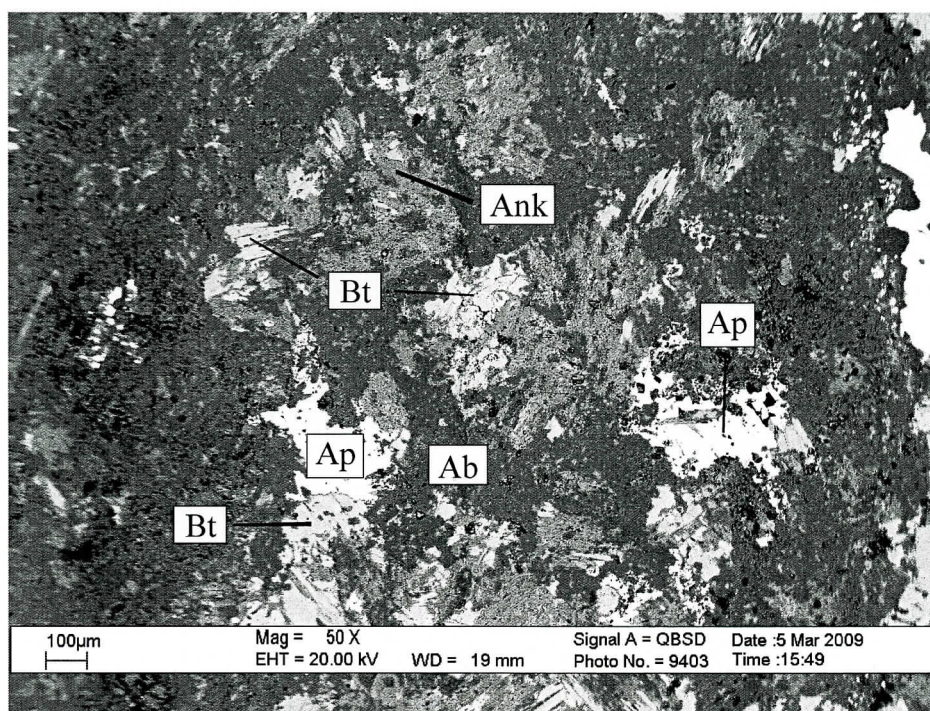
Figure B.2.6 Representative backscatter electron image of sample UA28 225. Hydrothermal apatite growing adjacent to biotite and moderate ankerite alteration in an albite groundmass.
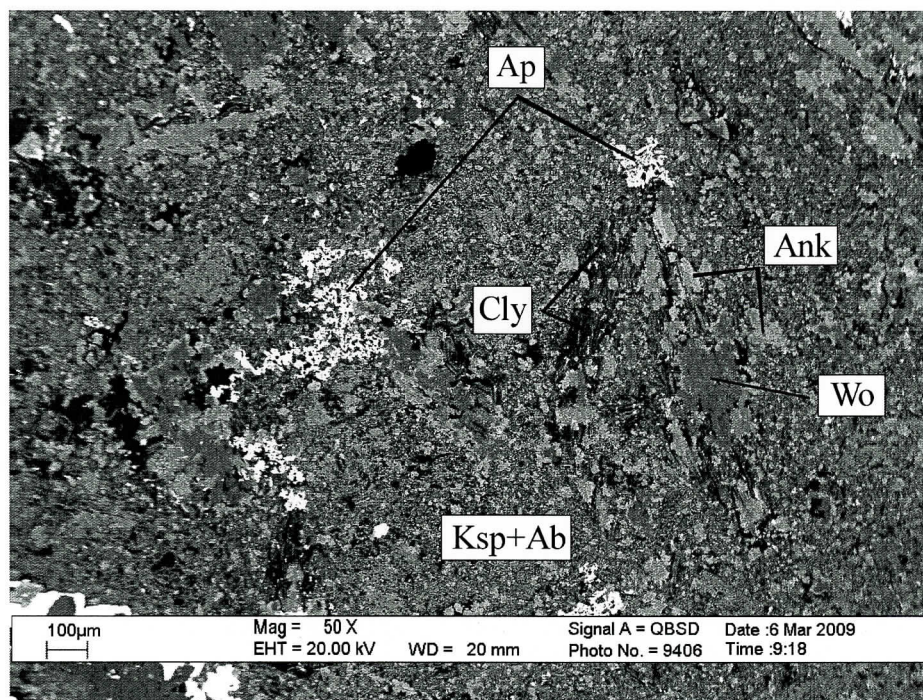
Figure B.2.7 Representative backscatter electron image of sample UA28 234. Bioite totally replaced by ankerite, wollastonite, and clay minerals. Hydrothermal apatite grow in association with the original. biotite grains. The groundmass has undergone intense potassic alteration.
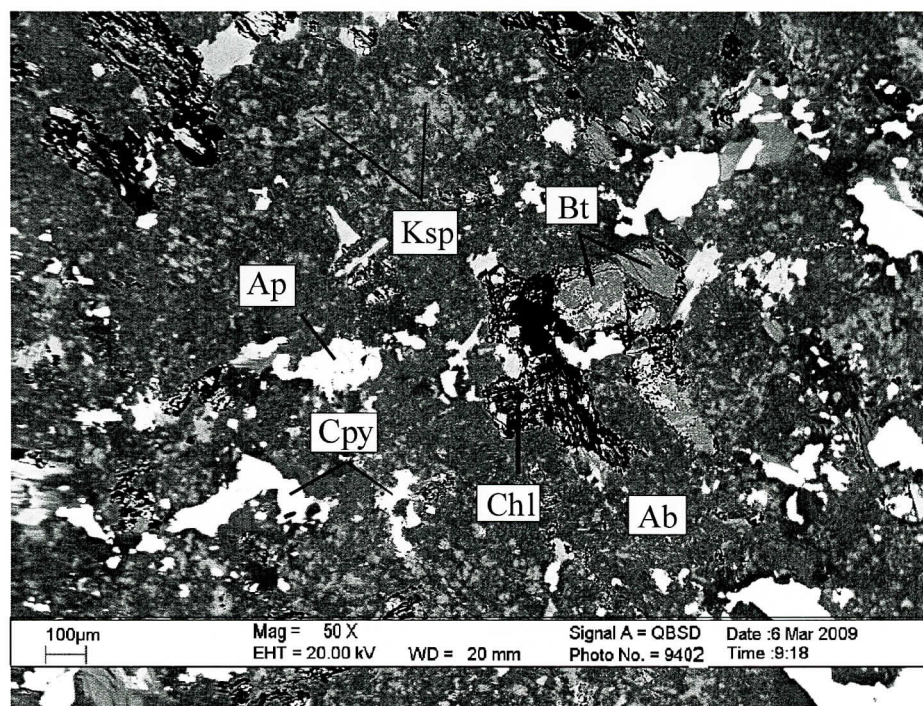
Figure B.2.8 Representative backscatter electron image of sample UA44 349. Chlorite replacing biotite. Apatite has a weak association with biotite. The groundmass consisting of albite has undergone moderate potassic alteration.
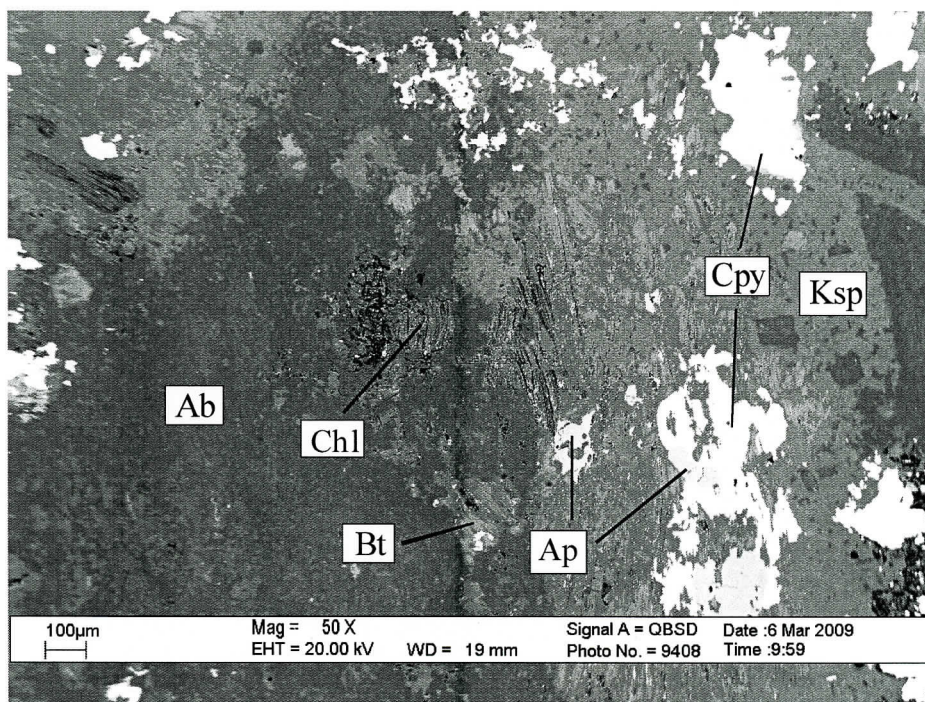
Figure B.2.9 Representative backscatter electron image of sample UA50 245. Chlorite replacing biotite. Apatite and chalcopyrite growing in K-feldspar vein. Albite groundmass that has undergone potassic alteration near vein.
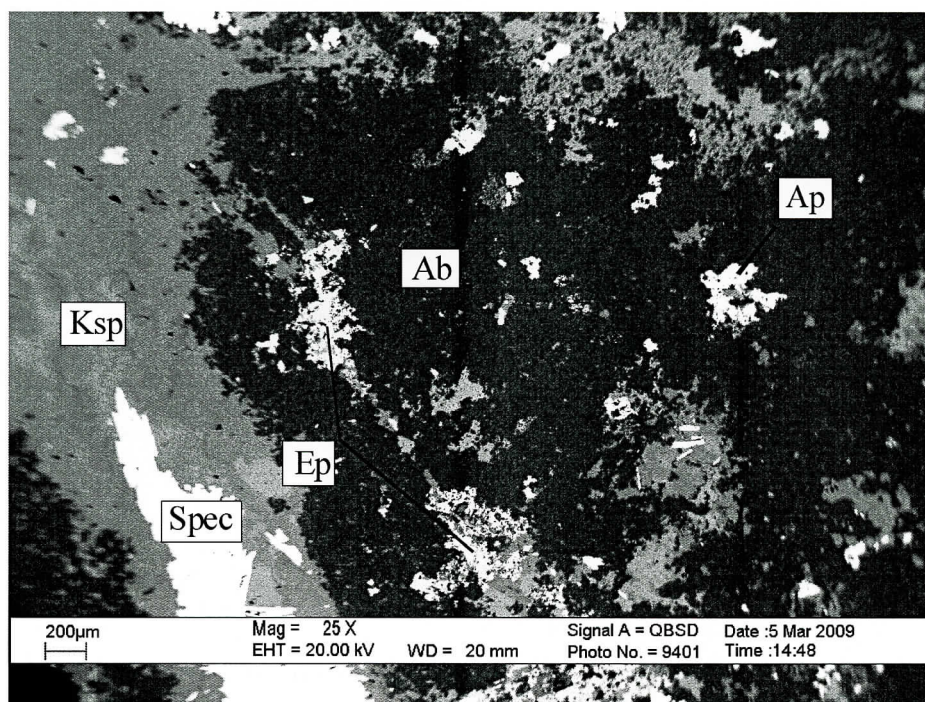
Figure B.2.10 Representative backscatter electron image of sample UA52 383. Epidote growing from a K-feldspar vein that contains specular hematite. Apatite growing in groundmass of albite.
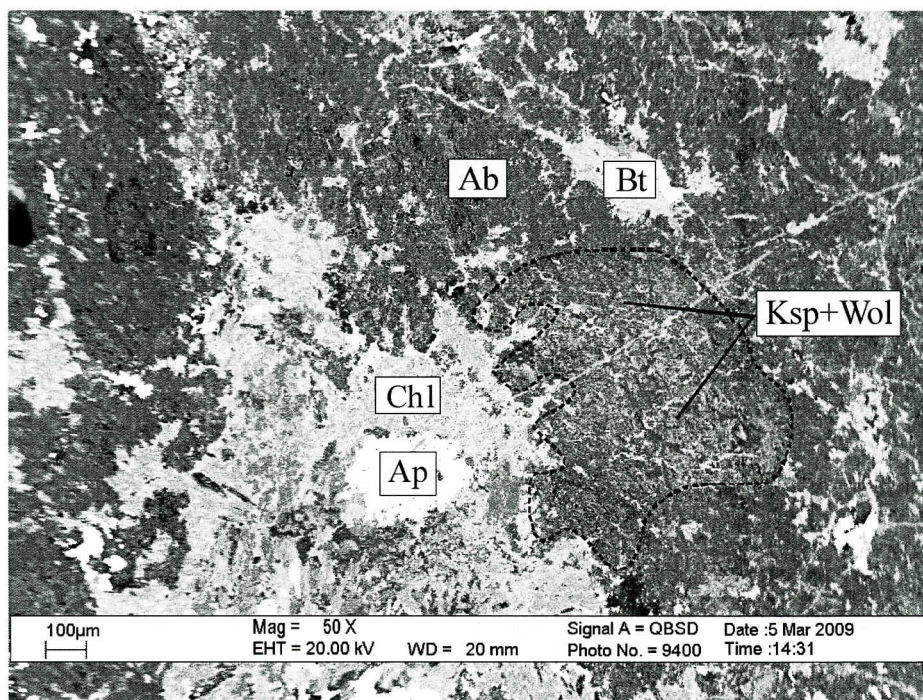
Figure B.2.11 Representative backscatter electron image of sample UA80 613. Apatite, and K-feldspar+wollastonite skarn alteration in association with chlorite.
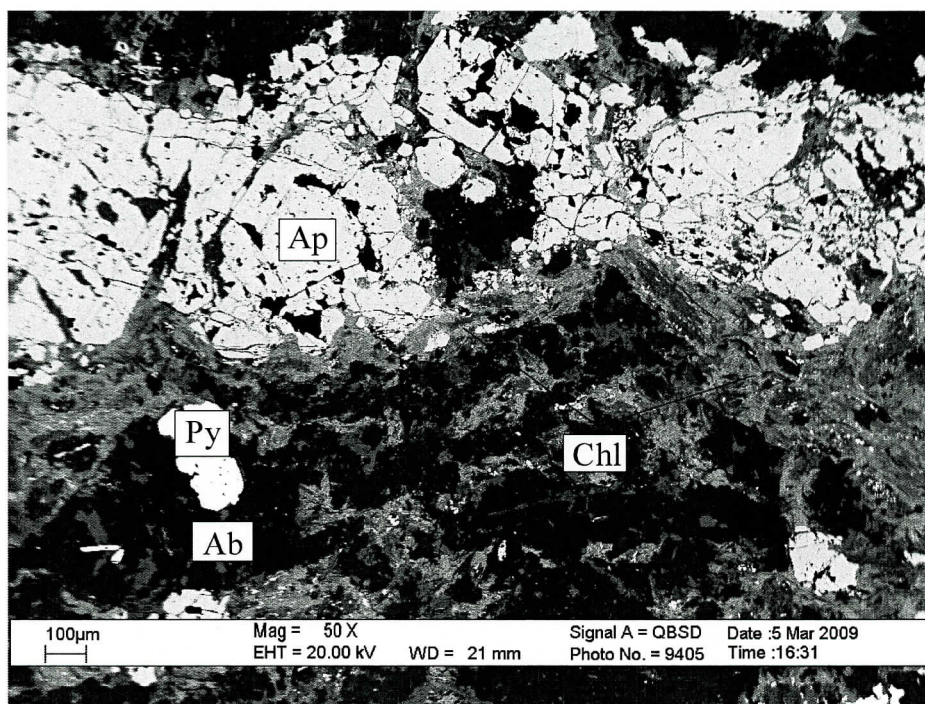
Figure B.2.12 Representative backscatter electron image of sample UA100 822. A large apatite vein with chlorite forming at the edge. The wall rock is albite.

APPENDIX C – EMP DATA

C.1 Sample calculations

C.1.4.1 Biotite-Apatite calculations

$X_{F(Ap)} = 0.75 \; mol$

$X_{OH(Ap)} = 0.25 \; mol$

$X_{F(Bt)} = 0.11 \; mol$

$X_{OH(Bt)} = 0.88 \; mol$

$X_{Fe(Bt)} = 0.65 \; mol$

$P = 8.6 \; Kbar \; (86000 \; Bar)$

$$lnK_D = ln \frac{\left(\frac{X_F}{X_{OH}}\right) Apatite}{\left(\frac{X_F}{X_{OH}}\right) Biotite} \qquad\qquad (Eq. \; 2.2)$$

$$lnK_D = ln \frac{\left(\frac{0.75}{0.25}\right)}{\left(\frac{0.111}{0.878}\right)} = 3.16$$

$$Tcalc \; (\square) = \frac{[(8852-(0.024*P)+(5000*X_{Fe})]}{[(1.987*\ln K_D)+3.3666]} - 273.1 \qquad\qquad (Eq. \; 2.3)$$

$$Tcalc \; (\square) = \frac{[(8852-(0.024*86000)+(5000*)]}{[(1.987*3.16))+3.3666} - 273.1 = 1098.4°C$$

C.1.4.1 Chlorite calculations

$Fe = 2.98 \; mol$

$Mg = 6.51 \; mol$

$Al^{IV} = 1.94 \; mol$

$$Al_C^{IV} = Al^{IV} + 0.1\left(\frac{Fe}{[Fe+Mg]}\right) \qquad\qquad (Eq. \; 2.6)$$

$$Al_C^{IV} = 1.94 + 0.1\left(\frac{2.99}{[2.99+6.51]}\right) = 2.16$$

$$T = 319 \; Al_C^{IV} - 69 \qquad\qquad (Eq. \; 2.7)$$

$$T = 319 * 2.16 - 69 = 620.4$$

C.2 Apatite microprobe data

Table C.2 Apatite microprobe analysis continued

Sample	UA13-214	UA13-214	UA13-214	UA13-214	UA13-214	UA13-214	UA13-214	UA44-349	UA44-349	UA44-349	UA44-349
Grain	A	B	B	C	C	D	D	A	B	B	C
No.	32.0	35.0	36.0	39.0	40.0	43.0	44.0	47.0	51.0	52.0	55.0
Wt %											
SiO_2	0.1	0.2	0.1	0.1	0.1	0.2	0.1	0.1	0.1	0.2	0.1
FeO	0.0	0.0	0.0	0.1	0.1	0.1	0.1	0.1	0.2	0.1	0.2
MnO	0.0	0.1	0.0	0.0	0.1	0.1	0.0	0.0	0.1	0.1	0.1
MgO	0.0	0.0	0.0	0.0	0.0	0.0	0.0	0.0	0.0	0.0	0.0
CaO	56.5	54.0	55.6	55.0	55.0	55.5	55.8	56.5	55.0	55.5	55.9
Na_2O	0.0	0.2	0.0	0.0	0.0	0.0	0.0	0.0	0.2	0.1	0.0
K_2O	0.0	0.0	0.0	0.0	0.0	0.0	0.0	0.0	0.0	0.0	0.0
P_2O_5	42.2	41.3	42.2	41.2	40.8	42.0	42.1	41.9	41.7	41.7	42.1
F	2.0	2.8	3.8	3.0	2.9	3.3	3.0	1.8	1.6	1.7	1.7
Cl	0.1	2.5	0.1	0.1	0.2	0.0	0.1	0.3	1.8	1.4	0.4
Total	101.0	101.1	101.8	99.8	99.1	101.3	101.2	100.7	100.8	100.8	100.6
O+F+Cl	0.9	1.7	1.6	1.3	1.3	1.4	1.3	0.8	1.1	1.1	0.8
C Total	100.2	99.3	100.2	98.5	97.9	99.9	99.9	99.9	99.7	99.7	99.8

Cations/anions (a.p.f.u calculated based on 10 cations)

Fe^{2+}	0.0	0.0	0.0	0.0	0.0	0.0	0.0	0.0	0.0	0.0	0.0
Mn	0.0	0.0	0.0	0.0	0.0	0.0	0.0	0.0	0.0	0.0	0.0
Mg	0.0	0.0	0.0	0.0	0.0	0.0	0.0	0.0	0.0	0.0	0.0
Sr	0.0	0.0	0.0	0.0	0.0	0.0	0.0	0.0	0.0	0.0	0.0
Ca	10.0	9.9	10.0	10.0	10.0	10.0	10.0	10.0	9.9	9.9	10.0
Na	0.0	0.1	0.0	0.0	0.0	0.0	0.0	0.0	0.1	0.1	0.0
K	0.0	0.0	0.0	0.0	0.0	0.0	0.0	0.0	0.0	0.0	0.0
Si	0.0	0.0	0.0	0.0	0.0	0.0	0.0	0.0	0.0	0.0	0.0
P	5.9	6.0	6.0	5.8	5.8	6.0	6.0	5.8	5.9	5.9	5.9
S	0.0	0.0	0.0	0.0	0.0	0.0	0.0	0.0	0.0	0.0	0.0
Cations	15.9	16.0	16.0	15.9	15.9	16.0	16.0	15.9	15.9	15.9	16.0
F	1.1	1.5	2.0	1.5	1.6	1.8	1.6	0.9	0.9	0.9	0.9
Cl	0.0	0.7	0.0	0.0	0.1	0.0	0.0	0.1	0.5	0.4	0.1

Table C.2 Apatite microprobe analysis continued

Sample	UA44-349	UA44-349	UA44-349	UA44-349	UA44-349	UA44-349	UA44-349	UA44-349	UA44-349	UA44-349	UA44-349
Grain	C	D	D	E	E	F	F	G	G	H	H
No.	56.0	59.0	60.0	63.0	64.0	67.0	68.0	71.0	72.0	75.0	76.0
Wt %											
SiO_2	0.1	0.1	0.1	0.1	0.1	0.1	0.1	0.1	0.1	0.2	0.1
FeO	0.0	0.0	0.1	0.0	0.0	0.1	0.1	0.2	0.2	0.1	0.2
MnO	0.0	0.0	0.0	0.1	0.0	0.0	0.0	0.1	0.0	0.0	0.1
MgO	0.0	0.0	0.0	0.0	0.0	0.0	0.0	0.0	0.0	0.0	0.0
CaO	56.5	56.1	55.7	56.1	56.7	56.3	56.0	54.5	55.3	55.7	56.1
Na_2O	0.0	0.0	0.0	0.0	0.0	0.0	0.0	0.1	0.0	0.0	0.0
K_2O	0.0	0.0	0.0	0.0	0.0	0.0	0.0	0.0	0.0	0.0	0.0
P_2O_5	42.1	42.0	41.7	42.2	41.9	42.1	42.1	41.7	41.9	41.7	42.0
F	1.8	1.9	1.9	1.8	1.8	1.9	1.7	2.7	2.8	2.2	2.6
Cl	0.2	0.4	0.4	0.3	0.4	0.3	0.6	1.7	0.5	0.2	0.3
Total	100.8	100.5	99.9	100.6	100.8	100.7	100.7	101.1	100.8	100.2	101.4
O+F+Cl	0.8	0.9	0.9	0.8	0.8	0.9	0.9	1.5	1.3	1.0	1.2
C Total	100.0	99.6	99.0	99.8	100.0	99.9	99.8	99.5	99.5	99.3	100.3

Cations/anions (a.p.f.u calculated based on 10 cations)

Fe^{2+}	0.0	0.0	0.0	0.0	0.0	0.0	0.0	0.0	0.0	0.0	0.0
Mn	0.0	0.0	0.0	0.0	0.0	0.0	0.0	0.0	0.0	0.0	0.0
Mg	0.0	0.0	0.0	0.0	0.0	0.0	0.0	0.0	0.0	0.0	0.0
Sr	0.0	0.0	0.0	0.0	0.0	0.0	0.0	0.0	0.0	0.0	0.0
Ca	10.0	10.0	10.0	10.0	10.0	10.0	10.0	9.9	10.0	10.0	10.0
Na	0.0	0.0	0.0	0.0	0.0	0.0	0.0	0.0	0.0	0.0	0.0
K	0.0	0.0	0.0	0.0	0.0	0.0	0.0	0.0	0.0	0.0	0.0
Si	0.0	0.0	0.0	0.0	0.0	0.0	0.0	0.0	0.0	0.0	0.0
P	5.9	5.9	5.9	5.9	5.8	5.9	5.9	6.0	6.0	5.9	5.9
S	0.0	0.0	0.0	0.0	0.0	0.0	0.0	0.0	0.0	0.0	0.0
Cations	15.9	15.9	15.9	15.9	15.9	15.9	15.9	16.0	16.0	15.9	15.9
F	0.9	1.0	1.0	1.0	0.9	1.0	0.9	1.5	1.5	1.1	1.3
Cl	0.1	0.1	0.1	0.1	0.1	0.1	0.2	0.5	0.1	0.1	0.1

Table C.2   Apatite microprobe analysis continued

Sample	UA06 - 317	UA28 - 225	UA28 - 225	UA28 - 225	UA28 - 225	UA28 - 225	UA28 - 225	UA28 - 225	UA28 - 225	UA28 - 225	UA28 - 225
Grain	A	A	B	B	C	C	D	D	E	E	F
No.	79.0	87.0	91.0	92.0	95.0	96.0	99.0	100.0	103.0	104.0	107.0
Wt %											
SiO_2	0.1	0.9	0.5	0.8	0.6	0.3	0.3	0.3	0.3	0.1	0.4
FeO	0.1	0.1	0.0	0.1	0.1	0.1	0.1	0.1	0.1	0.2	0.1
MnO	0.1	0.1	0.1	0.0	0.1	0.1	0.1	0.2	0.1	0.2	0.1
MgO	0.0	0.0	0.0	0.0	0.0	0.0	0.0	0.0	0.0	0.0	0.0
CaO	55.7	55.5	55.5	56.2	56.2	56.0	55.5	55.8	56.5	56.6	54.6
Na_2O	0.0	0.2	0.1	0.2	0.2	0.3	0.3	0.0	0.0	0.0	0.2
K_2O	0.0	0.0	0.0	0.0	0.0	0.0	0.0	0.0	0.0	0.0	0.0
P_2O_5	41.6	39.8	41.1	40.0	40.5	41.2	41.0	41.7	41.9	42.2	40.7
F	2.6	2.7	2.4	2.1	2.0	1.9	2.6	2.8	1.9	2.1	3.7
Cl	0.4	0.3	0.3	0.3	0.4	0.5	0.6	0.3	0.2	0.4	0.7
Total	100.6	99.4	100.1	99.8	100.1	100.3	100.6	101.2	101.1	101.7	100.6
O+F+Cl	1.2	1.2	1.1	1.0	0.9	0.9	1.3	1.2	0.9	1.0	1.7
C Total	99.4	98.3	99.0	98.8	99.2	99.4	99.3	99.9	100.2	100.8	98.8

Cations/anions (a.p.f.u calculated based on 10 cations)

Fe^{2+}	0.0	0.0	0.0	0.0	0.0	0.0	0.0	0.0	0.0	0.0	0.0
Mn	0.0	0.0	0.0	0.0	0.0	0.0	0.0	0.0	0.0	0.0	0.0
Mg	0.0	0.0	0.0	0.0	0.0	0.0	0.0	0.0	0.0	0.0	0.0
Sr	0.0	0.0	0.0	0.0	0.0	0.0	0.0	0.0	0.0	0.0	0.0
Ca	10.0	9.9	9.9	9.9	9.9	9.9	9.9	10.0	10.0	9.9	9.9
Na	0.0	0.1	0.0	0.1	0.1	0.1	0.1	0.0	0.0	0.0	0.1
K	0.0	0.0	0.0	0.0	0.0	0.0	0.0	0.0	0.0	0.0	0.0
Si	0.0	0.1	0.1	0.1	0.1	0.1	0.0	0.1	0.0	0.0	0.1
P	5.9	5.6	5.8	5.6	5.6	5.8	5.8	5.9	5.8	5.9	5.8
S	0.0	0.0	0.0	0.0	0.0	0.0	0.0	0.0	0.0	0.0	0.0
Cations	15.9	15.8	15.9	15.7	15.7	15.8	15.8	15.9	15.9	15.9	15.9
F	1.4	1.4	1.3	1.1	1.0	1.0	1.4	1.5	1.0	1.1	2.0
Cl	0.1	0.1	0.1	0.1	0.1	0.1	0.2	0.1	0.1	0.1	0.2

Table C.2   Apatite microprobe analysis continued

Sample	UA28 - 225	UA28 - 225	UA28 - 225	UA28 - 225	UA28 - 225
Grain	F	G	G	H	H
No.	108.0	111.0	112.0	115.0	116.0
Wt %					
SiO_2	0.3	0.1	0.0	0.4	0.3
FeO	0.1	0.0	0.2	0.1	0.1
MnO	0.1	0.1	0.1	0.0	0.2
MgO	0.0	0.0	0.0	0.0	0.0
CaO	55.9	56.5	56.8	56.0	55.9
Na_2O	0.4	0.1	0.0	0.4	0.5
K_2O	0.0	0.0	0.0	0.0	0.0
P_2O_5	40.6	42.0	42.4	40.5	40.3
F	1.9	2.1	2.2	1.9	2.1
Cl	0.5	0.2	0.2	0.4	0.5
Total	99.8	101.1	101.9	99.9	99.9
O+F+Cl	0.9	0.9	1.0	0.9	1.0
C Total	98.9	100.2	100.9	99.0	98.9

Cations/anions (a.p.f.u calculated based on 10 cations)

Fe^{2+}	0.0	0.0	0.0	0.0	0.0
Mn	0.0	0.0	0.0	0.0	0.0
Mg	0.0	0.0	0.0	0.0	0.0
Sr	0.0	0.0	0.0	0.0	0.0
Ca	9.9	10.0	10.0	9.8	9.8
Na	0.1	0.0	0.0	0.1	0.2
K	0.0	0.0	0.0	0.0	0.0
Si	0.1	0.0	0.0	0.1	0.1
P	5.6	5.9	5.9	5.6	5.6
S	0.0	0.0	0.0	0.0	0.0
Cations	15.7	15.9	15.9	15.7	15.6
F	1.0	1.1	1.1	1.0	1.1
Cl	0.1	0.1	0.1	0.1	0.1

C.3 Biotite microprobe anaylses

Table C.3 Biotite microprobe analysis

Sample	UA50 - 245	UA50 - 245	UA50 - 245	UA50 - 245	UA50 - 245	UA50 - 245	UA50 - 245	UA50 - 245	UA50 - 245	UA50 - 245
No.	9.0	10.0	13.0	14.0	17.0	18.0	21.0	22.0	25.0	26.0
Wt. %										
SiO_2	39.8	39.2	38.1	37.9	40.3	40.2	37.5	38.5	40.0	39.6
TiO_2	7.5	7.8	5.8	4.8	7.6	6.9	5.5	5.9	6.5	7.3
Al_2O_3	12.2	12.6	13.9	14.8	12.9	12.9	14.5	14.1	12.8	13.3
Cr_2O_3	0.0	0.0	0.0	0.0	0.0	0.0	0.0	0.0	0.0	0.0
FeO	9.1	9.4	10.6	12.5	8.8	9.3	11.7	10.9	11.3	10.3
MnO	0.1	0.1	0.2	0.2	0.1	0.1	0.2	0.1	0.2	0.1
MgO	18.2	17.8	17.9	18.4	19.0	19.0	18.0	17.9	17.8	17.9
CaO	0.0	0.0	0.0	0.1	0.0	0.0	0.2	0.1	0.0	0.1
Na_2O	0.2	0.2	0.2	0.1	0.2	0.1	0.2	0.2	0.1	0.2
K_2O	9.6	9.7	9.5	8.2	9.9	9.7	8.2	9.3	9.7	9.4
F	0.8	0.8	0.6	0.5	0.9	0.9	0.5	0.7	0.7	0.9
Cl	0.1	0.1	0.1	0.1	0.1	0.1	0.1	0.2	0.1	0.1
H_2O	1.6	1.6	1.6	1.7	1.6	1.6	1.7	1.6	1.6	1.6
Total	99.3	99.3	98.5	99.6	101.3	100.9	98.1	99.3	101.0	100.7
O+F+Cl	0.4	0.4	0.3	0.3	0.4	0.4	0.3	0.3	0.3	0.4
CTotal	99.0	98.9	98.2	99.3	100.9	100.5	97.9	99.0	100.7	100.3
Cations	(Calculated based on 14 cations)									
Si	5.9	5.8	5.6	5.5	5.8	5.8	5.5	5.7	5.8	5.8
Ti	0.8	0.9	0.6	0.5	0.8	0.7	0.6	0.6	0.7	0.8
Fe^{2+}	1.1	1.2	1.3	1.5	1.1	1.1	1.4	1.3	1.4	1.3
Mg	4.0	3.9	4.0	4.0	4.1	4.1	3.9	3.9	3.9	3.9
Ca	0.0	0.0	0.0	0.0	0.0	0.0	0.0	0.0	0.0	0.0
Na	0.0	0.0	0.0	0.0	0.0	0.0	0.0	0.0	0.0	0.1
K	1.8	1.8	1.8	1.5	1.8	1.8	1.5	1.7	1.8	1.7
Cations	15.9	15.9	15.8	15.6	15.9	15.8	15.6	15.8	15.8	15.8
F	0.4	0.4	0.3	0.2	0.4	0.4	0.2	0.3	0.3	0.4
Cl	0.0	0.0	0.0	0.0	0.0	0.0	0.0	0.0	0.0	0.0
OH	1.5	1.6	1.6	1.6	1.5	1.5	1.6	1.6	1.6	1.5

Table C.3   Biotite microprobe analysis continued

Sample No.	UA13-214 37.0	UA13-214 38.0	UA13-214 41.0	UA13-214 42.0	UA44-349 45.0	UA44-349 50.0	UA44-349 53.0	UA44-349 54.0	UA44-349 57.0	UA44-349 58.0
Wt. %										
SiO_2	37.8	37.7	37.9	37.0	39.5	39.5	38.9	38.7	38.4	38.0
TiO_2	6.6	7.0	6.1	8.3	5.2	4.1	6.4	6.6	6.3	6.4
Al_2O_3	13.8	13.7	14.0	13.6	13.0	13.6	13.9	13.5	13.7	13.9
Cr_2O_3	0.0	0.0	0.0	0.0	0.1	0.2	0.0	0.1	0.0	0.0
FeO	8.6	8.9	9.5	9.4	11.3	10.1	10.9	11.2	12.4	12.0
MnO	0.2	0.3	0.1	0.2	0.1	0.0	0.2	0.2	0.2	0.1
MgO	18.4	17.9	19.2	18.4	17.7	19.1	17.5	17.1	16.8	16.6
CaO	0.0	0.0	0.0	0.0	0.1	0.1	0.0	0.1	0.1	0.0
Na_2O	0.2	0.2	0.2	0.1	0.2	0.1	0.3	0.1	0.1	0.1
K_2O	9.7	9.8	9.2	9.0	9.4	9.9	9.7	9.8	9.8	10.0
F	1.3	1.2	1.2	1.3	0.4	0.7	0.4	0.3	0.2	0.2
Cl	0.2	0.2	0.1	0.1	0.2	0.2	0.2	0.2	0.2	0.2
H_2O	1.3	1.4	1.4	1.4	1.8	1.6	1.8	1.8	1.9	1.9
Total	97.9	98.3	99.0	99.0	99.0	99.3	100.2	99.6	100.0	99.5
O+F+Cl	0.6	0.6	0.5	0.6	0.2	0.3	0.2	0.2	0.1	0.1
CTotal	97.4	97.7	98.4	98.4	98.8	98.9	100.0	99.4	99.9	99.3
Cations	(Calculated based on 14 cations)									
Si	5.6	5.7	5.5	5.5	5.8	5.8	5.7	5.7	5.7	5.6
Ti	0.7	0.8	0.7	0.9	0.6	0.4	0.7	0.7	0.7	0.7
Fe^{2+}	1.1	1.1	1.2	1.2	1.4	1.2	1.3	1.4	1.5	1.5
Mg	4.1	4.0	4.2	4.1	3.9	4.2	3.8	3.8	3.7	3.7
Ca	0.0	0.0	0.0	0.0	0.0	0.0	0.0	0.0	0.0	0.0
Na	0.0	0.0	0.1	0.0	0.0	0.0	0.1	0.0	0.0	0.0
K	1.8	1.9	1.7	1.7	1.8	1.8	1.8	1.8	1.9	1.9
Cations	15.9	15.9	15.8	15.7	15.8	15.9	15.9	15.9	15.9	15.9
F	0.6	0.6	0.6	0.6	0.2	0.3	0.2	0.1	0.1	0.1
Cl	0.0	0.0	0.0	0.0	0.0	0.1	0.0	0.0	0.0	0.0
OH	1.3	1.4	1.3	1.3	1.7	1.6	1.7	1.8	1.8	1.8

Table C.3   Biotite microprobe analysis continued

Sample	UA44-349	UA44-349	UA44-349	UA44-349	UA44-349	UA44-349	UA44-349	UA06-317	UA28-225	UA28-225
No.	61.0	62.0	65.0	66.0	73.0	118.0	119.0	77.0	78.0	85.0
Wt. %										
SiO_2	39.4	38.5	38.3	38.3	36.8	39.9	38.3	39.3	39.3	39.6
TiO_2	5.8	5.1	6.6	6.1	6.6	4.1	6.6	6.3	5.0	6.7
Al_2O_3	12.8	14.3	13.8	13.5	13.9	12.9	13.9	13.2	13.7	12.8
Cr_2O_3	0.0	0.0	0.0	0.0	0.1	0.2	0.1	0.0	0.0	0.0
FeO	10.3	11.0	11.8	11.4	13.4	10.5	11.0	8.5	8.6	10.6
MnO	0.1	0.1	0.1	0.2	0.2	0.2	0.2	0.1	0.1	0.2
MgO	18.3	17.9	16.7	16.7	15.4	19.2	17.4	19.7	20.3	17.9
CaO	0.1	0.4	0.0	0.2	0.1	0.0	0.0	0.1	0.0	0.0
Na_2O	0.1	0.2	0.1	0.2	0.1	0.0	0.1	0.1	0.1	0.2
K_2O	9.6	9.6	9.7	9.7	9.4	10.0	10.1	9.9	9.9	9.9
F	0.4	0.3	0.3	0.3	0.2	0.5	0.2	1.0	1.2	0.7
Cl	0.2	0.2	0.2	0.2	0.2	0.2	0.2	0.1	0.2	0.2
H_2O	1.8	1.8	1.8	1.8	1.8	1.7	1.8	1.5	1.4	1.6
Total	98.8	99.3	99.6	98.6	98.1	99.3	99.9	99.9	99.8	100.4
O+F+Cl	0.2	0.2	0.2	0.2	0.1	0.3	0.1	0.5	0.6	0.3
CTotal	98.6	99.1	99.4	98.4	98.0	99.1	99.8	99.4	99.3	100.0
Cations	(Calculated based on 14 cations)									
Si	5.8	5.7	5.7	5.7	5.6	5.8	5.6	5.7	5.7	5.8
Ti	0.6	0.6	0.7	0.7	0.7	0.4	0.7	0.7	0.5	0.7
Fe^{2+}	1.3	1.4	1.5	1.4	1.7	1.3	1.4	1.0	1.0	1.3
Mg	4.0	3.9	3.7	3.7	3.5	4.2	3.8	4.3	4.4	3.9
Ca	0.0	0.1	0.0	0.0	0.0	0.0	0.0	0.0	0.0	0.0
Na	0.0	0.0	0.0	0.1	0.0	0.0	0.0	0.0	0.0	0.0
K	1.8	1.8	1.8	1.9	1.8	1.9	1.9	1.8	1.8	1.8
Cations	15.9	15.9	15.9	16.0	15.9	15.9	15.9	15.9	15.9	15.9
F	0.2	0.2	0.1	0.1	0.1	0.2	0.1	0.5	0.6	0.3
Cl	0.0	0.0	0.0	0.0	0.0	0.0	0.0	0.0	0.0	0.0
OH	1.7	1.8	1.8	1.8	1.8	1.6	1.8	1.5	1.4	1.6

Table C.3 Biotite microprobe analysis continued

Sample No.	UA28 - 225 86.0	UA28 - 225 90.0	UA28 - 225 93.0	UA28 - 225 94.0	UA28 - 225 97.0	UA28 - 225 98.0	UA28 - 225 101.0	UA28 - 225 102.0	UA28 - 225 105.0	UA28 - 225 106.0
Wt. %										
SiO_2	39.8	39.0	37.9	38.6	38.0	39.2	39.3	38.7	39.0	39.0
TiO_2	6.8	7.1	6.4	5.2	7.4	6.8	7.1	6.2	5.1	4.8
Al_2O_3	13.1	13.3	14.1	13.9	13.9	13.0	13.0	13.8	14.0	13.8
Cr_2O_3	0.0	0.0	0.0	0.0	0.0	0.0	0.0	0.0	0.0	0.0
FeO	10.3	10.2	11.7	10.8	11.0	10.8	11.3	11.3	10.3	10.1
MnO	0.2	0.1	0.2	0.1	0.1	0.1	0.2	0.1	0.1	0.1
MgO	18.3	17.4	16.9	18.1	16.9	17.6	16.7	17.2	18.8	19.0
CaO	0.0	0.0	0.0	0.0	0.1	0.0	0.1	0.1	0.0	0.0
Na_2O	0.1	0.2	0.2	0.1	0.2	0.1	0.2	0.3	0.1	0.1
K_2O	10.0	9.7	9.7	9.8	9.6	9.8	9.7	9.7	10.1	10.0
F	0.8	0.6	0.5	0.6	0.5	0.6	0.6	0.6	0.9	0.7
Cl	0.2	0.2	0.2	0.2	0.2	0.2	0.3	0.2	0.2	0.2
H_2O	1.6	1.7	1.7	1.6	1.7	1.6	1.6	1.6	1.6	1.6
Total	101.1	99.5	99.6	99.2	99.5	100.0	100.0	99.8	100.2	99.5
O+F+Cl	0.4	0.3	0.3	0.3	0.2	0.3	0.3	0.3	0.4	0.4
CTotal	100.7	99.2	99.3	98.9	99.3	99.6	99.7	99.5	99.8	99.2
Cations	(Calculated based on 14 cations)									
Si	5.8	5.8	5.6	5.7	5.6	5.8	5.8	5.7	5.7	5.7
Ti	0.7	0.8	0.7	0.6	0.8	0.8	0.8	0.7	0.6	0.5
Fe^{2+}	1.2	1.3	1.5	1.3	1.4	1.3	1.4	1.4	1.3	1.2
Mg	4.0	3.8	3.7	4.0	3.7	3.9	3.7	3.8	4.1	4.1
Ca	0.0	0.0	0.0	0.0	0.0	0.0	0.0	0.0	0.0	0.0
Na	0.0	0.1	0.0	0.0	0.1	0.0	0.1	0.1	0.0	0.0
K	1.9	1.8	1.8	1.8	1.8	1.8	1.8	1.8	1.9	1.9
Cations	15.9	15.9	15.9	15.9	15.9	15.9	15.9	15.9	15.9	15.9
F	0.4	0.3	0.2	0.3	0.2	0.3	0.3	0.3	0.4	0.3
Cl	0.0	0.0	0.0	0.0	0.0	0.1	0.1	0.1	0.0	0.0
OH	1.6	1.6	1.7	1.6	1.7	1.6	1.6	1.6	1.5	1.6

Table C.3 Biotite microprobe analysis continued

Sample No.	UA28 - 225 109.0	UA28 - 225 110.0	UA28 - 225 113.0	UA28 - 225 114.0	UA28 - 225 120.0
Wt. %					
SiO_2	38.9	39.2	39.0	38.1	39.4
TiO_2	7.0	6.9	7.1	7.6	6.9
Al_2O_3	13.0	13.1	12.5	13.7	13.4
Cr_2O_3	0.0	0.0	0.0	0.0	0.0
FeO	11.4	10.9	10.8	10.9	10.1
MnO	0.1	0.1	0.2	0.1	0.2
MgO	16.6	17.4	17.4	16.8	17.9
CaO	0.2	0.0	0.0	0.0	0.0
Na_2O	0.1	0.1	0.2	0.2	0.2
K_2O	9.5	9.8	9.9	9.9	9.5
F	0.5	0.6	0.7	0.6	0.7
Cl	0.2	0.2	0.3	0.2	0.2
H_2O	1.7	1.7	1.6	1.7	1.6
Total	99.4	100.1	99.7	99.8	100.0
O+F+Cl	0.3	0.3	0.3	0.3	0.3
CTotal	99.1	99.8	99.3	99.5	99.6
Cations	(Calculated based on 14 cations)				
Si	5.8	5.8	5.8	5.7	5.8
Ti	0.8	0.8	0.8	0.9	0.8
Fe^{2+}	1.4	1.3	1.3	1.4	1.2
Mg	3.7	3.8	3.9	3.7	3.9
Ca	0.0	0.0	0.0	0.0	0.0
Na	0.0	0.0	0.0	0.1	0.0
K	1.8	1.8	1.9	1.9	1.8
Cations	15.9	15.9	15.9	15.9	15.8
F	0.3	0.3	0.3	0.3	0.3
Cl	0.1	0.1	0.1	0.0	0.0
OH	1.7	1.6	1.6	1.6	1.6

C.4 Chlorite microprobe analyses

Table C.4   Chlorite microprobe analyses

No.	2.0	3.0	4.0	5.0	6.0	7.0	8.0	9.0	10.0
Sample	UA52 - 383	UA52 - 383	UA52 - 383	UA52 - 383	UA52 - 383	UA52 - 383	UA52 - 383	UA52 - 383	UA52 - 383
Wt. %									
FeO	17.5	17.0	17.2	16.3	17.3	18.6	16.8	17.3	17.5
Cr_2O_3	0.0	0.0	0.0	0.0	0.0	0.0	0.0	0.0	0.0
Na_2O	0.1	0.0	0.0	0.0	0.0	0.1	0.0	0.0	0.0
Al_2O_3	17.5	16.5	15.9	16.4	17.7	17.2	16.3	16.0	17.6
MnO	0.3	0.2	0.1	0.3	0.3	0.2	0.1	0.1	0.3
CaO	0.1	0.1	0.1	0.1	0.1	0.1	0.1	0.1	0.0
MgO	21.4	21.9	21.2	21.7	21.2	20.6	22.4	20.5	21.8
SiO_2	29.7	29.7	29.4	30.8	29.8	28.9	30.3	30.0	29.8
NiO	0.0	0.0	0.0	0.0	0.1	0.1	0.0	0.0	0.0
K_2O	0.0	0.0	0.0	0.0	0.0	0.0	0.0	0.1	0.0
TiO_2	0.0	0.0	0.0	0.0	0.0	0.0	0.0	0.0	0.0
Total	86.5	85.4	83.9	85.6	86.4	85.8	86.0	84.1	87.2

Cations (a.p.f.u calculated on the basis of 20 cations)

	2.0	3.0	4.0	5.0	6.0	7.0	8.0	9.0	10.0
Si	6.1	6.1	6.2	6.3	6.1	6.0	6.2	6.3	6.0
AlIV	1.9	1.9	1.8	1.7	1.9	2.0	1.8	1.7	2.0
AlVI	2.3	2.1	2.1	2.2	2.3	2.2	2.1	2.2	2.2
Ti	0.0	0.0	0.0	0.0	0.0	0.0	0.0	0.0	0.0
Fe^{3+}	0.0	0.0	0.0	0.0	0.0	0.0	0.0	0.0	0.0
Fe^{2+}	3.0	2.9	3.0	2.8	3.0	3.2	2.9	3.0	3.0
Mn	0.0	0.0	0.0	0.0	0.0	0.0	0.0	0.0	0.1
Mg	6.5	6.7	6.6	6.6	6.4	6.4	6.8	6.4	6.6
Ca	0.0	0.0	0.0	0.0	0.0	0.0	0.0	0.0	0.0
Na	0.0	0.0	0.0	0.0	0.0	0.0	0.0	0.0	0.0
K	0.0	0.0	0.0	0.0	0.0	0.0	0.0	0.0	0.0
Cations	19.9	19.9	19.8	19.7	19.8	19.9	19.9	19.7	19.9

Table C.4   Chlorite microprobe analyses

No.	11.0	12.0	13.0	14.0	15.0	16.0	17.0	18.0
Sample	UA52 - 383	UA80 - 613	UA80 - 613	UA80 - 613	UA80 - 613	UA80 - 613	UA80 - 613	UA80 - 613
Wt. %								
FeO	16.7	19.4	19.3	20.6	20.4	20.4	20.6	16.8
Cr_2O_3	0.0	0.0	0.0	0.0	0.0	0.0	0.0	0.0
Na_2O	0.0	0.1	0.0	0.0	0.0	0.0	0.1	0.1
Al_2O_3	16.8	16.9	17.2	15.4	19.2	19.2	16.7	15.6
MnO	0.2	0.3	0.2	0.2	0.4	0.4	0.4	0.2
CaO	0.1	0.1	0.1	0.1	0.0	0.0	0.1	0.1
MgO	22.2	18.6	20.3	16.2	17.0	17.0	18.6	22.5
SiO_2	30.4	29.7	29.1	30.6	27.5	27.5	29.9	30.6
NiO	0.0	0.1	0.1	0.1	0.1	0.1	0.1	0.2
K_2O	0.0	0.1	0.0	1.4	0.5	0.5	0.1	0.0
TiO_2	0.0	0.1	0.0	0.2	0.1	0.1	0.1	0.0
Total	86.4	85.3	86.4	84.9	85.2	85.2	86.8	86.0

Cations (a.p.f.u calculated on the basis of 20 cations)

	11.0	12.0	13.0	14.0	15.0	16.0	17.0	18.0
Si	6.2	6.2	6.0	6.5	5.8	5.8	6.2	6.3
AlIV	1.8	1.8	2.0	1.5	2.2	2.2	1.8	1.7
AlVI	2.2	2.4	2.2	2.4	2.6	2.6	2.3	2.0
Ti	0.0	0.0	0.0	0.0	0.0	0.0	0.0	0.0
Fe^{3+}	0.0	0.0	0.0	0.0	0.0	0.0	0.0	0.0
Fe^{2+}	2.8	3.4	3.3	3.7	3.6	3.6	3.6	2.9
Mn	0.0	0.0	0.0	0.0	0.1	0.1	0.1	0.0
Mg	6.7	5.8	6.3	5.2	5.4	5.4	5.7	6.9
Ca	0.0	0.0	0.0	0.0	0.0	0.0	0.0	0.0
Na	0.0	0.0	0.0	0.0	0.0	0.0	0.0	0.0
K	0.0	0.0	0.0	0.4	0.1	0.1	0.0	0.0
Cations	19.8	19.7	19.9	19.7	19.8	19.8	19.8	19.9

Table C.4	Chlorite microprobe analyses							
No.	19.0	20.0	21.0	22.0	23.0	24.0	25.0	26.0
Sample	UA80 - 613	UA06 - 307	UA06 - 307	UA06 - 307	UA06 - 307	UA06 - 307	UA06 - 307	UA06 - 308
Wt. %								
FeO	17.5	22.5	17.3	21.2	22.3	20.8	20.4	17.0
Cr_2O_3	0.0	0.0	0.0	0.0	0.1	0.0	0.0	0.0
Na_2O	0.0	0.0	0.0	0.0	0.0	0.0	0.0	0.0
Al_2O_3	16.7	18.7	19.8	19.3	19.9	19.4	20.6	18.8
MnO	0.2	0.5	0.3	0.5	0.5	0.4	0.1	0.4
CaO	0.1	0.1	0.1	0.1	0.1	0.1	0.1	0.1
MgO	19.8	16.3	19.7	17.0	17.2	17.1	16.6	20.7
SiO_2	28.4	27.6	27.3	27.6	28.2	27.6	27.7	29.4
NiO	0.1	0.1	0.1	0.0	0.1	0.0	0.1	0.0
K_2O	0.1	0.0	0.0	0.0	0.0	0.0	0.0	0.0
TiO_2	0.2	0.0	0.0	0.0	0.0	0.0	0.0	0.0
Total	83.1	85.8	84.8	85.7	88.4	85.6	85.7	86.6

Cations (a.p.f.u calculated on the basis of 20 cations)

Si	6.1	5.9	5.7	5.8	5.8	5.8	5.8	6.0
AlIV	1.9	2.1	2.3	2.2	2.2	2.2	2.2	2.0
AlVI	2.3	2.5	2.6	2.6	2.6	2.6	2.9	2.5
Ti	0.0	0.0	0.0	0.0	0.0	0.0	0.0	0.0
Fe^{3+}	0.0	0.0	0.0	0.0	0.0	0.0	0.0	0.0
Fe^{2+}	3.1	4.0	3.0	3.7	3.8	3.7	3.6	2.9
Mn	0.0	0.1	0.1	0.1	0.1	0.1	0.0	0.1
Mg	6.3	5.2	6.1	5.3	5.3	5.4	5.2	6.3
Ca	0.0	0.0	0.0	0.0	0.0	0.0	0.0	0.0
Na	0.0	0.0	0.0	0.0	0.0	0.0	0.0	0.0
K	0.0	0.0	0.0	0.0	0.0	0.0	0.0	0.0
Cations	19.8	19.8	19.9	19.8	19.8	19.8	19.7	19.8

Table C.4   Chlorite microprobe analyses

No.	27.0	28.0	29.0	30.0	31.0
Sample	UA06 - 308	UA06 - 308	UA06 - 308	UA06 - 308	UA06 - 308
Wt. %					
FeO	14.7	19.8	0.0	0.3	18.2
Cr_2O_3	0.0	0.0	0.0	0.0	0.0
Na_2O	0.0	0.0	0.0	0.0	0.0
Al_2O_3	19.1	18.4	0.0	2.6	18.3
MnO	0.3	1.0	0.6	1.1	0.7
CaO	0.1	0.1	66.5	56.8	0.1
MgO	22.0	17.8	0.0	0.2	18.2
SiO_2	29.4	27.9	0.0	5.3	28.1
NiO	0.0	0.0	0.0	0.0	0.1
K_2O	0.0	0.0	0.0	0.5	0.0
TiO_2	0.0	0.0	0.0	0.0	0.0
Total	85.6	85.1	67.1	66.8	83.8

Cations (a.p.f.u calculated on the basis of 20 cations)

	27.0	28.0			31.0
Si	6.0	5.9			6.0
AlIV	2.0	2.1			2.0
AlVI	2.5	2.5			2.6
Ti	0.0	0.0			0.0
Fe^{3+}	0.0	0.0			0.0
Fe^{2+}	2.5	3.5			3.2
Mn	0.0	0.2			0.1
Mg	6.7	5.6			5.8
Ca	0.0	0.0			0.0
Na	0.0	0.0			0.0
K	0.0	0.0			0.0
Cations	19.7	19.8			19.7

APPENDIX D – TRACE ELEMENT ANALYSES

Table D.1 Trace Element Analyses

Sample Rock Type	UA06 306.0 Bx	UA06 307.6 Bx	UA06 308.1 Bx	UA06 317.3 Di	UA28 225.7 Di	UA28 234.3 Ar	UA44 349.3 Di	UA50 245.5 Di	UA52 383.0 Di	UA80 613.5 Di
ppm										
Li	27.1	17.5	25.8	20.4	26.8	23.6	18.8	34.2	8.0	26.1
Rb	4.4	53.2	34.1	34.9	84.1	65.5	82.9	83.8	38.4	94.8
Cs	0.1	0.4	0.2	0.7	2.0	1.4	2.2	1.3	0.1	2.4
Tl	0.0	0.2	0.2	0.1	0.2	0.3	0.2	0.3	0.1	0.3
Pb	23.3	7.7	23.7	17.3	5.4	16.9	4.0	4.9	4.6	4.7
Ba	70.8	535.0	617.3	256.2	514.8	65.5	454.8	1334.1	211.9	1303.9
W	2.9	2.5	11.1	1.0	0.7	4.1	<0.5	0.6	1.3	0.8
Th	7.6	1.0	1.3	1.0	1.1	1.3	0.8	1.3	1.4	1.1
U	2.5	1.3	1.0	0.7	0.8	0.6	0.4	0.7	1.4	0.7
Ta	<0.2	<0.2	<0.2	<0.2	<0.2	0.2	<0.2	0.2	0.2	<0.2
Nb	1.7	1.8	1.9	2.0	2.2	1.8	1.7	3.2	2.7	2.3
La	73.4	6.0	6.5	5.4	4.5	6.0	4.0	5.2	9.9	4.4
Ce	137.5	12.2	14.4	10.9	13.2	13.3	8.5	12.5	22.0	8.9
Sr	116.0	176.0	87.0	345.0	323.0	132.0	502.0	729.0	363.0	254.0
Pr	15.8	1.6	1.9	1.4	2.3	2.0	1.2	1.9	3.2	1.2
Nd	66.3	7.3	8.8	6.4	12.7	10.8	6.4	9.8	14.9	5.6
Be	0.7	0.7	0.5	0.8	1.0	0.7	1.0	0.7	0.8	1.0
Zr	26.0	39.0	38.0	43.0	46.0	41.0	47.0	55.0	77.0	49.0
Hf	0.6	1.2	1.2	1.4	1.4	1.2	1.3	1.8	2.0	1.4
Sm	12.6	1.8	2.1	1.7	4.2	3.1	2.1	2.8	3.9	1.6
Eu	2.5	0.6	0.6	0.6	1.3	0.9	0.7	1.0	1.6	0.8
Gd	12.1	2.1	2.3	1.8	4.6	3.4	2.4	3.0	4.4	1.8
Tb	1.6	0.3	0.4	0.3	0.7	0.5	0.4	0.5	0.7	0.3
Ti	1592.0	2510.0	2654.0	2995.0	4385.0	2645.0	3188.0	4438.0	3141.0	3256.0
Dy	8.6	2.2	2.2	2.1	4.6	3.2	2.7	2.9	4.4	1.9
Y	52.8	13.4	13.6	13.3	24.9	18.5	16.1	17.0	26.2	12.1
Ho	1.7	0.5	0.5	0.5	1.0	0.6	0.6	0.6	0.9	0.4
Er	4.4	1.3	1.2	1.4	2.6	1.7	1.6	1.6	2.7	1.1
Tm	0.6	0.2	0.2	0.2	0.4	0.3	0.3	0.2	0.4	0.2
Yb	3.8	1.3	1.3	1.6	2.5	1.7	1.6	1.6	2.7	1.1
Lu	0.6	0.2	0.2	0.3	0.4	0.3	0.3	0.2	0.4	0.2
Sc	9.9	15.7	17.4	22.0	46.6	24.8	26.8	23.8	16.5	24.3
V	>600	220.0	307.0	277.0	321.0	197.0	300.0	217.0	152.0	274.0
Zn	56.0	33.0	49.0	43.0	67.0	159.0	49.0	76.0	29.0	47.0
Ni	160.0	63.0	71.0	64.0	153.0	100.0	237.0	120.0	56.0	306.0
Co	47.0	20.5	28.2	24.2	50.4	79.9	129.3	34.2	107.3	46.4
Cr	63.0	53.0	81.0	108.0	72.0	31.0	493.0	63.0	129.0	121.0
Ga	16.7	12.9	16.2	17.1	14.6	14.8	14.8	15.4	13.3	17.5